



Norwegian University of
Science and Technology

Patient Specific Finite Element Modelling of a Barlow Mitral Valve

Mechanical Engineering
Submission date: June 2019
Supervisor: Victorien Prot, KT

Norwegian University of Science and Technology
Department of Structural Engineering



MASTER THESIS 2019

SUBJECT AREA: Applied Mechanics (Biomechanics)	DATE: 03.06.19	NO. OF PAGES: 81
--	----------------	------------------

TITLE:

Patient Specific Finite Element Modelling of a Barlow Mitral Valve

BY:

Hans Martin Dahl Aguilera



SUMMARY:

The creation of accurate and reliable patient-specific finite element (FE) models of the mitral valve, is a fundamental step in order to improve and optimise patient-specific surgical repair and diagnosis. Furthermore, accurate finite element models of mitral valves may facilitate to an increased understanding of how the mitral valve functions, and how lesions develop.

In the present work, a patient-specific finite element model is created for a mitral valve diagnosed with Barlow disease. The FE geometry and boundary conditions are constructed from three-dimensional (3D) echocardiographic data, acquired from the studied patient. Moreover, the mitral valve leaflets and chordae tendineae are modelled using hyperelastic material models. The FE model of this Barlow mitral valve is created to investigate if a FE model can be used to predict the location of mitral regurgitation.

The global response of the mitral valve model is compared with echocardiographic measurements, and with the patient's lesions observed pre- and intraoperatively. The results showed regurgitation at both commissures, and the FE model aligned well with the echocardiographic measurements at peak systole. Compared with the patient's lesions, the FE model accurately predicted regurgitation in the posteromedial commissure. In the anterolateral region, however, the FE model predicted too severe regurgitation compared to the patient.

SUPERVISOR: Victorien Prot

CARRIED OUT AT: NTNU

Assignment

The mitral valve is a thin walled complex connective tissue structure located between the left atrium and left ventricle preventing the blood from flowing back into the atrium when the ventricle contracts. The mitral apparatus consists of two leaflets attached to the annulus, which is an ill-defined line between the left atrium and the left ventricle, and connected to a network of chordae tendinae further attached to the papillary muscles attached to the left ventricular wall. The normal function of the mitral valve depends on the coordinated actions of different anatomical parts: the left atrium, the mitral annulus, the mitral leaflets, the chordae tendinae, the papillary muscles and the left ventricle.

Barlow disease is a common cause of mitral regurgitation and leaflet prolapse. Barlow's disease is characterized by annular dilatation, leaflet prolapse, leaflet thickening due to excessive myxomatous tissue proliferation, chordal elongation and rupture. The goals of reconstructive surgery are to ensure normal leaflet motion and restoration of a sufficiently large surface of coaptation between the leaflets. This may be achieved by annuloplasty, neo-chordal replacement, leaflets resection and papillary muscle repositioning. Therefore, durable surgical mitral valve repair is a challenging task for surgeons.

The goal of this project is to develop a finite element model of a Barlow mitral valve before surgical treatment.

The project includes the following tasks:

- Literature review of Barlow disease with a focus on the mitral valve (anatomy, histology, material properties, surgical treatments)
- Development of a finite element model of a patient specific Barlow mitral valve with a focus on the chordae modelling and a parametric study of the leaflet material properties.

Research question:

- Is it possible to predict the location of mitral regurgitation?

Abstract

The creation of accurate and reliable patient-specific finite element (FE) models of the mitral valve, is a fundamental step in order to improve and optimise patient-specific surgical repair and diagnosis. Furthermore, accurate finite element models of mitral valves may facilitate to an increased understanding of how the mitral valve functions, and how lesions develop.

In the present work, a patient-specific finite element model is created for a mitral valve diagnosed with Barlow disease. The FE geometry and boundary conditions are constructed from three-dimensional (3D) echocardiographic data, acquired from the studied patient. Moreover, the mitral valve leaflets and chordae tendineae are modelled using hyperelastic material models. The FE model of this Barlow mitral valve is created to investigate if a FE model can be used to predict the location of mitral regurgitation.

The global response of the mitral valve model is compared with echocardiographic measurements, and with the patient's lesions observed pre- and intraoperatively. The results showed regurgitation at both commissures, and the FE model aligned well with the echocardiographic measurements at peak systole. Compared with the patient's lesions, the FE model accurately predicted regurgitation in the posteromedial commissure. In the anterolateral region, however, the FE model predicted too severe regurgitation compared to the patient.

Sammendrag

Utviklingen av nøyaktige og pålitelige pasientspesifikke elementmetodemodeller av mitralklaffen, er et fundamentalt skritt for å forbedre og optimalisere pasientspesifikk behandling og diagnostisering. Videre kan nøyaktige elementmetodemodeller, legge til rette for en økt forståelse av hvordan mitralklaffen fungerer, og hvordan lesjoner utvikles.

I denne oppgaven er det laget en pasientspesifikk elementmetodemodell, av en mitralklaff diagnostisert med Barlow sykdom. Elementmetodemodellens geometri er konstruert ved hjelp av tredimensjonal ekkokardiografisk data fra den studerte pasienten. Mitralklaff seilene og chordae tendineae er videre modellert med hyperelastiske material modeller. Grensebetingelsene som beskriver bevegelsesmønsteret til mitralklaffen er også pasientspesifikk, og er laget ved å følge annulus og papille-musklene gjennom systolen. Denne elementmetodemodellen er laget for å undersøke om en elementmetodemodell kan brukes til å estimere hvor en pasient med Barlow sykdom vil oppleve mitralklaffsvikt.

Den globale responsen til mitralklaffmodellen er sammenlignet med ekkokardiografiske målinger, samt pasientens observerte lesjoner før og under operasjon. Resultatene fra elementmetodemodellen viste lekkasje i begge commissurene, og modellen viste seg å passe godt til ekkokardiografiske målinger gjort ved maksimalt systolisk trykk. Sammenlignet med pasientens lesjoner, estimerte elementmetodemodellen lekkasje korrekt i den posteromediale commissuren. I den anterolaterale regionen estimerte elementmetodemodellen imidlertid en mer alvorlig lekkasje sammenlignet med det pasienten opplevde.

Preface

This master thesis is the final written work submitted as partial fulfillment of a Master of Science degree (M.Sc) in Mechanical Engineering at the Norwegian University of Science and Technology (NTNU). The thesis has been submitted to the Department of Structural Engineering, Faculty of Engineering Science, where the acquired specialization is Applied Mechanics. My supervisor has been Assoc. Prof. Victorien Prot at the Department of Structural Engineering.

The findings in this thesis has further been submitted and presented at the 10th National Conference on Computational Mechanics MekIT'19. The submitted paper can be found in appendix A.

Hans Martin Dahl Aguilera
June 3, 2019

Acknowledgements

I would first and foremost like to thank my supervisor, Assoc. Prof. Victorien Prot for all the invaluable help and guidance throughout the work with this thesis.

I would like to thank Stig Urheim M.D., Ph.D., for providing me with echocardiographic data of the studied patient, and answering questions related to the interpretation of echocardiographic data and Barlow disease in general.

I would also like to thank Kjell Saatvedt M.D., Ph.D., for allowing me to observe a surgery of a patient with mitral valve prolapse. This experience provided me with a greater understanding of the anatomical features and surgical procedures related to the mitral valve.

I would further like to thank my fellow student, Vetle Christensen Birkeland, for introducing me to and helping me with the usage of the CAD software Rhino.

Lastly, I would like to thank family and friends for the continuous support throughout this thesis.

Contents

List of Figures	xv
List of Tables	xvii
1 Introduction	1
2 Theory	3
2.1 The Heart	3
2.2 The Cardiac Cycle	4
2.3 Anatomy and Histology of the Mitral Valve	5
2.4 Barlow Disease	8
2.5 Surgical Repair Techniques	9
2.6 Patient	12
2.7 Continuum Mechanics	12
2.8 Constitutive Models	14
2.8.1 Holzapfel-Gasser-Ogden	14
2.8.2 May-Newman and Yin	14
2.8.3 Ogden Form	15
3 Modelling	16
3.1 Implementation of the Constitutive model	16
3.1.1 Mitral Valve Leaflets	16
3.1.2 Chordae Tendineae	19
3.2 The Mitral Valve Model	21
3.2.1 Mitral Valve Geometry	21
3.2.2 Chordae Modelling	24
3.2.3 Thickness Modelling	25
3.2.4 Contact Modelling	25
3.2.5 Boundary Conditions	25
3.2.6 Load History	26
3.2.7 Material Orientation	27
3.2.8 Element Types	28
4 Results	29
4.1 Measurements of FE Geometry	29
4.2 Global Response	31
4.3 Displacements	33

4.4	Comparison with Three-Dimensional Echocardiographic Data	34
4.5	Stresses	35
4.6	Thickness Study	36
4.7	Material Parameter Study	38
4.8	Mesh Study	40
4.9	Modified Annulus	41
5	Discussion	43
5.1	Global Response	43
5.2	Echocardiographic Modelling	44
5.3	Comparison with 3D Echocardiographic Data	44
5.4	Material Parameters	44
5.5	Boundary Conditions	45
5.6	Chordae Modelling	46
5.7	Material Orientation	46
5.8	Stresses	46
5.9	Mesh Study	47
5.10	Thickness Study	47
6	Concluding Remarks	48
6.1	Conclusion	48
6.2	Further Work	48
	Bibliography	50
	Appendices	56
A	Manuscript submitted for 10 th National Conference on Computa- tional Mechanics	57

List of Figures

2.1	Structure of the human heart	3
2.2	Electrical and mechanical representation of the cardiac cycle on the left heart. (Iaizzo, 2005)	4
2.3	Atrial view of the mitral valve (Carpentier et al., 2010)	6
2.4	Histological comparison of mitral valve leaflets (Hjortnaes et al., 2016)	9
2.5	Triangular vs Quadrangular resection technique (Carpentier et al., 2010)	11
3.1	Cauchy-stress vs stretch curves for the anterior leaflet. Fitted material model compared with experimental data on the anterior leaflet	18
3.2	Cauchy-stress vs stretch curves for the posterior leaflet. Fitted material model compared with experimental data on the posterior leaflet	19
3.3	Nominal stress vs nominal strain curves. Human and ovine chordae material parameters implemented in the Ogden material model.	20
3.4	Configuration of the mitral valve in the GUI related to echocardiographic data.	21
3.5	Explanation of the anatomical components on an echocardiographic image, end-diastolic configuration	22
3.6	Point cloud extracted from echocardiography	23
3.7	FE geometry created from echocardiographic data.	23
3.8	Geometry constructed from echocardiographic points at peak systole	24
3.9	Annular configurations during systole	26
3.10	Load amplitude curve in the cardiac cycle	26
3.11	Collagen fibre direction for both the anterior and posterior leaflet. (Einstein et al., 2005, Cochran et al., 1991)	27
3.12	Material orientation of the MV leaflets	28
4.1	Annular measurements and shape	30
4.2	Valve closure of finite element model from end-diastole to end-systole	31
4.3	Cut-view of prolapse at the posteromedial side of the P2 segment	32
4.4	Valve closure of finite element model from end-diastole to end-systole (Ovine chordae material parameters)	32
4.5	Norm of the displacement of point A and B	33
4.6	Comparison between finite element models and echocardiography	34
4.7	von Mises stress of the mitral valve leaflets (MPa)	35
4.8	Maximum principal stress on the mitral valve leaflets.	36
4.9	Stress along path for different leaflet thicknesses	37

4.10	Reduction in section thickness for different leaflet thicknesses of point A.	38
4.11	Displacement of point A obtained from analyses using stiffer and softer material parameters compared with material parameters from nonlinear data-fitting.	39
4.12	Different meshing techniques for the anterior leaflet	40
4.13	Magnitude plot of different meshing techniques	41
4.14	Closure of mitral valve after the annulus and papillary muscles are held constant	42

List of Tables

3.1	Material parameters proposed by May-Newman and Yin (1998) . . .	16
3.2	Material parameters obtained from nonlinear data-fitting of experimental data provided by May-Newman and Yin (1998)	18
3.3	Ogden model material parameters for modelling of chordae tendineae	20
4.1	Mitral valve measurements of the FE model, compared with measurements from literature both <i>in vitro</i> and from 3D echocardiography. (Kunzelman et al., 1994, Grewal et al., 2010, Chandra et al., 2011, Apor et al., 2016)	29
4.2	Mean stress along path and maximum $\Delta_{reduction}$ in section thickness for different leaflet thicknesses.	38

1

Introduction

The mitral valve is a complex structure that separates the left atrium from the left ventricle, ensuring one-way blood flow between the two heart chambers. This valvular structure consists of several components: the anterior and posterior leaflets, the annulus, chordae tendineae and the papillary muscles. The annulus is situated at the intersection between the left atrium and the left ventricle, and functions as an attachment ring for the two leaflets. Moreover, from the ventricular wall, the papillary muscles originate. From the papillary muscles, the chordae tendineae branches out and insert into the posterior and anterior leaflets. During the cardiac cycle, the components of the mitral valve work in concert in order to achieve proper closure at systole, enabling unidirectional blood flow.

The second most common valvular heart disease in European countries is mitral regurgitation (Iung et al., 2007). Mitral regurgitation is predominantly caused by degenerative diseases such as Fibroelastic Deficiency or Barlow disease (BD), where the latter is the topic of this thesis. BD affects the entire mitral valve apparatus, where a severely dilated annulus, excessive leaflet tissue, billowing or prolapse of the leaflets, myxomatous degeneration and chordae alterations are characteristic lesions. Another characteristic feature related to BD is that the annular saddle shape flattens, and overstretches at end systole (Apor et al., 2016). Furthermore, Barlow disease is mainly observed in patients younger than the age of 60 (Jouan et al., 2012). The work by Hjortnaes et al. (2016) studied the histological changes in the mitral valve due to Barlow disease. It was observed that the thickening of the mitral valve leaflets was caused by gathering of water absorbent proteins (proteoglycans) in the spongiosa layer, and intimal thickening of the fibrosa and atrialis.

Repairing a Barlow mitral valve is a complex procedure, and often the whole mitral apparatus must be assessed. Reconstructive surgery of the mitral valve may include annuloplasty, different sliding and resection techniques and artificial chordal insertions. Sophisticated imaging techniques have in recent years become available, leading to a greater understanding of the mitral valve dynamics. The motivation for this thesis is to develop a patient-specific finite element model of a Barlow mitral valve before surgical treatment. The development of such a model will hopefully enable us to predict the location of mitral regurgitation. Furthermore, with a realistic model it should be possible to perform surgical procedures *in silico*, optimising and creating a patient-specific repair procedure. To the author's knowledge, this is the first time a Barlow mitral valve has been studied using a finite element model.

This thesis is organised as follows. First theory related to the mitral valve, Barlow disease and surgical repair techniques is presented. Then the patient's pathology is described, followed by the continuum mechanical framework and material models

used. Thereafter, the modelling of the FE geometry and boundary conditions are described. Then, the results are presented and discussed. Finally, conclusions from the study and suggestions for further work are given.

2

Theory

2.1 The Heart

The heart is a muscular pump, pumping blood through the cardiovascular system transporting oxygen, nutrients, drugs, and water to the tissues. The heart is a four-chambered structure, consisting of the upper chambers (atria) left and right, and the lower chambers (ventricles) left and right (figure 2.1).

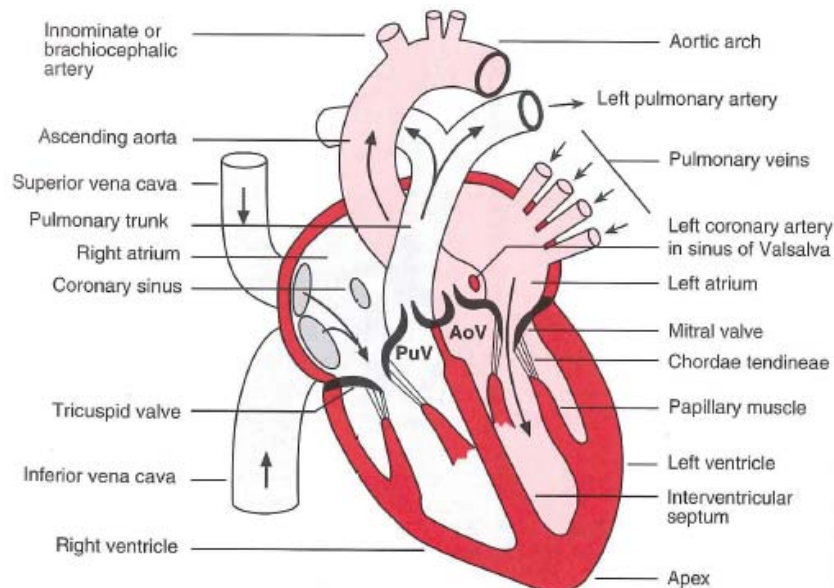


Figure 2.1: Structure of the human heart. Oxygenated blood (pink) and deoxygenated blood (grey). (Levick, 2010)

Oxygenated blood enters the left atrium and passes through the mitral valve into the left ventricle. From the left ventricle, blood is ejected through the aortic valve and into the aorta. From here, oxygenated blood supplies the tissues around the body with oxygen. As the tissues absorb some of the oxygen, the blood gets deoxygenated and returns into the right atrium from the superior and inferior vena cava. From the right atrium, deoxygenated blood passes through the tricuspid valve and into the right ventricle. As the pulmonary valve opens, blood is ejected from the right ventricle and into the pulmonary trunk, which guides the blood to the lungs. Completing the circuit, blood returns from the lungs, through the pulmonary veins and into the left atrium.

2.2 The Cardiac Cycle

The cardiac cycle consists of four distinct phases: ventricular filling, isovolumetric contraction, ejection, and isovolumetric relaxation, which are caused by atrial and ventricular contraction.

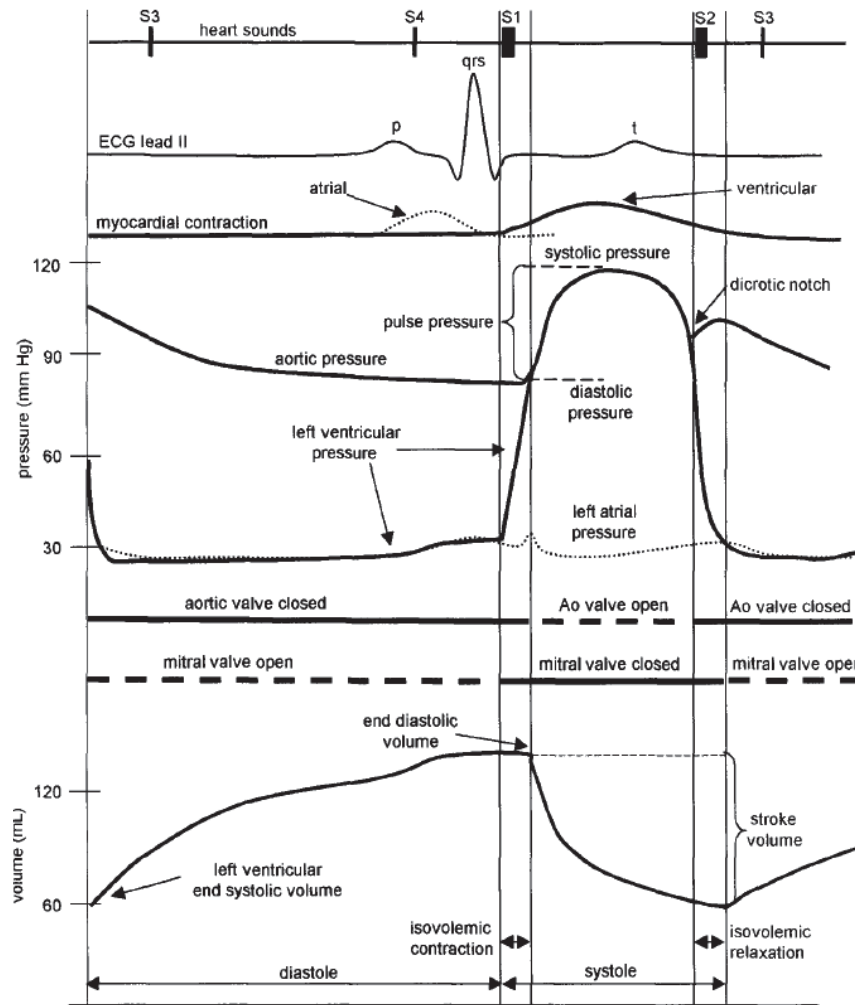


Figure 2.2: Electrical and Mechanical representation of the cardiac cycle on the left heart (Iaizzo, 2005).

In the left heart, the opening of the mitral valve characterises the beginning of diastole. The mitral valve opens when the atrial pressure exceeds the ventricular pressure, creating a pressure gradient between the two chambers. The created pressure gradient allows the blood to passively fill the left ventricle. At end diastole, as the passive filling slows down due to a diminishing pressure gradient, the left atrium contracts forcing extra blood into the left ventricle.

Left ventricular systole begins when the pressure in the left ventricle exceeds the pressure in the left atrium, leading the mitral valve to close, preventing outflow

of blood into the left atrium. After the mitral valve closes, the isovolumetric contraction phase begins, causing the ventricular pressure to further increase. As the ventricular pressure exceeds the aortic pressure, the aortic valve opens, and blood is ejected into the aorta. Lastly, at end systole the aortic valve closes when the aortic pressure exceeds the ventricular pressure (figure 2.2).

When studying echocardiographic data, the information from figure 2.2 is a valuable tool, especially the ECG curve and pressure curve. Comparing echocardiographic images with characteristic features such as the opening and closing of the aortic valve, enables the identification of anatomical features and configurations of interest. As the FE models boundary conditions are modelled from end-diastole to end-systole using echocardiography, it is essential to understand the dynamics of the heart at this time interval.

2.3 Anatomy and Histology of the Mitral Valve

In this section the anatomy and histology of the different constituents of the mitral valve is discussed

Annulus

The annulus is described as a non-planar saddle shaped fibrous structure, which functions as a junction zone between the left atrium, left ventricle, and the mitral leaflets. (Dal-Bianco and Levine, 2013). The annulus is divided into the anterior and posterior part of the annulus. The anterior part of the annulus is in fibrous connection with the right and left fibrous trigones and the aortic root (Ormiston et al., 1981). This fibrous connection makes the anterior part of the annulus less susceptible to dilation during the cardiac cycle (McCarthy et al., 2010). Moreover, the right and left fibrous trigones are located at the two lowest points of the saddle-shaped annular structure (Carpentier et al., 2010). The posterior part of the annulus is not entirely as connected to this fibrous region, making the posterior annulus more prone to dilation compared to the anterior part of the annulus (Van Mieghem et al., 2010)

A study performed by Kunzelman et al. (1994), showed that the total annular length increased by 20.9% for human mitral valves when subjected to pressures ranging from 0 to 120 mmHg. Furthermore, it was shown that the anterior annular length only increased 3.3%, while the posterior annular length increased by 31.1%. These findings substantiate the fact that the posterior annulus is more prone to dilation during the cardiac cycle.

Mitral Valve Leaflets

The mitral valve leaflets are divided into the anterior and posterior leaflet by the anterolateral and posteromedial commissures (figure 2.3). The mitral valve leaflets are analogous to a door in a door frame and open at the beginning of diastole. During diastole, the anterior leaflet divides the left ventricle into the outflow tract and the inflow chamber (Carpentier et al., 2010). In contrast, during systole, the leaflets

prevent blood from regurgitating back into the left atrium by coapting together. According to Ranganathan et al. (1970), the leaflets can be further subdivided into distinct zones. For both the anterior and posterior leaflet a clear and a rough zone is observed, while a basal zone is only to be found in the posterior leaflet. The clear zone is defined as the zone where chordal insertions are absent. Moreover, the rough zone is defined by chordal insertions at the ventricular surface, creating an irregular and uneven surface. Lastly, the basal zone is situated between the clear zone and annulus and is unique to the posterior leaflet as only here tertiary chords are inserted.

Carpentier et al. (1996) further divided the posterior leaflet into three different scallops: P1, P2, and P3, where the scallops are distinguished by indentations in the posterior leaflet (figure 2.3). The P1 scallop is situated next to the anterolateral commissure (AC), while the P3 scallop is located next to the posteromedial commissure (PC), leaving the P2 scallop between the two. The P2 scallop is further observed to be the largest of the three segments. In the study performed by Ranganathan et al. (1970), 46/50 hearts were found to have a tri-scalloped posterior leaflet. Quill et al. (2009) later confirmed that the majority of the posterior leaflets in their research also were tri-scalloped. Backing the common nomenclature presented by Carpentier.

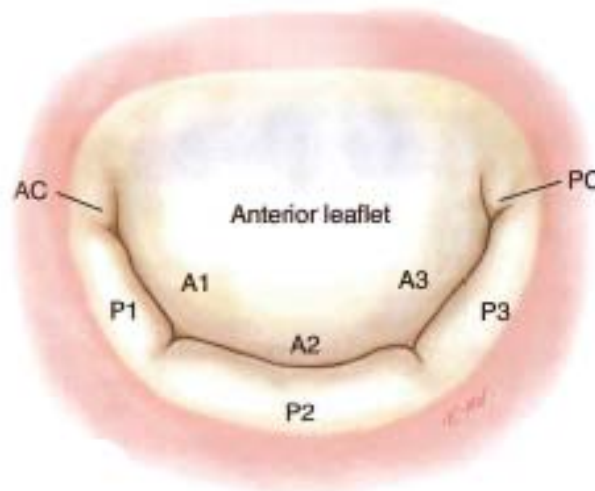


Figure 2.3: Atrial view of the mitral valve with leaflet segmentation. Anterolateral Commissure (AC), posteromedial Commissure (PC). Taken from (Carpentier et al., 2010)

The anterior leaflet has the shape of a bishop's mitre, and is by Carpentier et al. (1996) divided into three different segments: A1, A2, and A3. This segmentation of the anterior leaflet is done for descriptive purposes and is not distinguished by indentations as in the posterior leaflet.

The mitral valve leaflets are considered trilaminar structures and consists of the atrialis, spongiosa, and fibrosa. A thin ventricular layer termed the ventricularis is in some papers, also mentioned as a layer (Gross and Kugel, 1931, Fornes et al.,

1999, Prot and Skallerud, 2017). However, in other papers, the mitral valve leaflets are referred to as a trilaminar structure, where the fibrosa and ventricularis are considered as one layer (Dal-Bianco and Levine, 2013, Hjortnaes et al., 2016). The atrialis is the atrium facing layer and consists of aligned elastin and collagen fibres. The spongiosa is situated below the atrialis, and consist mainly of water absorbent proteins (glycosaminoglycans). Also, small traces of randomly oriented elastin and collagen can be found in the spongiosa. Lastly, the fibrosa layer is composed of a dense, highly aligned layer of collagen. (Roberts et al., 2016, Zhang et al., 2016, Dal-Bianco and Levine, 2013)

Chordae Tendineae

The chordae tendineae are fibrous chords that originate either from the papillary muscles tips or from the posterior part of the ventricular wall (Lam et al., 1970). In the work done by Kunzelman et al. (1994), it was observed that for each chordae tendineae originating from the papillary muscle, the chordae branches out in a fan-like manner and inserts into the mitral valve leaflets in approximately five different insertion points.

There have been several suggestions to the categorisation of chordae, where the leaflet insertion point has been the most common classifier. Primary (marginal) chordae inserts into the free edge of the mitral valve leaflets. Secondary (rough zone) chordae insert into the leaflets rough zone. Tertiary chordae insert into the basal zone of the posterior leaflet and originates from the posterior part of the ventricular wall or the papillary muscles (Muresian, 2009, Ho, 2002, Lam et al., 1970). However, tertiary chordae is not observed in all mitral valves. In the study performed by Lam et al. (1970), only 31 out of 50 were found to have these tertiary chords.

The primary chords main function is to prevent leaflet prolapse and is essential for coaptation. Secondary chordae supports leaflet and ventricular geometry. Furthermore, secondary chordae is observed to be thicker than the primary chordae, and among the secondary chordae in the anterior leaflet, there is generally a thicker pair of chordae, which are called the strut chordae. The strut chordae are unique for the anterior leaflet and are situated near the closure line of the anterior leaflet (Muresian, 2009, Lam et al., 1970). Moreover, the strut chordae restricts the anterior leaflet from obstructing the left ventricular outflow tract during diastole, while during systole maintains anterior leaflet geometry (Padala et al., 2010). Common for all chordae is that they are prone to rupture near the leaflet insertion point, as they are observed to be at its thinnest at this location (Van Mieghem et al., 2010). Furthermore, Lim and Boughner (1975) discovered that thinner chordae is less extensible compared to thicker chordae.

From a histological perspective, the chordae tendineae consists of an interconnected composition of collagen fibres and elastin fibres with an outer layer of endolethium (Millington-Sanders et al., 1998). Liao and Vesely (2003) discovered that the difference in collagen fibril crimping period was the reason for different extensibility between the primary and secondary chordae. A shorter fibril crimp period was observed in thicker chordae, hence leading it to extend more than thinner chordae.

Papillary Muscles

The papillary muscles (PMs) are situated in the lower portion of the left ventricular wall, and functions as an anchor point to the chordae tendineae (Brock, 1952). Based on their projected position below the commissures, the PMs are named the anterolateral and posteromedial papillary muscle (Ho, 2002). The papillary muscles help prevent leaflet prolapse and ensures coaptation by contracting with the ventricular myocardium during the systolic phase of the cardiac cycle (Votta et al., 2008, Dal-Bianco and Levine, 2013). The papillary muscles can have several different shapes and sizes. The most common form for the anterolateral PM is with a single papilla with several chordae originating from it. For the posteromedial PM, several heads are recurrent, where the different heads' chordae insert into the posterior, anterior and commissural part of the leaflets (Carpentier et al., 2010). The anterolateral PM is further supplied with blood from the left anterior descending artery and the circumflex artery. While, the posteromedial PM is either supplied by the circumflex artery or the right coronary artery, depending on coronary dominance (Estes et al., 1966).

2.4 Barlow Disease

Barlow disease is classified as a degenerative mitral valve disease and is mainly observed in patients younger than the age of 60 (Jouan et al., 2012). Barlow disease causes mitral valve prolapse, which again leads to mitral regurgitation. Furthermore, according to Iung et al. (2007), mitral regurgitation is the second most common valvular heart disease in European countries and is primarily caused by a degenerative disease.

The main characteristics related to a Barlow mitral valve is excessive leaflet tissue, billowing or prolapse of leaflet segments, myxomatous degeneration, and severe annular dilation (Hjortnaes et al., 2016). Often, multiple leaflet segments are observed to be prolapsed, and the annular saddle shape is found to be significantly flattened, compared to a normal annular shape (Apor et al., 2016). Moreover, ruptured chordae is not common for Barlow patients and was only observed in 21% of the patients studied by Hjortnaes et al. (2016). Also, as reported by Anyanwu and Adams (2007), leaflet prolapse is more frequently observed to be due to elongated chordae rather than ruptured chordae.

According to Carpentier et al. (2010), the most characteristic feature when diagnosing Barlow disease with echocardiography is the excessive leaflet tissue. In addition, during systole the bulging of the leaflets into the left atrium can be assessed, hence also an increased coaptation height toward the mitral orifice plane. It can further be observed on echocardiography, that the annular saddle shape flattens, and the mitral annulus overstretches at end systole (Apor et al., 2016). Additionally, depending on when regurgitation is observed during the cardiac cycle, echocardiography can by observing the regurgitating jet tell whether it is due to chordal elongation or rupture (Anyanwu and Adams, 2007). Moreover, clinical assessment of patients with Barlow disease is performed by auscultation, where a late systolic murmur and a midsystolic click is discovered. The midsystolic click is further presumed to be

caused by excess valvular tissue (Carpentier et al., 2010).

The work by Hjortnaes et al. (2016) studied the histological changes in the mitral valve due to Barlow disease. It was observed that the thickening of the mitral valve leaflets was caused by gathering of water absorbent proteins (proteoglycans) in the spongiosa layer, and intimal thickening of the fibrosa and atrialis (figure 2.4). Furthermore, elastin fragmentation and diminishing collagen fibres were also observed to be characteristic with Barlow mitral leaflets, leaving the collagen fibres disoriented and disrupted (Hjortnaes et al., 2016).

Specific mechanical properties for mitral valves with Barlow disease is yet to be studied. However, Barber et al. (2001a) discovered that myxomatous valves are twice as extensible compared to normal mitral valves and less stiff. Furthermore, another study by Barber et al. (2001b) studied myxomatous chordae tendineae, discovering that myxoid chordae has a 50% reduction in stiffness compared to normal chordae.

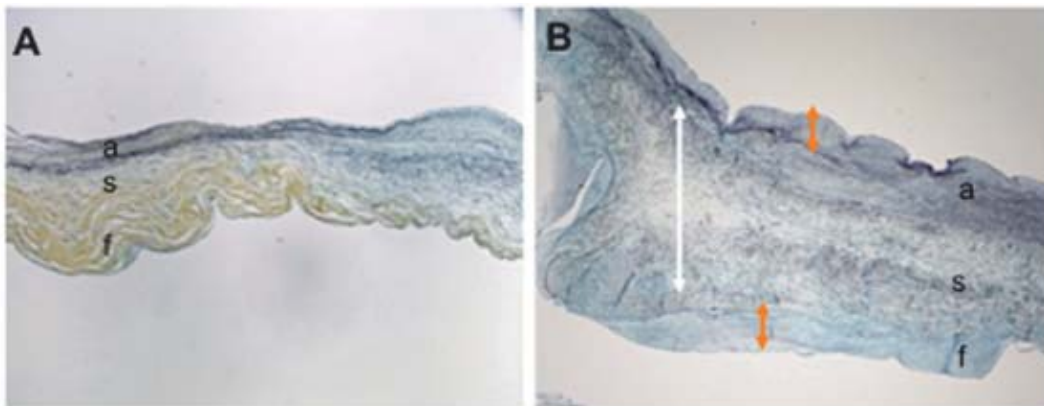


Figure 2.4: Histological comparison between a normal mitral valve leaflet and a Barlow mitral valve leaflet. (A) Normal, (B) Barlow Disease. (a) atrialis, (s) spongiosa, (f) fibrosa. Thickness change from a normal to a barlow disease infected mitral valve leaflet. Taken from (Hjortnaes et al., 2016)

2.5 Surgical Repair Techniques

In this section, the surgical procedures used to treat Barlow disease is discussed. Repairing a Barlow mitral valve is a complex procedure. However, surgical repair is preferred over replacement (Jouan et al., 2012). Furthermore, when the lesions involve annular dilation, excessive leaflet tissue, thickening of the leaflets and varying chordae defects, the whole mitral valve apparatus must be assessed.

In recent years, new and refined imaging techniques have become available. As a result, an improved understanding of mitral valve motion and function *in vivo* has been established. Leading to new non-resectional techniques, compared to the repair techniques developed by Carpentier et al. (2010). These new techniques have been termed the "American Correction" where the main goal is to obtain a functional restoration of the mitral valve. The "French Correction" however, aims to repair the mitral valve back to its anatomical origin and was developed by Alain Carpentier.

The techniques developed by Carpentier is based on extensive leaflet resection, rigid annuloplasty, and papillary muscle and chordal modifications. While, the "American Correction" involves flexible annuloplasty and artificial chordae insertions, where resection is left to a minimum and preferably not at all (Schubert et al., 2017).

Development of postoperative systolic anterior motion (SAM), poses a risk when repairing a Barlow mitral valve. Systolic anterior motion is caused by obstruction of the left ventricular outflow tract due to translation of the anterior leaflet. SAM is caused according to Carpentier et al. (1995), as a result of either excessive posterior leaflet tissue or a too small annuloplasty ring.

Annuloplasty

Due to severe annular dilation, characteristic to Barlow disease, a surgical procedure termed annuloplasty is always used during Barlow mitral valve repair (Tomsic et al., 2018). Annuloplasty aims to restore the annular geometry, leading to a reduction of the annular dilation. For Barlow patients, the size of the annuloplasty ring is usually greater than 36mm, and can often be up to 40mm in size (Adams et al., 2006). Furthermore, there have been developed different types of annuloplasty rings, some being rigid, and flexible (Apor et al., 2016). Rigid annuloplasty rings are usually used with the "French Correction," while flexible annuloplasty is used with the "American Correction" (Schubert et al., 2017).

Edge-To-Edge Techniques

The Edge-to-edge technique is performed by suturing the free edge of the mitral leaflet with the opposing leaflet edge. This technique can either be used near the commissures or in the middle portion of the leaflets, depending on where the prolapse is situated (D'Addario et al., 1998).

The double-orifice technique is an edge-to-edge technique used on Barlow patients. The method forces coaptation of the P2 and A2 region of the mitral valve leaflets (Maisano et al., 2000). As a result, the leaflet height is lowered, preventing the leaflets from bulging into the left atrium. Another consequence of the forced coaptation in the double-orifice technique is that the anterior leaflet will not experience SAM.

The triple-orifice technique is another edge-to-edge technique used on Barlow patients with multiple regurgitant jets. The procedure is described by Fucci et al. (2013) and is done by performing an edge-to-edge technique on the area where regurgitation is observed, starting with the most dominant jet. The result is a mitral valve with three asymmetric orifices. However, according to Fucci et al. (2013), several preoperative anatomical factors must be satisfied to use this technique. Moreover, SAM is prevented with this technique due to forced coaptation.

A percutaneous method named the MitralClip has been developed based on the double-orifice technique. The MitralClip is inserted through a guide catheter and into the left atrium. Instead of using sutures as in the double-orifice technique, the clip is clipped on and attached, leaving a double orifice. (Feldman et al., 2005). According to Katz et al. (2017), this minimally invasive surgical technique is mainly used when there is high surgical risk combined with severe mitral regurgitation.

Resection Techniques

There are two different types of resection techniques used to remove excessive leaflet tissue, quadrangular and triangular resection. According to Jouan et al. (2012), resection on Barlow mitral valves is mainly done on the posterior mitral leaflet.

The triangular resection technique is used when excessive tissue is mainly observed in height (Tomsic et al., 2018). As stated by Carpentier et al. (2010), triangular resection of the posterior leaflet should only be used when the prolapsed segments free margin width (B) is smaller than one-third of the base of the involved segment (A) (figure 2.5a). In addition, the triangular resection technique reduces the chance of postoperative SAM. (Schubert et al., 2017).

The quadrangular resection technique is used when excessive leaflet tissue is observed in both width and height (Tomsic et al., 2018). Or, as Carpentier et al. (2010) states, when $B > \frac{A}{3}$, (figure 2.5b). Furthermore, when excessive leaflet tissue is involved, quadrangular resection is often accompanied by sliding plasty (Jouan et al., 2012). Combining quadrangular resection with a sliding plasty also reduces the risk of postoperative SAM (Carpentier et al., 2010).

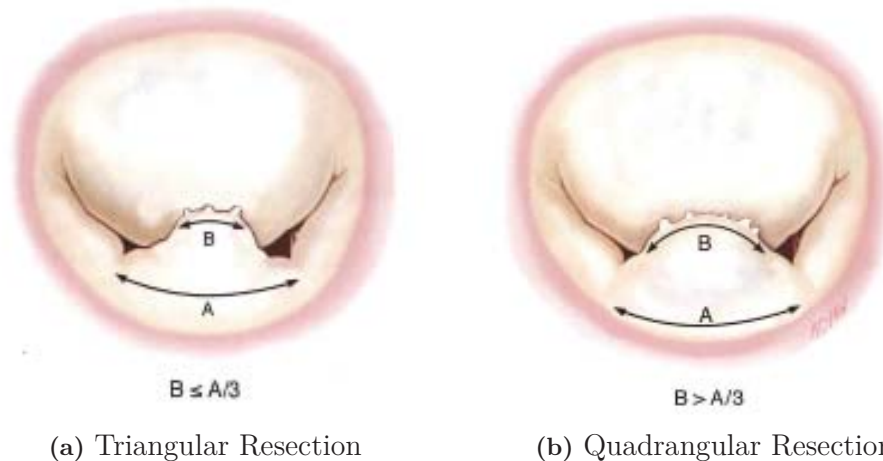


Figure 2.5: Triangular vs Quadrangular resection Technique (Carpentier et al., 2010)

Non Resection Techniques

The Loop Technique is a technique that was first described by von Oppell and Mohr (2000). Pre-measured Gore-Tex loops are connected to the papillary muscles and inserted into the free edge of the prolapsed leaflet segments (Kuntze et al., 2008). The main challenge of this technique is to optimise the required loop length in order to ensure coaptation. However, when postoperative systolic anterior motion must be avoided, leaflet resection techniques are used together with this technique. (Berger and Mohr, 2010)

Ring only repair is according to Ben Zekry et al. (2015) an effective and fast surgical procedure for Barlow patients where a major central jet is observed. The

procedure reduces the annular size, contributing to the restoration of annular dynamics. As a consequence the excessive tissue is pushed down, eliminating bulging into the left atrium as the leaflets now coapt below the mitral annulus. Concerns with this approach are as stated by Ben Zekry et al. (2015), the risk of SAM and functional mitral valve stenosis.

Lawrie et al. (2011) developed a non-resectional technique combining flexible annuloplasty and artificial chordal insertions. The technique has been termed the "American Correction," and has proven that leaflet resection is not necessary to avoid postoperative SAM (Lawrie et al., 2016).

Chordal & Papillary Muscle Repair

There are several possibilities related to chordal and papillary muscle repair. Correction methods may include: insertion of artificial chordae, chordal transposition, chordal shortening, papillary muscle sliding plasty or papillary muscle shortening (Tomsic et al., 2018). These repair techniques are used to restore prolapsed segments and leaflet geometry. As with the looping technique described above, the main challenge of using artificial chordae is the length adjustment, as a too short chordae may lead to leaflet restriction.

2.6 Patient

In this section the studied patient, his lesions and the surgical procedures performed are briefly described.

The patient is a 45 year old male who was diagnosed with Barlow disease and operated in 2017 with mitral valve repair. The patient had a severely dilated annulus with excessive leaflet tissue and mitral regurgitation. From echocardiographic findings, multiple jets of mitral regurgitation in mid to late systole were observed. The most severe regurgitation was located in the posteromedial region with billowing (A2-A3-P3) and prolapse of the P3 segment. A less severe regurgitation jet was observed in the anterolateral region due to prolapse of P1. Mitral annular disjunction (MAD) of 10 mm was observed in the P1-P2 region.

The patient received an annuloplasty ring of size 38, triangular resection and sliding of P2 in order to reduce the height of the P2 segment. Furthermore, there was inserted 2x4 neo chordae (Goretex 5-0) from each papillary muscle and to the edge of the A2 and P2 segment. Lastly, there was performed a transposition of secondary P2 chordae to the free edge of the P2 segment.

2.7 Continuum Mechanics

Kinematics

We consider a deformable body in two different instantaneous configurations Ω_0 and Ω , representing the reference and current configuration, respectively. A particle in the reference configuration Ω_0 is defined by the position vector \mathbf{X} . The position of

the same particle in the current configuration Ω is further defined by the the vector \mathbf{x} . The relationship between the two configurations is described by the deformation map relationship $\mathbf{x} = \mathbf{x}(\mathbf{X}, t)$. The deformation gradient \mathbf{F} is defined as

$$\mathbf{F} = \frac{\partial \mathbf{x}}{\partial \mathbf{X}} \quad (2.1)$$

The volume ratio is defined as $J = \det \mathbf{F}$, where $J = 1$ describes an isochoric transformation. Furthermore, the right and left Cauchy-Green tensors are defined as $\mathbf{C} = \mathbf{F}^T \mathbf{F}$ and $\mathbf{b} = \mathbf{F} \mathbf{F}^T$ respectively. Furthermore, the distortional part of the right and left Cauchy-Green can be written as $\bar{\mathbf{C}} = J^{-\frac{2}{3}} \mathbf{F}^T \mathbf{F}$ and $\bar{\mathbf{b}} = J^{-\frac{2}{3}} \mathbf{F} \mathbf{F}^T$

For an anisotropic material reinforced by a family of fibres, the fibre direction in the reference configuration is defined by the unit vector \mathbf{a}_0 . The mapping of the fibre direction from the reference configuration to the current configuration is expressed as $\mathbf{a} = \mathbf{F} \mathbf{a}_0$.

Strain-Energy Function and Stress Tensors

For hyperelastic materials a strain-energy function Ψ is introduced in order to describe the response of the material. The strain-energy function Ψ for incompressible materials can be expressed in terms of five invariants, I_1, I_2, J, I_4, I_5 as,

$$\Psi = \tilde{\Psi}(I_1, I_2, I_4, I_5) + p(1 - J), \quad (2.2)$$

where the principal invariants of \mathbf{C} , I_1, I_2, J are related to isotropic elasticity and defined as,

$$I_1 = \text{tr}(\mathbf{C}), \quad I_2 = \frac{1}{2}[I_1^2 - \text{tr}(\mathbf{C}^2)], \quad J = \sqrt{\det(\mathbf{C})}. \quad (2.3)$$

For an incompressible material the third invariant can be written as $J = 1$. The invariants I_4, I_5 describes the transversely isotropic properties of the material, expressed by the fibre direction in the reference configuration \mathbf{a}_0 and the right Cauchy-Green tensor \mathbf{C} ,

$$I_4 = \mathbf{a}_0 \cdot \mathbf{C} \mathbf{a}_0, \quad I_5 = \mathbf{a}_0 \cdot \mathbf{C}^2 \mathbf{a}_0, \quad (2.4)$$

and p is the Lagrange multiplier. The second Piola-Kirchhoff stress tensor \mathbf{S} can be derived from 2.2 giving,

$$\mathbf{S} = 2 \sum_{\substack{i=1 \\ i \neq 3}}^5 \frac{\partial \Psi}{\partial \mathbf{I}_i} \frac{\partial \mathbf{I}_i}{\partial \mathbf{C}} + p \mathbf{C}^{-1} \quad (2.5)$$

where the scalar p can be determined from the plane stress condition. In this work, we apply this constitutive model to mitral leaflets that may be considered as thin sheets, thus assuming that the stress in the out of plane direction (denoted 3-direction) S_{33} is zero leads to:

$$p = -2 \sum_{\substack{i=1 \\ i \neq 3}}^5 \frac{\partial \Psi}{\partial \mathbf{I}_i} \frac{\partial \mathbf{I}_i}{\partial C_{33}} C_{33} \quad (2.6)$$

Lastly the second Piola-Kirchhoff stress tensor \mathbf{S} can be transformed to the Cauchy stress tensor $\boldsymbol{\sigma} = \frac{1}{J}\mathbf{F}\mathbf{S}\mathbf{F}^T$ by the push-forward operation of \mathbf{S} (Prot et al., 2007). The Cauchy stress tensors for two different strain-energy functions presented in the upcoming section were derived in order to perform a material parameter fitting, which is presented in section 3.1.1.

2.8 Constitutive Models

2.8.1 Holzapfel-Gasser-Ogden

One of the two strain-energy functions concerning anisotropic hyperelastic materials, suggested in Abaqus is presented by (Holzapfel et al., 2006, 2000). The material model was developed in order to model the mechanical response of arterial layers with distributed collagen fibre orientations. The strain-energy function W is defined in terms of the deviatoric strain invariants \bar{I}_1 and \bar{I}_4 . Which are defined as,

$$\bar{I}_1 = \text{tr}\bar{\mathbf{C}}, \quad \bar{I}_4 = \mathbf{a}_0 \cdot \bar{\mathbf{C}} \cdot \mathbf{a}_0, \quad (2.7)$$

thus,

$$W(\bar{I}_1, \bar{I}_4) = C_{10}(\bar{I}_1 - 3) + \frac{1}{D} \left(\frac{(J^2) - 1}{2} - \ln(J) \right) + \frac{k_1}{2k_2} (\exp^{k_2(\bar{E})^2} - 1) \quad (2.8)$$

with,

$$\bar{E} = \kappa(\bar{I}_1 - 3) + (1 - 3\kappa)(\bar{I}_4 - 1) \quad (2.9)$$

where C_{10} , D , k_1 , k_2 and κ are temperature-dependent material parameters. C_{10} and k_1 has the dimension MPa, while k_2 is dimensionless. Furthermore, D is a material constant that controls compressibility (Prot and Skallerud, 2009). The dispersion parameter κ describes the distribution of the fibres. When $\kappa = 0$, there is no dispersion of the fibres, while, $\kappa = \frac{1}{3}$ describes an isotropic material where the fibres are randomly distributed (Abaqus, 2014).

2.8.2 May-Newman and Yin

In order to describe the mechanical response of the mitral valve leaflets. May-Newman and Yin (1998), compared experimental data extracted from biaxial tensile tests of porcine mitral valve tissue, with a transversely isotropic constitutive model. As the experimental data both for the anterior and posterior leaflets indicates a nonlinear behaviour, the suggested model in (May-Newman and Yin, 1998) has an exponential form in terms of the invariants I_1 and I_4 .

$$W(I_1, I_4) = c_0 [\exp^{c_1(I_1-3)^2 + c_2(\sqrt{I_4}-1)^4} - 1] + p(J - 1) \quad (2.10)$$

where c_i , $i=0,1,2$, are material parameters, and p is the Lagrange-multiplier.

2.8.3 Ogden Form

The Ogden strain-energy function is used in order to describe the non-linear isotropic behaviour of a hyperelastic material. When assumed incompressible the strain energy function is,

$$\Psi = \sum_{i=1}^N \frac{2\mu_i}{\alpha_i^2} (\lambda_1^{\alpha_i} + \lambda_2^{\alpha_i} + \lambda_3^{\alpha_i} - 3) \quad (2.11)$$

where μ_i and α_i are material constants and $\lambda_j^{\alpha_i}$ ($j=1,2,3$) are the principal stretches. The Ogden Form provides accurate fitting results when there is a lot of experimental test data available, generally at least both in the uniaxial and biaxial stretch directions. (Abaqus, 2014)

3

Modelling

3.1 Implementation of the Constitutive model

3.1.1 Mitral Valve Leaflets

The constitutive model used to analyse the response of the anterior and posterior leaflet from end diastole to end systole in Abaqus is presented in section 2.8.1. However, as mentioned in section 2.8.1, Abaqus only provides two anisotropic hyperelastic material models. To the author's knowledge, the two material models are not described in literature for mitral valve leaflets. Hence, in order to avoid the usage of the subroutine VUMAT, a non-linear data-fitting technique was used. The *lsqnonlin* function from the Optimisation Toolbox of Matlab was used to obtain a set of material parameters which exhibit the same response as the material model presented by May-Newman and Yin (1998). The material model developed by May-Newman and Yin (1998) was acquired from *in vitro* biaxial testing of porcine mitral valve leaflets and is described in section 2.8.2.

In the biaxial tests performed in May-Newman and Yin (1998), the leaflets fibre direction was aligned with one of the principle stretch directions, and the test samples were subjected to equibiaxial, off-biaxial and strip biaxial loading. Resulting in the material parameters described in table 3.1.

Table 3.1: Material parameters proposed by May-Newman and Yin (1998)

	c_0 (MPa)	c_1	c_2
Anterior leaflet	0.0399	4.325	1446.5
Posterior leaflet	0.0414	4.848	305.4

In order to perform the non-linear regression, the Cauchy stress tensors had to be derived from the Holzapfel-Gasser-Ogden strain-energy function and the May-Newman and Yin strain-energy function. As the mitral valve leaflets are assumed to be incompressible, equation 2.8 reduces to,

$$W(I_1, I_4) = C_{10}(I_1 - 3) + \frac{k_1}{2k_2} [\exp^{k_2(E)^2} - 1], \quad (3.1)$$

while equation 2.10 reduces to,

$$W(I_1, I_4) = c_0 [\exp^{c_1(I_1-3)^2 + c_2(\sqrt{I_4}-1)^4} - 1]. \quad (3.2)$$

To obtain the Cauchy stresses, the strain-energy functions needed to be differentiated with respect to invariants I_1 and I_4 . The stress functions W_1 and W_4 becomes,

$$W_1 = C_{10} + k_1 \kappa E [\exp^{k_2 (E)^2}] \quad (3.3)$$

$$W_4 = k_1 E (1 - 3\kappa) [\exp^{k_2 (E)^2}] \quad (3.4)$$

for equation 3.1, and

$$W_1 = 2c_0 c_1 (I_1 - 3) [\exp^{c_1 (I_1 - 3)^2 + c_2 (\sqrt{I_4} - 1)^4} - 1] \quad (3.5)$$

$$W_4 = \frac{2c_0 c_2 (\sqrt{I_4} - 3)^3}{\sqrt{I_4}} [\exp^{c_1 (I_1 - 3)^2 + c_2 (\sqrt{I_4} - 1)^4} - 1], \quad (3.6)$$

for equation 3.2. The second Piola-Kirchhoff stress tensor \mathbf{S} and the corresponding Cauchy stress tensor $\boldsymbol{\sigma}$ is derived using equation 2.5.

$$\mathbf{S} = 2W_1 \mathbf{1} + 2W_4 (\mathbf{a}_0 \times \mathbf{a}_0) + p \mathbf{C}^{-1}, \quad \boldsymbol{\sigma} = 2W_1 \mathbf{B} + 2W_4 (\mathbf{a} \times \mathbf{a}) + p \mathbf{1} \quad (3.7)$$

Recalling the plane stress state for thin sheets the second Piola-Kirchhoff stress S_{33} is zero. Hence the Lagrange multiplier defined in equation 2.6 becomes,

$$p = -2W_1 C_{33}. \quad (3.8)$$

The stress functions W_1 and W_4 , the Lagrange multiplier p and the fibre direction in the current configuration \mathbf{a} are then substituted into equation 3.7 obtaining the stress matrix,

$$\boldsymbol{\sigma} = \begin{bmatrix} \sigma_{11} & \sigma_{12} \\ \sigma_{21} & \sigma_{22} \end{bmatrix} \quad (3.9)$$

where the stress components becomes,

$$\begin{aligned} \sigma_{11} &= 2W_1 B_{11} + 2W_4 a_1 a_1 + p, & \sigma_{12} &= 2W_1 B_{12} + 2W_4 a_1 a_2, \\ \sigma_{22} &= 2W_1 B_{22} + 2W_4 a_2 a_2 + p. \end{aligned} \quad (3.10)$$

The constitutive model provided by Holzapfel et al. (2006) is fitted with the constitutive model presented by May-Newman and Yin (1998) and the material parameters in table 3.1, in order to obtain material parameters for the Holzapfel-Gasser-Ogden strain-energy function. The resulting material parameters are presented in table 3.2. Furthermore, figure 3.1 and 3.2 shows the correlations between the stress-stretch curves of the constitutive models with its respective material parameters.

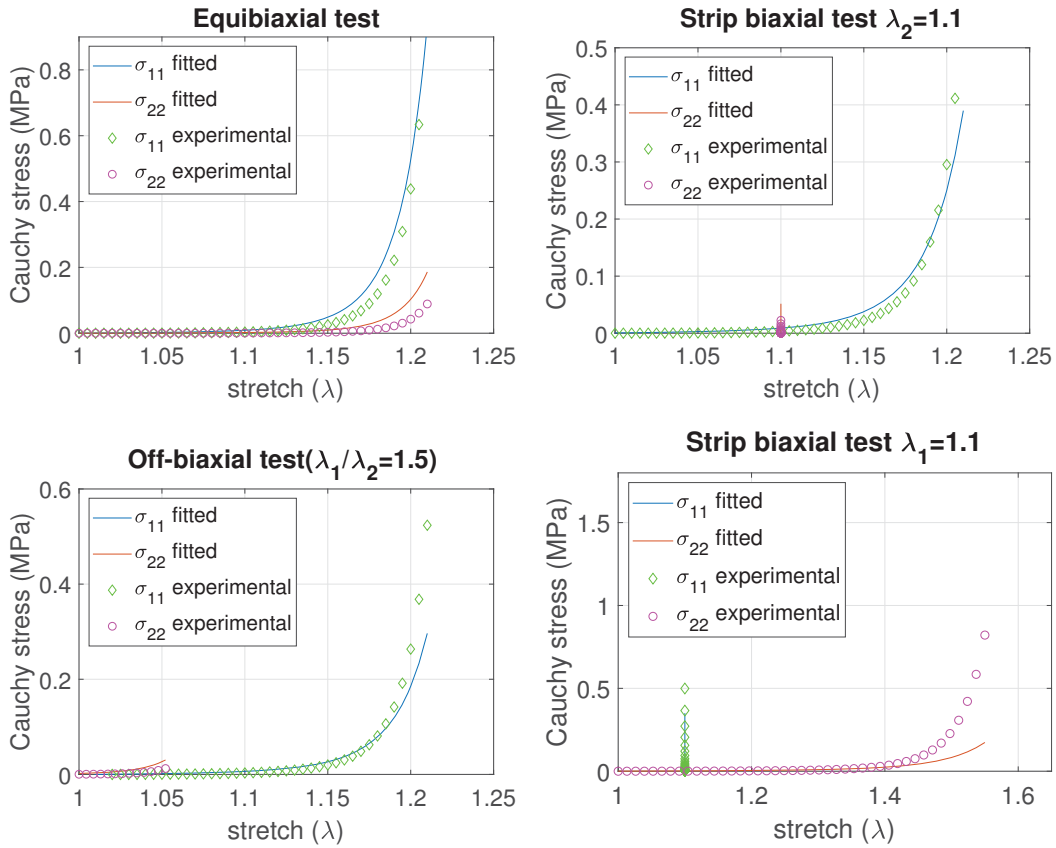


Figure 3.1: Cauchy-stress vs stretch curves for the anterior leaflet. Experimental data provided by May-Newman and Yin (1998) and nonlinear data-fitting of the constitutive model described by Holzapfel et al. (2006)

Table 3.2: Material parameters obtained from nonlinear data-fitting of experimental data provided by May-Newman and Yin (1998)

	c_{10} (MPa)	k_1 (MPa)	k_2	κ
Anterior leaflet	0.001	0.0240	50.92	0.1728
Posterior leaflet	0.001	0.0207	52.35	0.2669

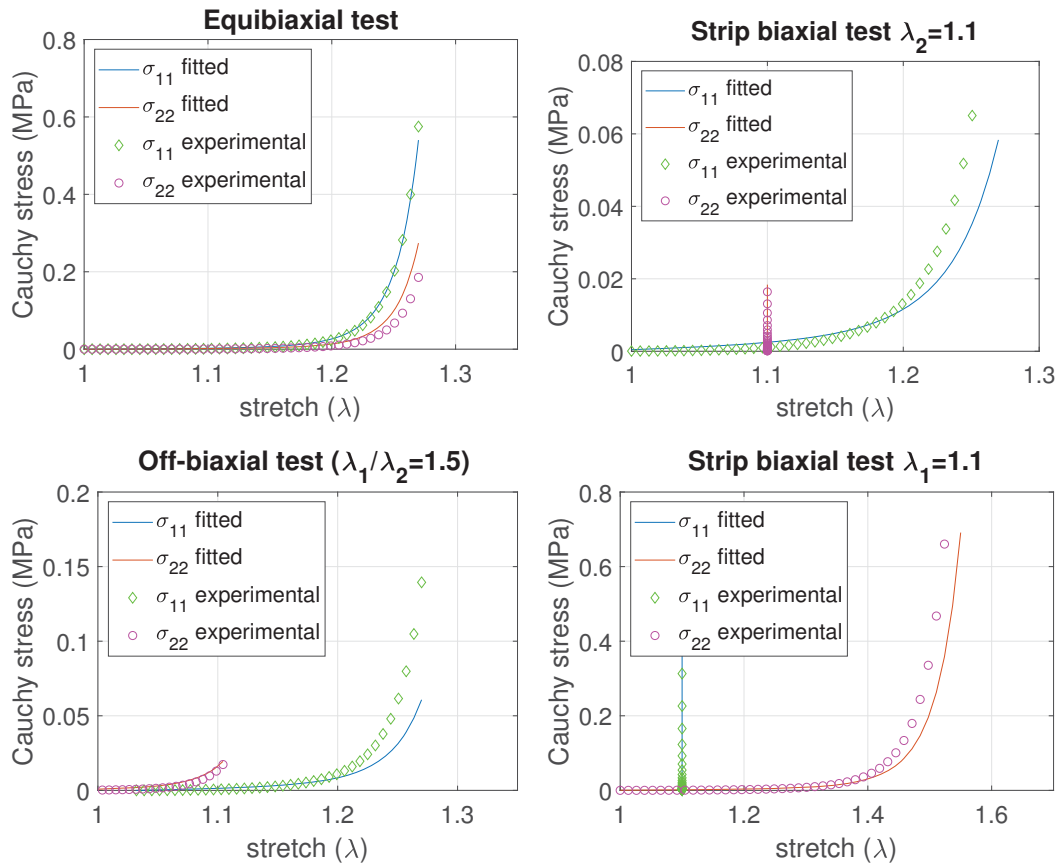


Figure 3.2: Cauchy-stress vs stretch curves for the posterior leaflet. Experimental data provided by May-Newman and Yin (1998) and nonlinear data-fitting of the constitutive model described by Holzapfel et al. (2006)

3.1.2 Chordae Tendineae

The Ogden strain energy function is used to model the response of the chordae tendineae and is presented in section 2.8.3. The material parameters used for the chordae is provided by Zuo et al. (2016), and describes the response of human chordae tendineae. These material parameters were extracted by least-square fitting on experimental data from fourteen human cadaver hearts, where a total of 106 chordae specimens were studied (Zuo et al., 2016). The chordae specimens were subjected to an uniaxial test, resulting in the material parameters presented in table 3.3.

Material parameters provided by Zuo et al. (2016) of ovine chordae tendineae were also implemented in another analysis. Human chordae were discovered to be significantly stiffer than ovine chordae (Zuo et al., 2016), and myxomatous chordae are discovered to be 50% less stiff compared to human chordae (Barber et al., 2001b). Thus, ovine material parameters were also implemented to study the difference in global response. Together with the human chordae material parameters, the ovine material parameters is presented in table 3.3.

Table 3.3: Ogden model material parameters for modelling of chordae tendineae. Anterior Marginal(AM), Anterior Strut(AS) and Posterior Marginal(PM). Human and ovine material parameters.

	Human			Ovine		
	AM	AS	PM	AM	AS	PM
$\mu_1(MPa)$	8.91	9.61	9.57	0.37	0.85	0.66
α_1	27.02	30.86	22.78	11.70	28.03	29.67
$\mu_2(MPa)$	12.19	7.99	10.61	1.79	0.21	1.37
α_2	20.91	27.65	21.68	5.00	5.47	18.25
$\mu_3(MPa)$	12.78	7.81	10.65	0.33	0.16	1.46
α_3	20.89	30.00	21.35	34.06	25.06	19.45

In figure 3.3, the nominal stress vs nominal strain is plotted for human and ovine marginal chordae tendineae. The marginal human chordae is observed to be stiffer than the marginal ovine chordae.

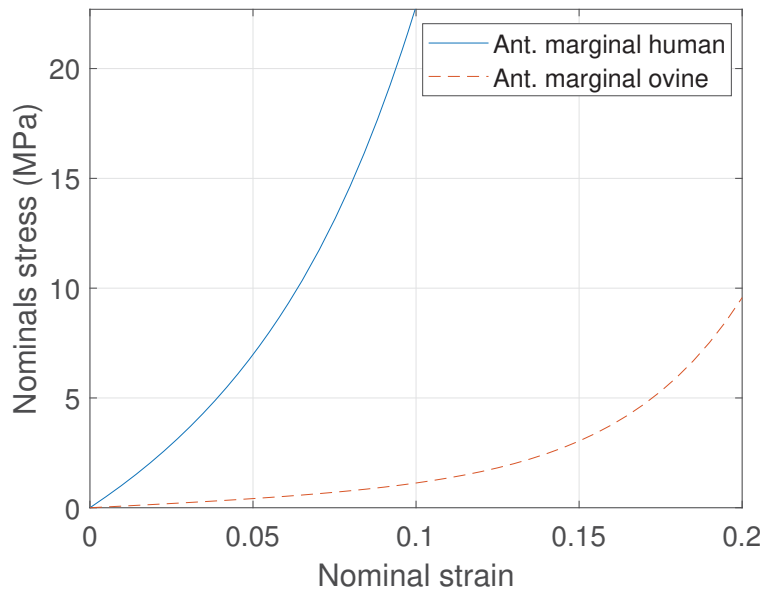


Figure 3.3: Nominal stress vs nominal strain curves. Human and ovine chordae material parameters implemented in the Ogden material model.

3.2 The Mitral Valve Model

The mitral valve has several complex anatomical features, where careful considerations have to be taken into account when modelling the apparatus as a whole. In this section, each component of the modelling is presented, from echocardiographic modelling to assigning the material orientation.

The geometrical model has been created based on echocardiographic data of a mitral valve diagnosed with Barlow disease.

3.2.1 Mitral Valve Geometry

In order to create a patient-specific mitral valve geometry, echocardiographic data from a patient with Barlow disease was studied. The echocardiogram was imported into a Matlab GUI, which enables manual extraction of geometrical points. The Matlab GUI can slice along either the x,y or z-axis, where the y-axis represents the probe axis. The different slice planes are illustrated by the box in figure 3.4, where the triad shows the mentioned directions. Furthermore, the GUI enables rotation about an axis which is parallel to the y-axis. The position of this axis can be set in the preferred location in the x,z-plane, enabling the possibility to study several rotational views, which is essential when locating the commissural region.

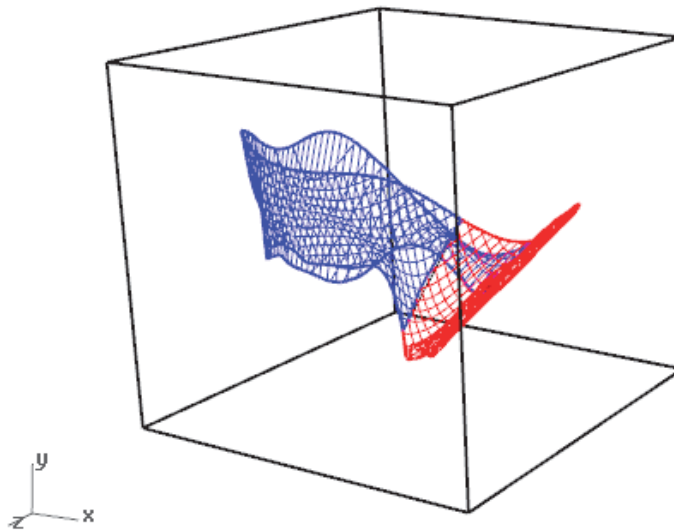


Figure 3.4: Configuration of the mitral valve in the GUI related to echocardiographic data. The red and the blue part describes the anterior and posterior leaflet respectively. The cube represents the different views it is possible to slice through the echocardiogram.

The modelled geometry is based on the end-diastolic configuration of the mitral valve, where points are extracted from different echocardiographic views (figure 3.4).

In end-diastole, the anterior and posterior leaflet is constructed by picking points from the leaflets free edge, leaflet tissue and annulus. The tissue points are situated between the free edge and the annulus, and were taken from the middle of the leaflet represented by the red circles in figure 3.5, enabling the leaflet thickness to be offset in both directions. To get a full representation of the leaflets, annulus and papillary muscles several views are combined.

The annulus is made by spline interpolation of data points, extracted from the rotational view in the Matlab GUI. The annulus points are found by first locating the aortic valve, which is in connection with the annulus, using this as a reference configuration, two points on each side are extracted every 30° , creating twelve individual points describing the annular perimeter. Lastly, the papillary muscle tips are identified, representing the papillary muscle as a whole. The papillary muscles further serve as the attachment point for the chordae.

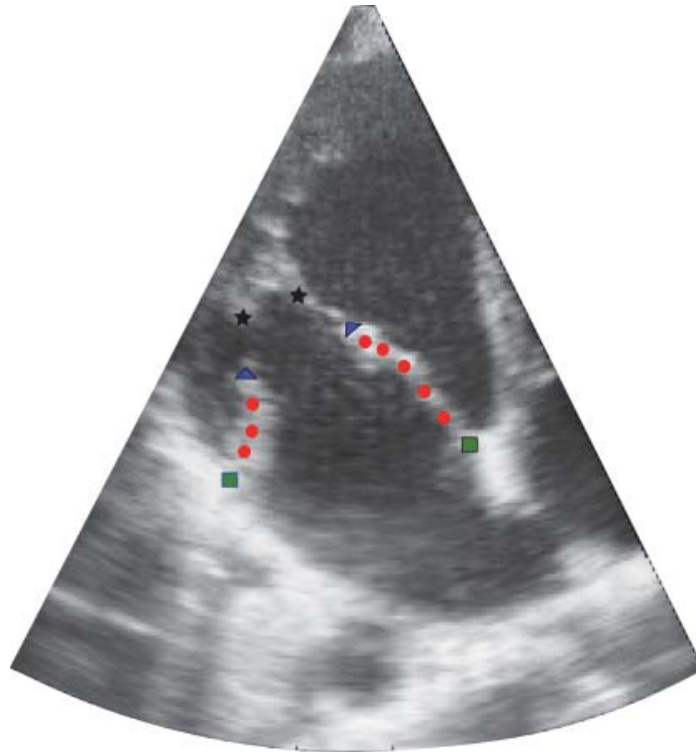


Figure 3.5: Explanation of the anatomical components on an echocardiographic image, end-diastolic configuration. Cross-sectional view along the x-axis. Papillary Muscle Tips (star), Posterior leaflet edge (left triangle), Anterior leaflet edge (right triangle), Annulus (square). Tissue points (circles)

The created point cloud is then imported into the CAD software Rhino, where the annulus line and free edge line is constructed using cubic spline interpolation (figure 3.6). The extracted tissue points are then used to guide a non-uniform rational B-spline (NURBS) surface between the annulus and free edge, creating the final geometry depicted in figure 3.7.

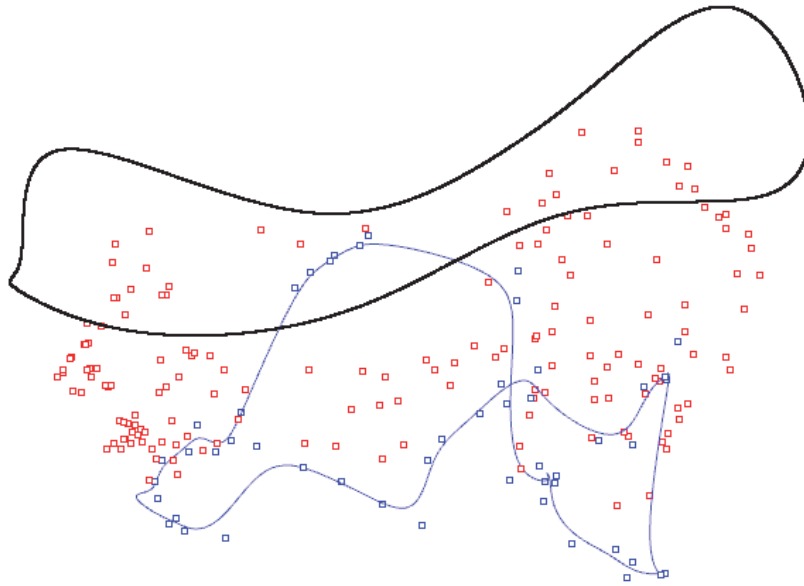


Figure 3.6: Point cloud extracted from echocardiography. Annulus (black line), Tissue points (red) and leaflet free edge (blue line)

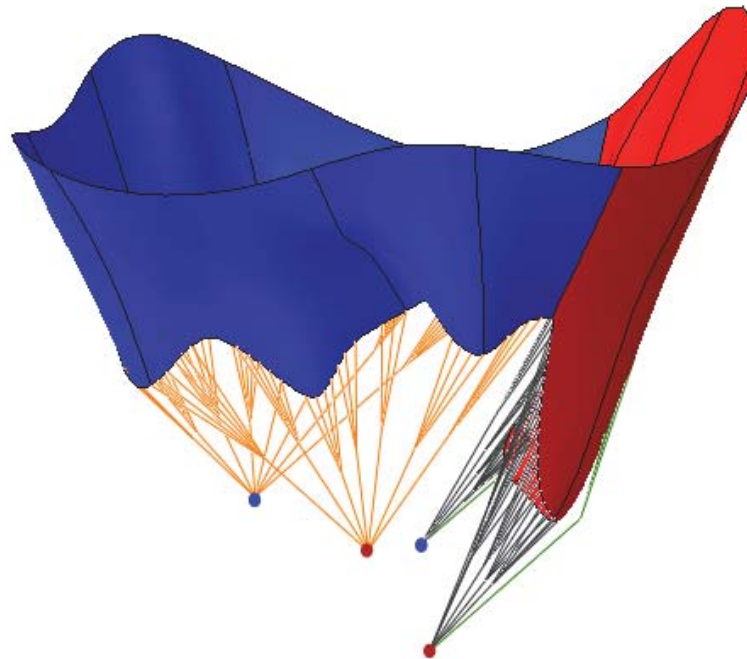


Figure 3.7: FE geometry created from echocardiographic data. Posterior leaflet (blue), anterior leaflet (red), Posterior marginal chordae (orange), anterior marginal chordae (black), strut chordae (green).

The four nodes situated below the leaflets in figure 3.7, describes the placement of the papillary muscles. Where the blue nodes represent the anterolateral papillary muscle, and the red nodes represent the posteromedial papillary muscle.

In order to interpret the results, a model of the mitral valve leaflets at peak systolic pressure was created from the echocardiographic data. The same method, as described above, is used to get the end-diastolic configuration. Obtaining a good representation near the commissures at peak systole is difficult. Thus only the middle of the leaflets have been created (figure 3.8). Figure 3.8 shows the peak systolic configuration of the mitral valve, where the purple section is where the FE model at peak systole is compared to the echocardiographic data in section 4.4.

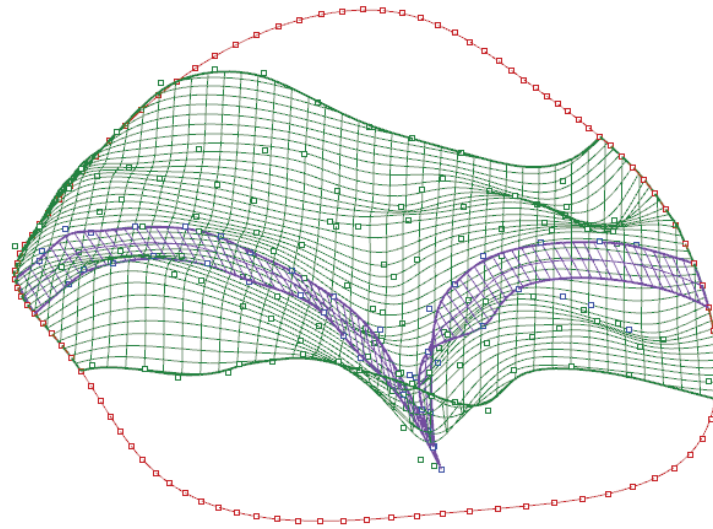


Figure 3.8: Geometry constructed from echocardiographic points at peak systole

3.2.2 Chordae Modelling

The chordae tendineae originate from the papillary muscles and insert into either the leaflet edge, rough zone or the basal portion of the mitral valve leaflets. However, in this thesis, the basal chordae are not considered. Hence only the marginal and strut chordae have been modelled. The marginal chordae insert into the free edge of both the anterior and posterior leaflet, while the strut chordae insert into the anterior leaflet only.

Twelve marginal chordae were modelled to originate from both the anterolateral and posteromedial papillary muscle. Each marginal chordae were then split in a fan-like manner, inserting into the leaflet edge with about five different insertion points as described by Kunzelman et al. (1994). The branching was mainly done in order to simulate a more anatomically correct model, where the branch origin was set between the papillary muscle and the free edge (figure 3.7). Moreover, the branching led to a redistribution of stress on the leaflet edge, which made the finite element analysis more numerically stable, preventing excessively distorted elements.

The strut chordae is inserted into the anterior leaflet rough zone, which is situated between the annulus and the free edge. Similar to the marginal chordae,

the strut chordae branches out in a fan-like manner. The branching is distributed to the nearby nodes of the main leaflet insertion point.

The cross-sectional areas for human marginal and strut chordae was modelled to be 0.25 mm^2 and 1.27 mm^2 respectively. While for the ovine chordae the cross-sectional areas were modelled to be 0.26 mm^2 and 0.6 mm^2 . Here, the chordae has been assumed to be circular and calculated with the cross-sectional diameter presented in the paper published by Zuo et al. (2016), which studied human and ovine cadaver hearts.

3.2.3 Thickness Modelling

The mitral valve leaflets are from a histological perspective a trilaminar structure, consisting of the spongiosa, fibrosa, and atrialis. However, the three layers work in concert and the mechanical properties used in this thesis represents each leaflet as one entity. Hence the leaflets are modelled as one undifferentiated layer, with a uniform thickness. Furthermore, as Barlow patients are observed to have an increased leaflet thickness due to an accumulation of GAGs in the spongiosa layer and intimal thickening of the atrialis and fibrosa, the thickness is modelled to be 3 mm. The chosen thickness is due to the study performed by Hjortnaes et al. (2016), which discovered that the overall leaflet thickness for Barlow mitral valves was $2885 \pm 85 \mu\text{m}$. The leaflets were further modelled with a density of 1000 kg/m^3 .

3.2.4 Contact Modelling

A general contact algorithm was used in the finite element analysis, where contact was set to all with self. Moreover, the mechanical contact properties used was tangential and normal behaviour. The tangential behaviour was set to frictionless, and the normal contact property was a hard contact condition (Abaqus, 2014).

3.2.5 Boundary Conditions

In order to model the patient-specific boundary conditions, the dynamics of the papillary muscle tips and the annulus have been studied using *in vivo* echocardiographic data. The geometry of the annulus and the positions of the PMs are recorded for all time-frames, between end-diastole and end-systole, as illustrated in 3.9. The annulus was constructed using a cubic spline interpolation between several recorded data points from the acquired images, as described in section 3.2.1. Between each configuration, a linear interpolation is performed, creating a continuously modelled movement between each time-frame. Hence, the entire movement of the annulus and papillary muscles from end-diastole to end-systole is described. The modelled movement is then implemented into an Abaqus user subroutine provided by Assoc. Prof. Victorien Prot called VDISP.



Figure 3.9: Annular configurations during systole

3.2.6 Load History

In order to model the mitral valve response during the cardiac cycle, the leaflets' ventricular surface was subjected to a load amplitude with patient-specific peak pressure. The peak systolic pressure observed in the studied patient was 136 mmHg, which is equivalent to 18.13 kPa. Hence, the patient's systolic blood pressure is not equal to the normal systolic blood pressure of a healthy heart (120mmHg) (Staessen et al., 2017). As a consequence, the mitral valve leaflets are subjected to higher overall loads. Moreover, the amplitude curve shown in Figure 3.10 is fitted in order to follow the echocardiographic time-frames and the pressure curve presented in figure 2.2. The last time-frame modelled in the subroutine is at the moment the aortic valve opens. Hence the pressure at this point was modelled to be approximately 100 mmHg (figure 2.2). As the amplitude curve follows the annular and papillary muscle movement, the applied load has a close to reality behaviour.

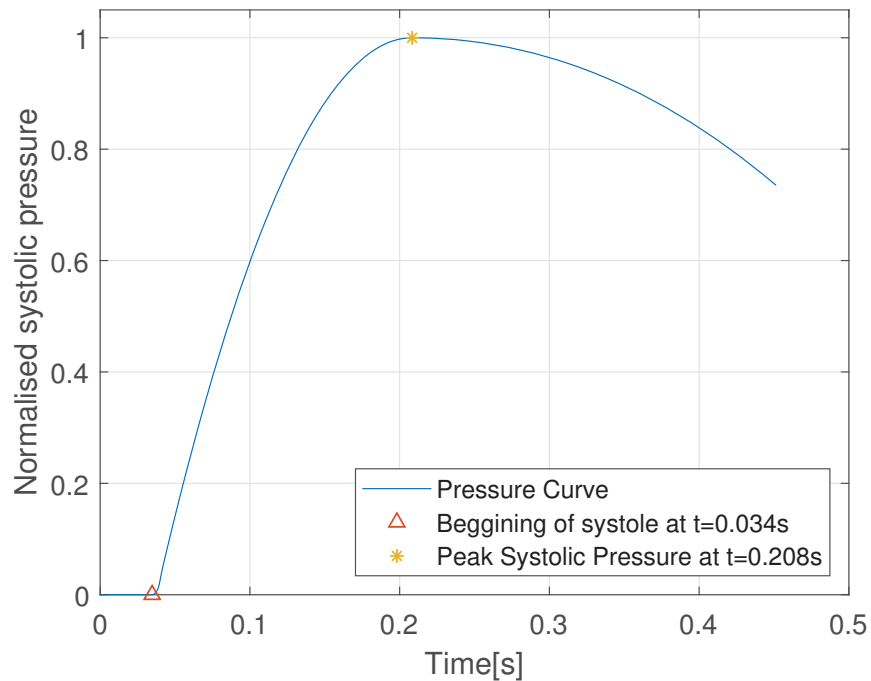


Figure 3.10: Load amplitude curve in the cardiac cycle

3.2.7 Material Orientation

The material orientation applied to the mitral valve leaflets in this thesis is obtained from small angle light scattering (SALS) data presented by Cochran et al. (1991). In figure 3.11, the mean collagen fibre direction is observed to be perpendicular to the annulus near the commissures, and parallel to the annulus at the middle of the leaflets. Moreover, the fibre direction is observed to gradually rotate from parallel to perpendicular towards the commissures.

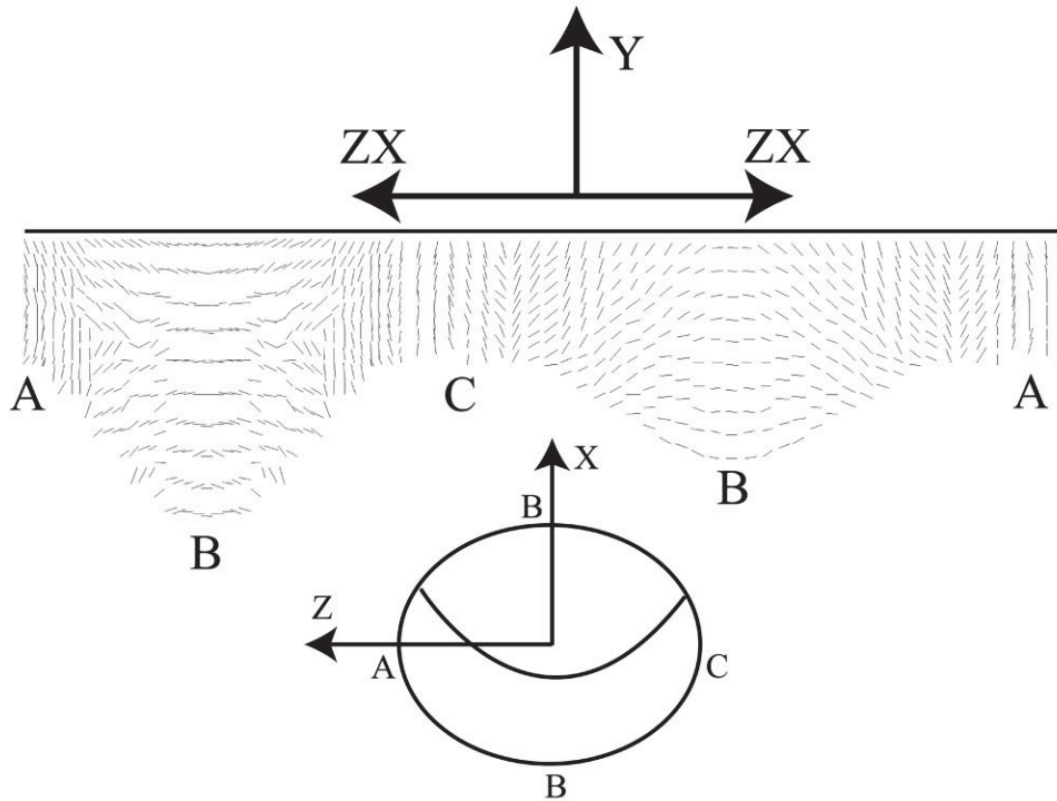
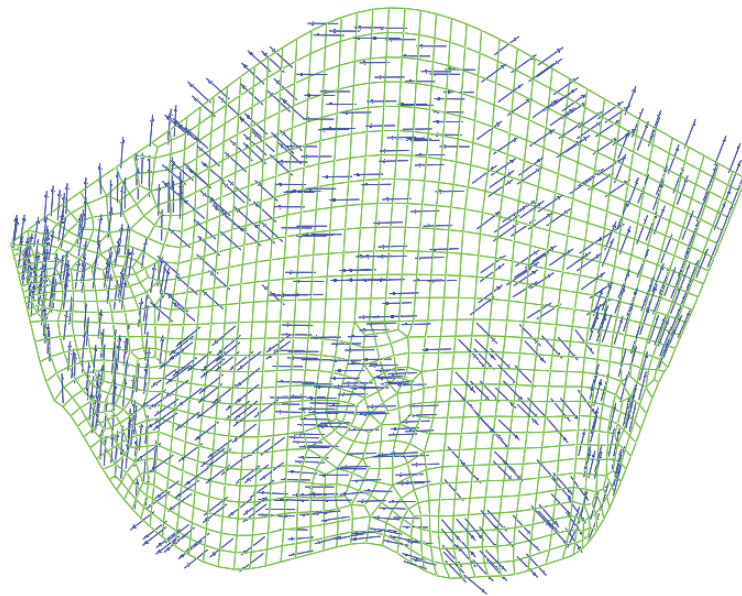
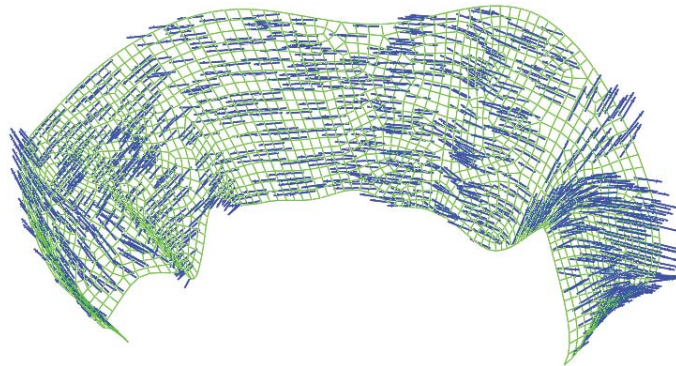


Figure 3.11: Collagen fibre direction for both the anterior and posterior leaflet. (Einstein et al., 2005, Cochran et al., 1991)

Implementation of the fibre direction presented by Cochran et al. (1991) in Abaqus is done by partitioning the leaflet into several regions. Then assigning a material orientation to each individual partitioned region. The fibre direction is approximated by creating a vector between two nodes for each partitioned region, where the vector points in the desired fibre direction. In figure 3.12, the primary axis is plotted on the undeformed configuration of the posterior and anterior leaflet. The normal axis is further defined to be normal to the leaflet surface, leaving the secondary axis to be the cross product between the primary and normal axis.



(a) Anterior leaflet



(b) Posterior Leaflet

Figure 3.12: Material orientation of the anterior and posterior leaflet, respectively.

3.2.8 Element Types

For the anterior and posterior leaflet, the general-purpose shell element S4 is used. The S4 shell element is based on thick shell theory and is defined for finite membrane strains and arbitrarily large rotations. Hence, the S4 element is applicable for large-strain analysis. Furthermore, the S4 element is based on a normal integration rule with four integration points. (Abaqus, 2014, Laulusa et al., 2006)

Additionally, the chordae tendineae is modelled with two-noded 3D truss elements (T3D2).

4

Results

4.1 Measurements of FE Geometry

The geometry modelled from echocardiographic data has been compared with measurements obtained in literature of a Barlow mitral valve and a healthy mitral valve. The goal being to verify the geometry with anatomical measurements of Barlow mitral valves. Furthermore, the Barlow mitral valve studied herein shows abnormal features such as excessive tissue and a severely dilated annulus. The finite element model is measured in both the end-diastolic and end-systolic configuration. In table 4.1 the measurements are presented.

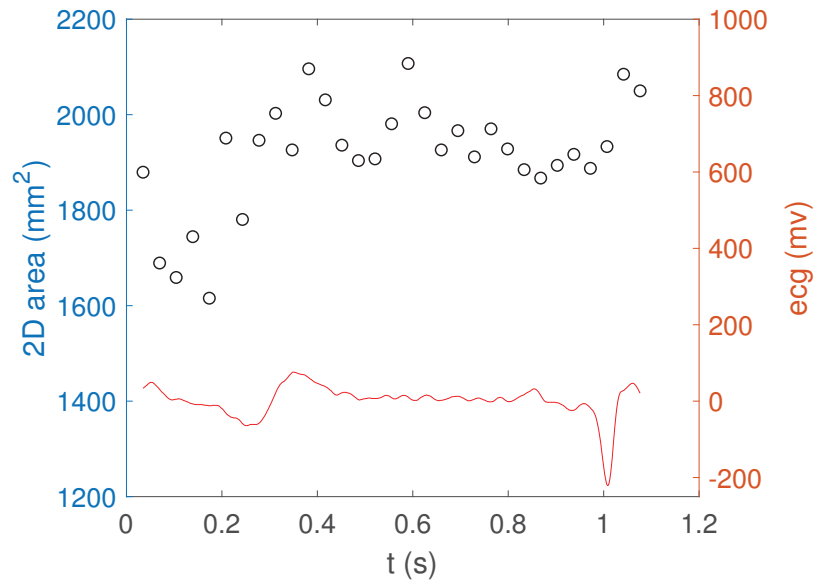
Table 4.1: Mitral valve measurements of the FE model, compared with measurements from literature both *in vitro* and from 3D echocardiography. (Kunzelman et al., 1994, Grewal et al., 2010, Chandra et al., 2011, Apor et al., 2016)

	FE model		From Literature		
	ED	PS	Barlow (S)	Barlow (D)	Healthy (D)
Annular perimeter (mm)	170	160	158 ±19	148±17	82 ±7
IC diameter (mm)	50.83	-	45±9	46.6 ±5	39.5 ±3.4
AP diameter (mm)	45.02	-	44 ±8	37.3 ±6	32.2 ±3.6
Anterior leaflet height (mm)	32.07	-	-	-	20 ±2
Posterior leaflet height (mm)	19.85	-	-	-	12 ±1
AC height (mm)	10.03	-	-	-	7 ±1
PC height (mm)	12.05	-	-	-	7 ±1
3D annular area (mm ²)	2100	1625	-	1500 ±280	-
3D total leaflet area (mm ²)	2645	-	2302 ±455	1850 ±490	-
Anterior leaflet area (mm ²)	1145	-	1162 ±276	-	-
Posterior leaflet area (mm ²)	1500	-	1175 ±306	-	-

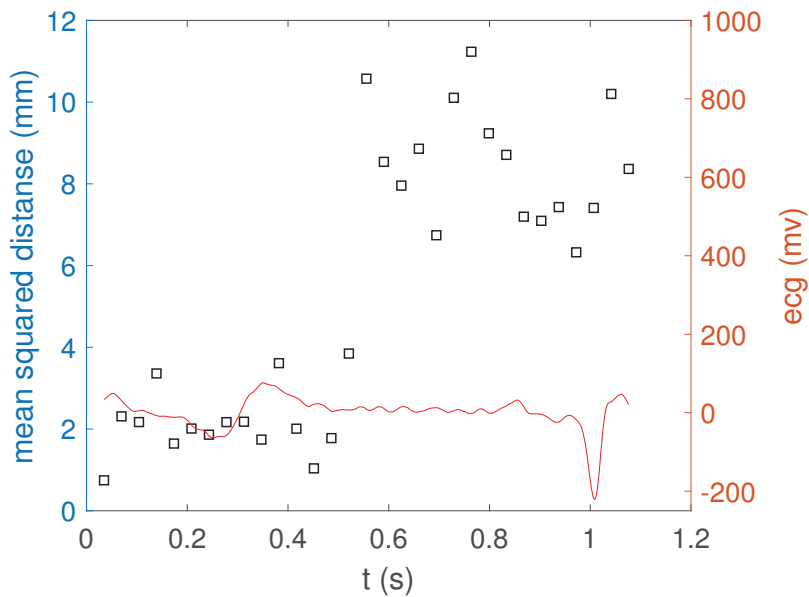
IC- Intercommisural, AP-Anteroposterior, AC-Anterolateral Commissure, PC-Posteriomedial commissure, ED-End Diastole, PS-Peak Systole, S-Systole, D-Diastole.

As can be seen in table 4.1, the FE model measurements coincide with the upper limits of the diastolic Barlow measures extracted from literature (Apor et al., 2016, Grewal et al., 2010). Furthermore, for each time step, a mean annulus plane was calculated. Then, the annulus was projected onto this mean plane and a two-dimensional (2D) area was computed and plotted against time in figure 4.1a. This plot shows how much the annulus dilates throughout the whole cardiac cycle. Then, the mean squared distance of the annulus to this plane was computed and plotted

in figure 4.1b, showing how much the annulus flattens during one full cardiac cycle. The t-wave on the ECG signal is observed prior to 0.5s, hence the measurements in figure 4.1 represents systole from 0 to 0.5s. As can be seen in figure 4.1b, the annulus is distinctly flattened during systole. Note that the end-diastolic configuration is the very last time step in figure 4.1.



(a) 2D annular area plotted against time(s)



(b) Mean squared distance of the annulus to its mean-plane

Figure 4.1: Annular measurements and shape

4.2 Global Response

In this section the global response of the finite element analysis is presented. Figure 4.2 depicts the valve closure from end-diastole to end-systole observed from the left atrium.

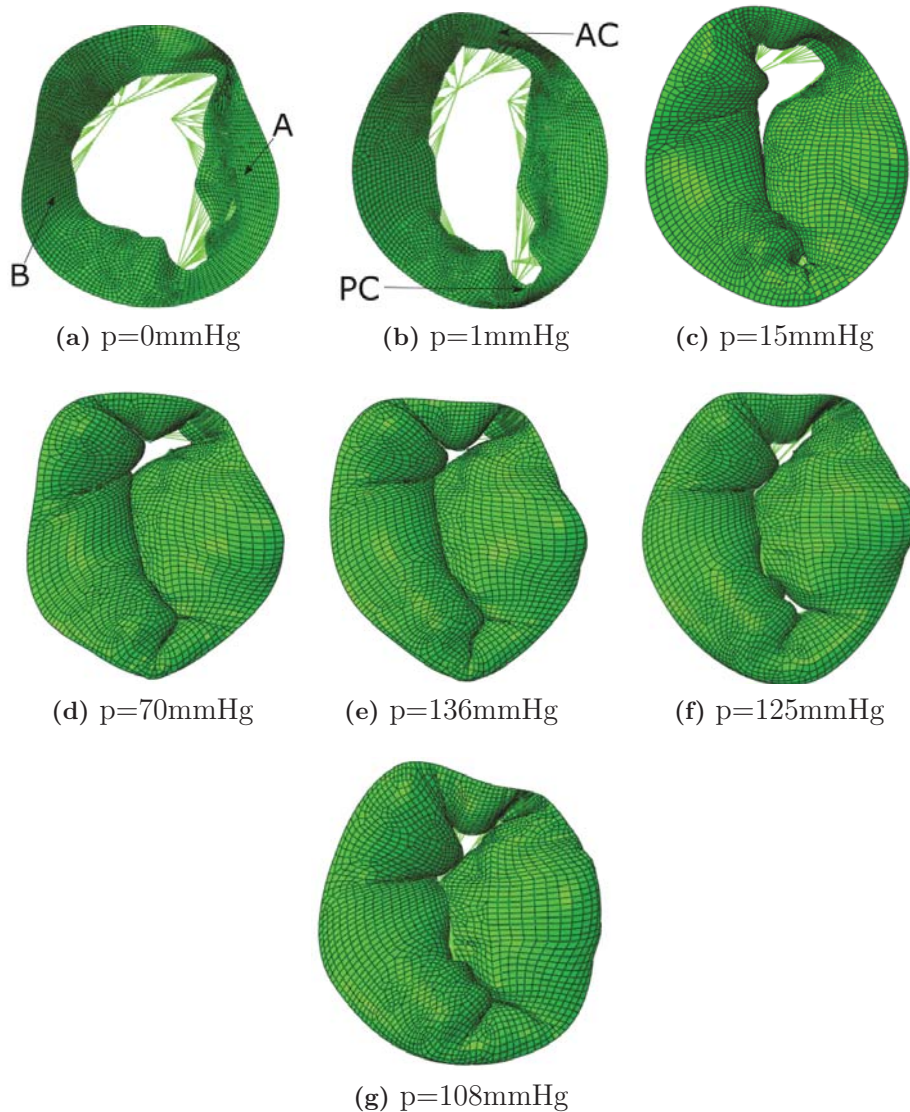


Figure 4.2: Valve closure of finite element model from end-diastole to end-systole. (a) End-diastolic configuration, $p=0\text{ mmHg}$. (b) $p=1\text{ mmHg}$. (c) First observation of coapting surfaces, $p=15\text{ mmHg}$. (d) $p=70\text{ mmHg}$. (e) Peak systolic pressure, $p=136\text{mmHg}$ (f) Late systolic regurgitation, $p=125\text{mmHg}$ (g) End-systolic configuration, $p=108\text{ mmHg}$

From figure 4.2 it can firstly be observed regurgitation at the anterolateral region (A1-P1) throughout the whole analysis. Secondly, the annular motion is

clearly observed in figure 4.2. Lastly, in figure 4.2f, a late systolic regurgitation can be observed near the posteromedial commissure (A3-P3). Figure 4.3 depicts a cut-view, showing what appears to be prolapse at the posteromedial side of the P2 segment. The prolapse is observed at the same time as the late systolic regurgitation in figure 4.2f. Note that the prolapse is present until the end of systole.

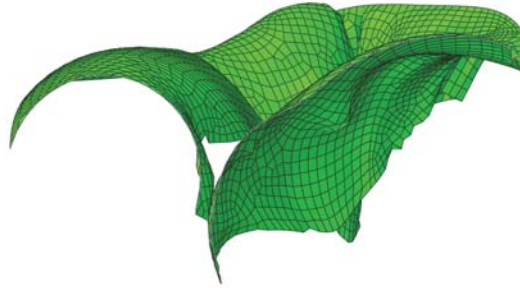


Figure 4.3: Cut-view of prolapse at the posteromedial side of the P2 segment

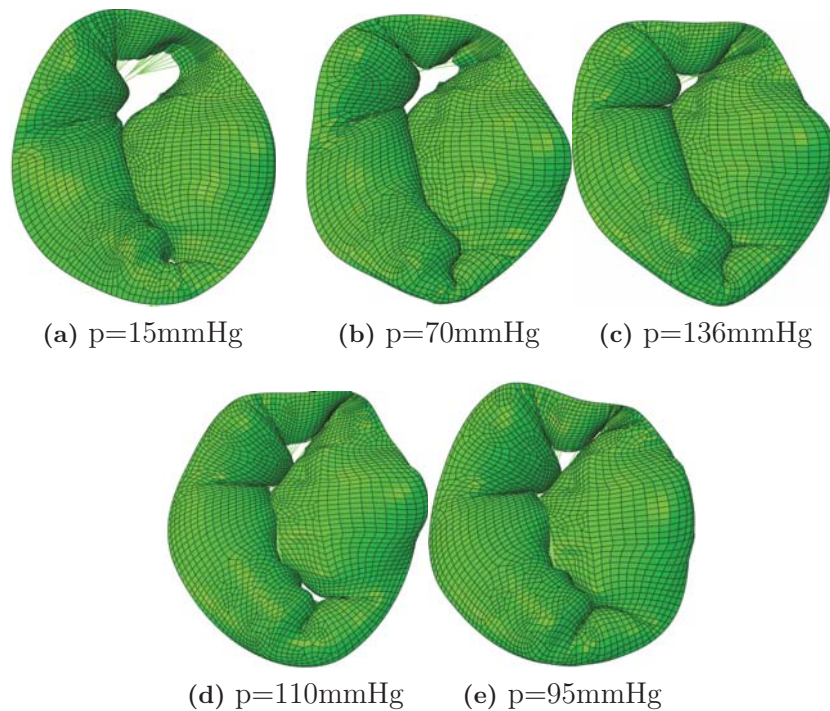


Figure 4.4: Valve closure of finite element model from end-diastole to end-systole (Ovine chordae material parameters). (a) End-diastolic configuration, $p=0$ mmHg. (b) $p=1$ mmHg. (c) First observation of coapting surfaces, $p=15$ mmHg. (d) $p=70$ mmHg. (e) Peak systolic pressure, $p=136$ mmHg (f) Late systolic regurgitation, $p=110$ mmHg (g) End-systolic configuration, $p=95$ mmHg

Figure 4.4 shows the mitral valve closure when ovine chordae material parameters are implemented. The response is observed to be very similar to the analysis

with human chordae parameters, with regurgitation and prolapse at the same locations. However, displacements are higher for the ovine model, which is further discussed in section 4.3.

4.3 Displacements

The norm of the displacement of point A and B (figure 4.5a) are plotted against time in figure 4.5. Prior to the pressure being applied, it is observed that point A and B move without any loading. These movements are due to the annular and papillary muscle dynamics. Moreover, figure 4.5 shows that as the analysis approaches 0.1s ($p=81$ mmHg) the leaflets tend to oscillate very little for the rest of the analysis. Lastly, in figure 4.5, the displacements of point A and B are plotted to compare the leaflet response when ovine and human chordae material parameters are implemented.

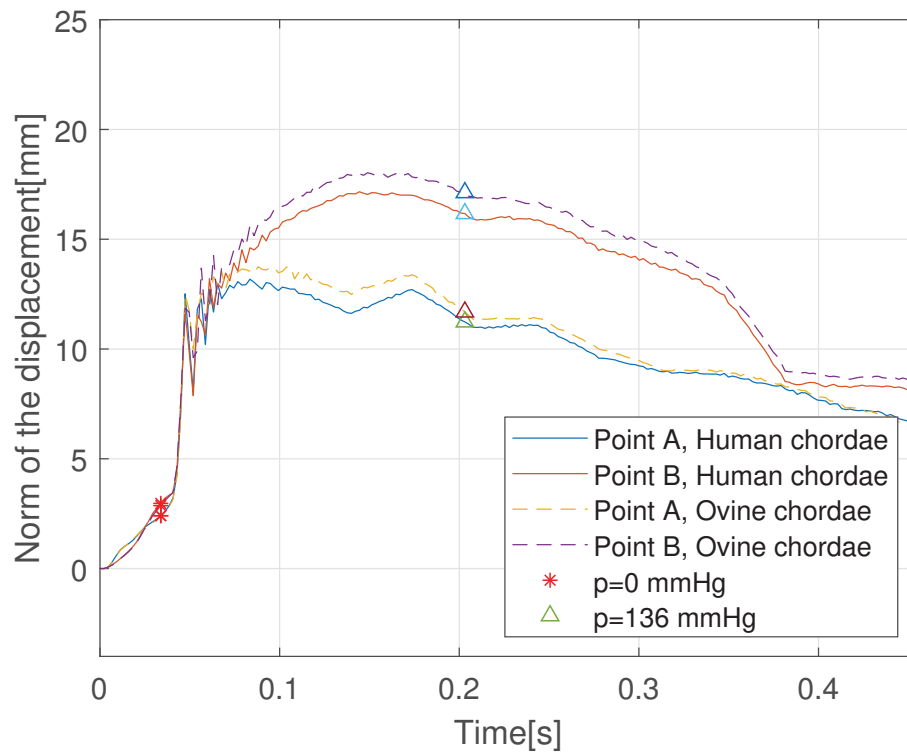


Figure 4.5: Norm of the displacement of point A and B, obtained with leaflet parameters from table 3.1, and human and ovine chordae material parameters from table 3.3

4.4 Comparison with Three-Dimensional Echocardiographic Data

Figure 4.6 shows the global response at the A2-P2 region of the leaflet compared to echocardiography at peak systole. As can be seen, there is a very good correspondence between the echocardiographic measurements and the mitral valve models.

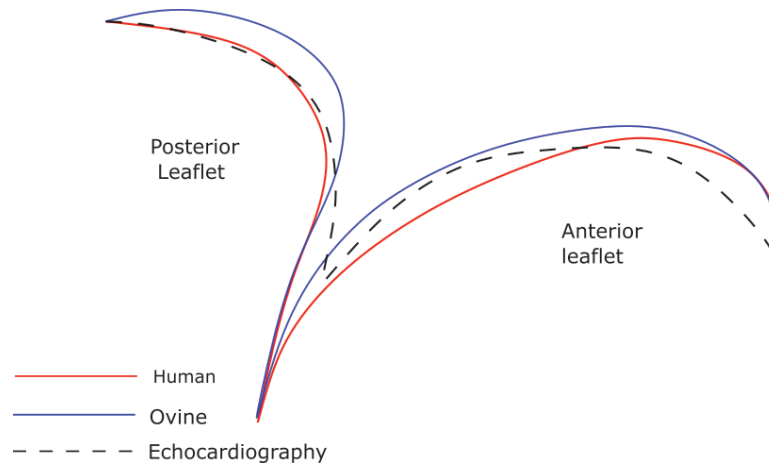


Figure 4.6: Comparison between finite element models and echocardiography along the A2-P2 leaflets at peak systolic pressure $p=136\text{mmHg}$, using human and ovine chordae material parameters.

4.5 Stresses

The leaflets von Mises stresses are plotted at peak systole (18.13 kPa) in figure 4.7. High stress regions are observed near the location where the strut chordae is inserted into the anterior leaflet and near the fibrous trigones. At the marginal chordae insertion points there is also observed high von Mises stresses. However, high stresses are also observed due to the implementation of material orientations, and is further discussed in the discussion section.

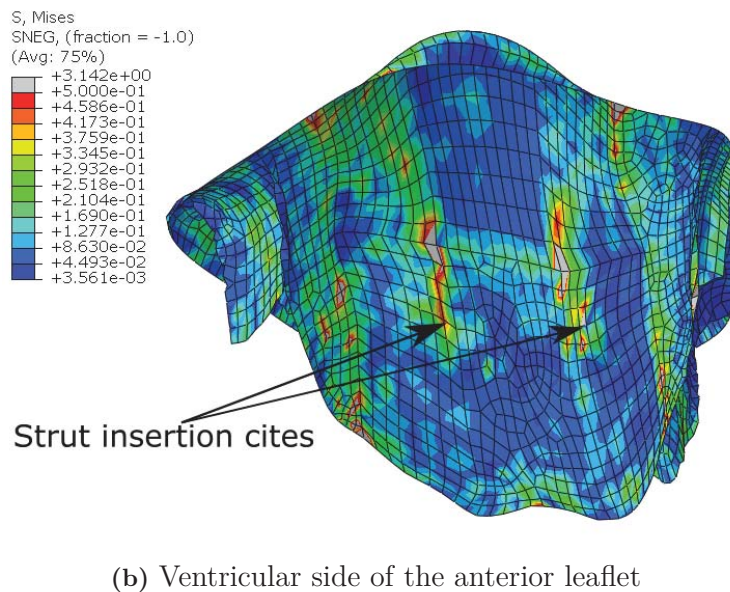
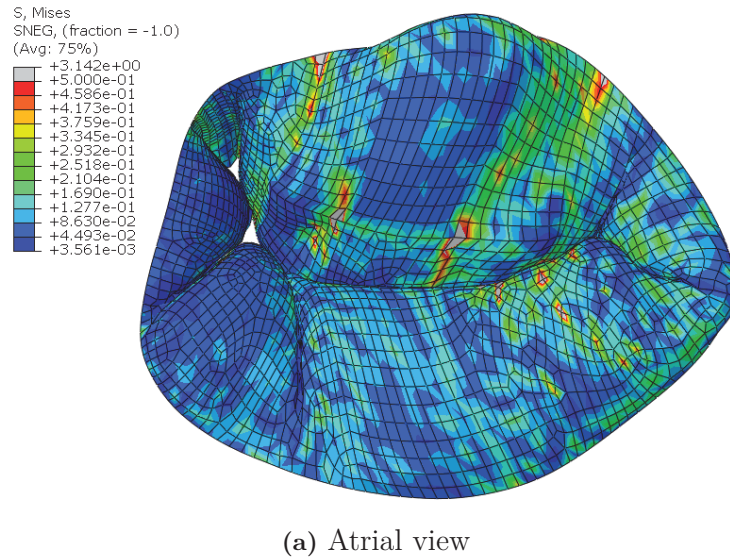
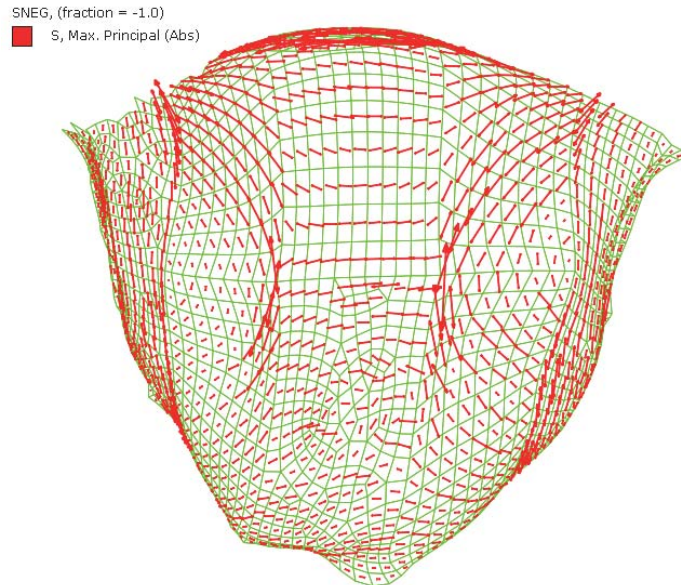


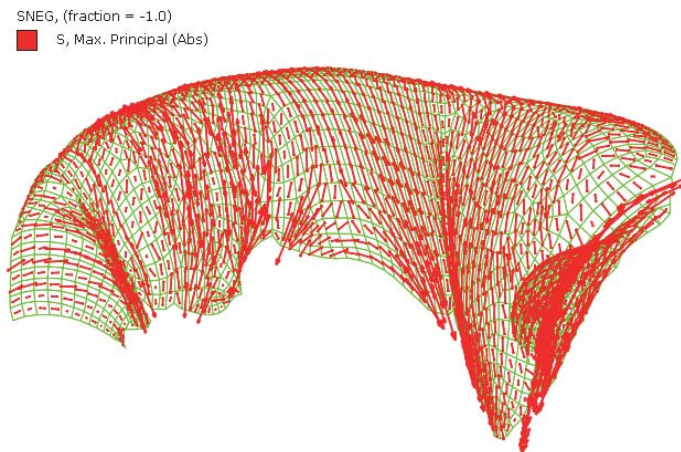
Figure 4.7: von Mises stress of the mitral valve leaflets (MPa)

The maximum principal stress direction is plotted on the deformed leaflets in figure 4.8. As can be seen from figure 4.8a, the maximum principal stress is aligned

with the modelled material orientation for the anterior leaflet. The maximum principal stress for the entire posterior leaflet is observed in figure 4.8b to be perpendicular to the annulus. As a result, in the posterior leaflet, the maximum principal stress only aligns with the assigned material orientation near the commissures.



(a) Anterior leaflet



(b) Posterior leaflet - atrial view

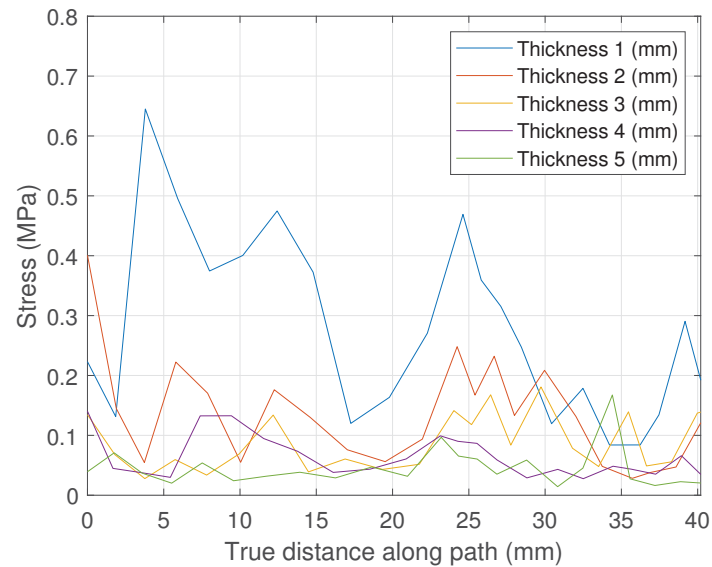
Figure 4.8: Maximum principal stress plotted on deformed mitral valve leaflets.

4.6 Thickness Study

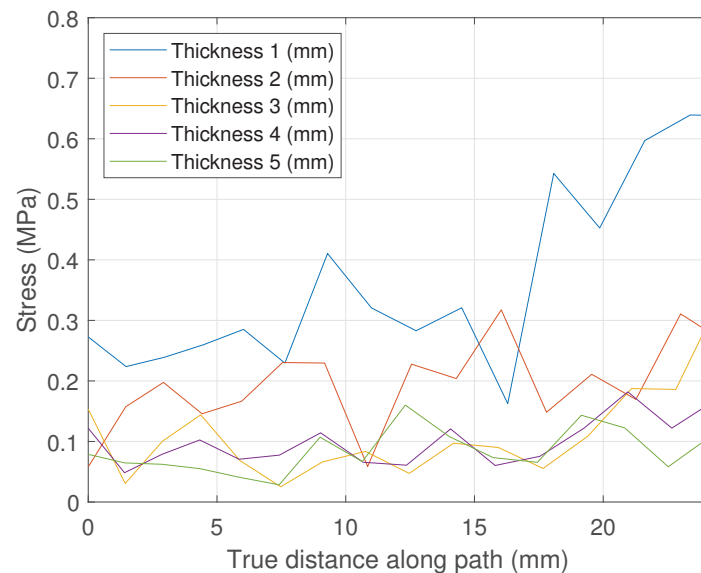
In this section, the effect of different leaflet thicknesses is presented. As a Barlow mitral valve is observed to have an approximate overall leaflet thickness of 3 mm, it is interesting to study how different leaflet thicknesses behaves. The mitral valve

leaflets presented in this section is modelled with overall thicknesses of 1, 2, 3, 4 and 5 mm.

In order to study the difference in stresses due to leaflet thickness, two paths were created in Abaqus. The paths were created from the annulus to the free edge for the middle portions of the posterior and anterior leaflet. Then, the stresses along these paths were studied at the peak systolic configuration.



(a) Anterior leaflet



(b) Posterior leaflet

Figure 4.9: Stress along path for different leaflet thicknesses

As can be observed from figure 4.9, there is a substantial decrease in stress when comparing the leaflets modelled with a thickness of 1mm and 2mm. However, as the thickness is increased the stresses are observed to be more similar. In table

4.2, the mean stresses for each thickness is presented, as well as the maximum reduction in section thickness for both point A and B. Lastly, in figure 4.10, the section thickness at point A throughout the analysis is plotted for every modelled thickness. The reduction in thicknesses during the analyses are observed to be approximately 40% for point A, and 35% for point B.

Table 4.2: Mean stress along path and maximum $\Delta_{reduction}$ in section thickness for different leaflet thicknesses. AL-anterior leaflet, PL-posterior leaflet

Thickness	1mm	2mm	3mm	4mm	5mm
Mean stress AL (MPa)	0.3673	0.1937	0.1105	0.0992	0.0838
Mean stress PL (MPa)	0.2782	0.1505	0.0899	0.0647	0.0458
max $\Delta_{reduction}$ AL (mm)	0.43	0.82	1.23	1.59	1.945
max $\Delta_{reduction}$ PL (mm)	0.37	0.73	1.03	1.42	1.62

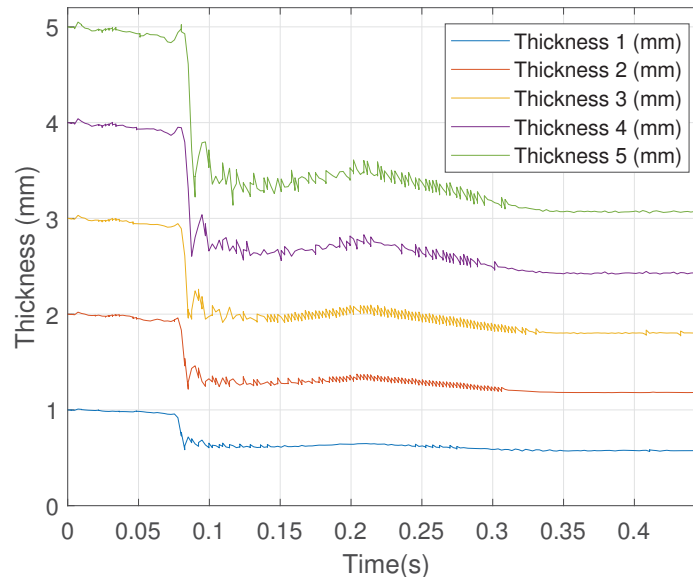
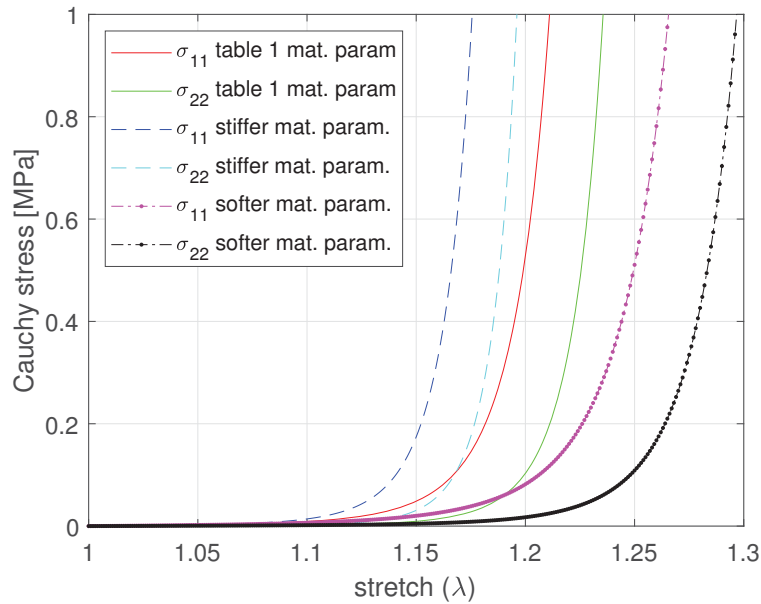


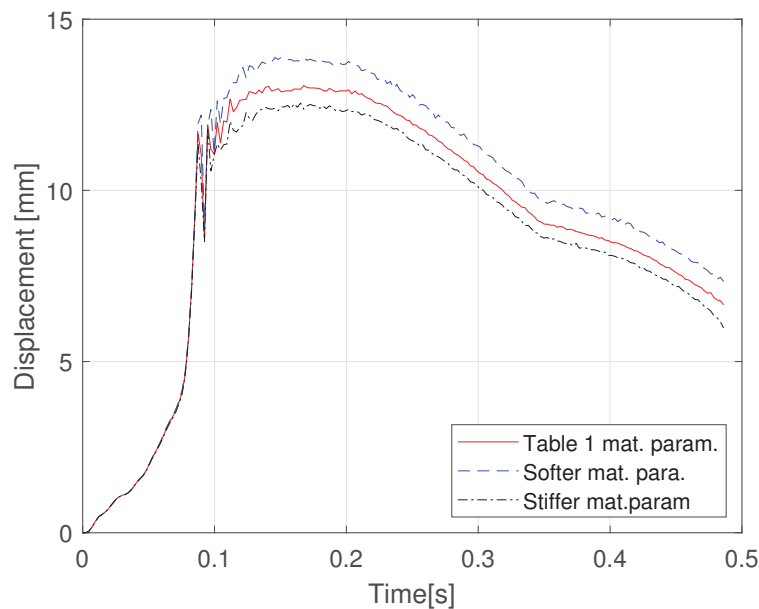
Figure 4.10: Reduction in section thickness for different leaflet thicknesses of point A.

4.7 Material Parameter Study

In this section the material parameters acquired from the nonlinear data-fitting is compared with stiffer and softer material parameters for the leaflets. This is done in order to observe if there is any difference in global response, when changing these parameters. In figure 4.11a, the stress-stretch curves are plotted for an equibiaxial tensile test. Furthermore, in figure 4.11b the magnitude of point A is plotted, comparing the response from table 3.1 with the stiffer and softer material parameters.



(a) Equibiaxial test



(b) Magnitude plot

Figure 4.11: Displacement of point A obtained from analyses using stiffer and softer material parameters compared with material parameters from nonlinear data-fitting.

From figure 4.11b, the response is as expected. For the stiffer material there are small oscillations during the analysis, and the displacement of point A at peak systole is 0.60mm less for the stiffer material, compared with the material parameters obtained in table 3.1. Moreover, the softer material clearly has higher oscillations throughout the analysis and displaces 0.75mm higher than the material parameters

from table 3.1 at peak systole. Lastly, it is observed that during the first part of the analysis the response is similar for every analysis. Even for the large difference in stiffness in figure 4.11a, the difference in leaflet displacement in figure 4.11b is moderate.

4.8 Mesh Study

The main goal of this study was to get an overall equal mesh size in the leaflets. As the smallest element in a dynamic explicit analysis governs the time step, it is of interest to have a uniform mesh size and not too small elements in order to keep the computational cost within reasonable limits.

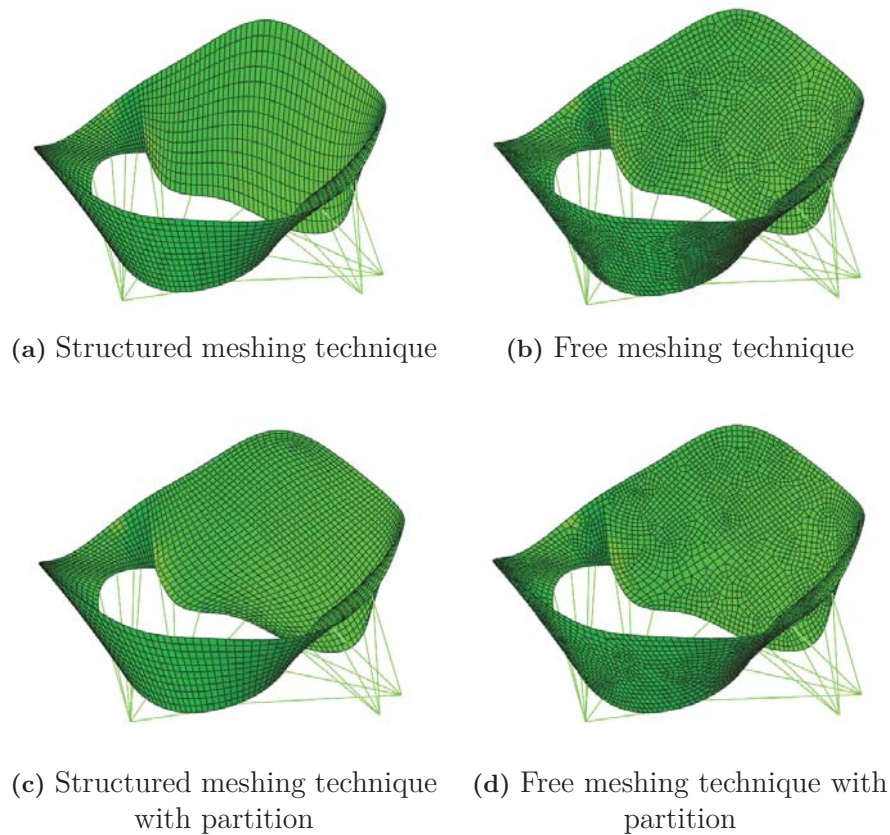
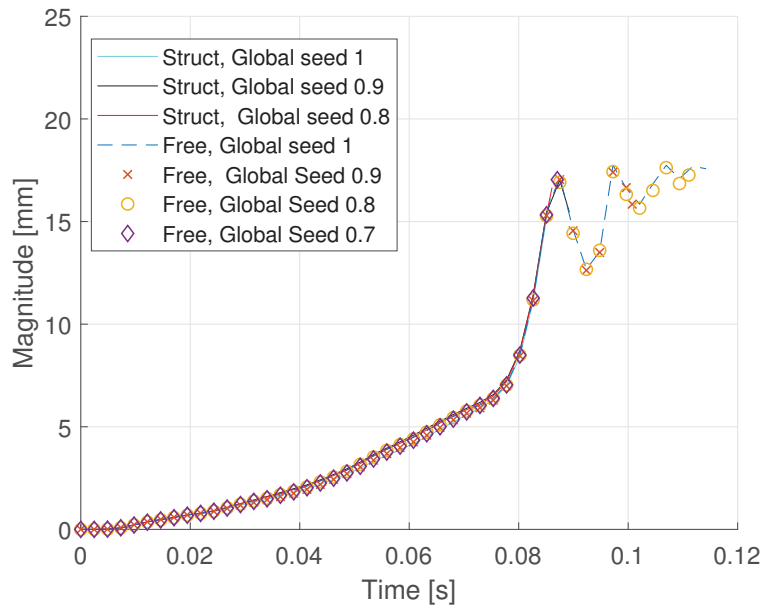


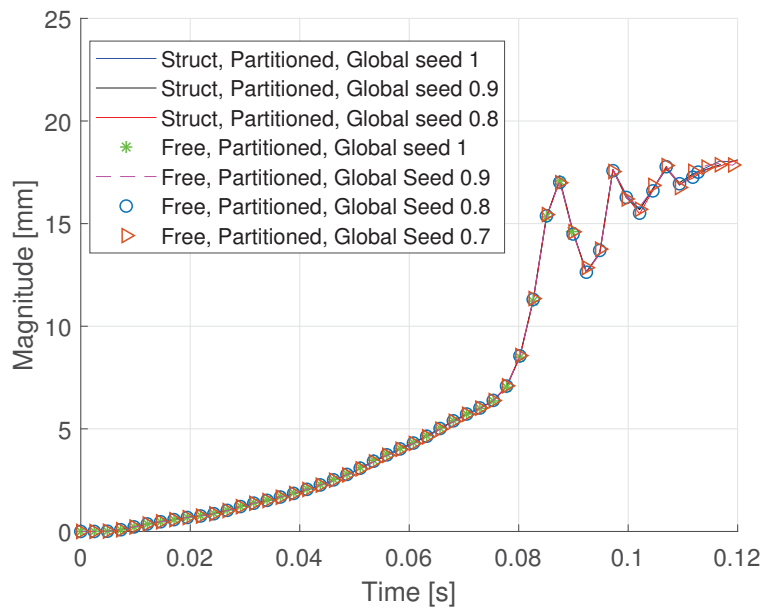
Figure 4.12: Different meshing techniques for the anterior leaflet

The different meshing techniques applied to the mitral valve leaflets are shown in figure 4.12, where a structured meshing technique is used for figure 4.12a and c, while a free meshing technique is used for figure 4.12b and d. For each technique the global seeding was iterated between 1 and 0.7, but deformation wave speed errors were an issue for low seeding, hence some analysis aborted. The global seeding was iterated in order to analyse if the global mesh size had any effect on accuracy.

In Figure 4.13, the magnitude or bulging of the anterior leaflet into the left atrium is plotted against time for each performed analysis.



(a) Anterior leaflet without partition



(b) Anterior leaflet with partition

Figure 4.13: Magnitude plot of different meshing techniques

4.9 Modified Annulus

In section 4.2, the global response show that there is late systolic regurgitation near the posteromedial commissure. In this section, an analysis is performed in order to

check if the regurgitation at this location is due to annular dilation. As can be seen in figure 4.1a, the annular area is at its highest where the late systolic regurgitation is observed. In order to model this, the VDISP user subroutine was modified so that the annulus and papillary muscle movement were held constant after peak systole ($t=0.20833s$). The results are presented in figure 4.14 below.

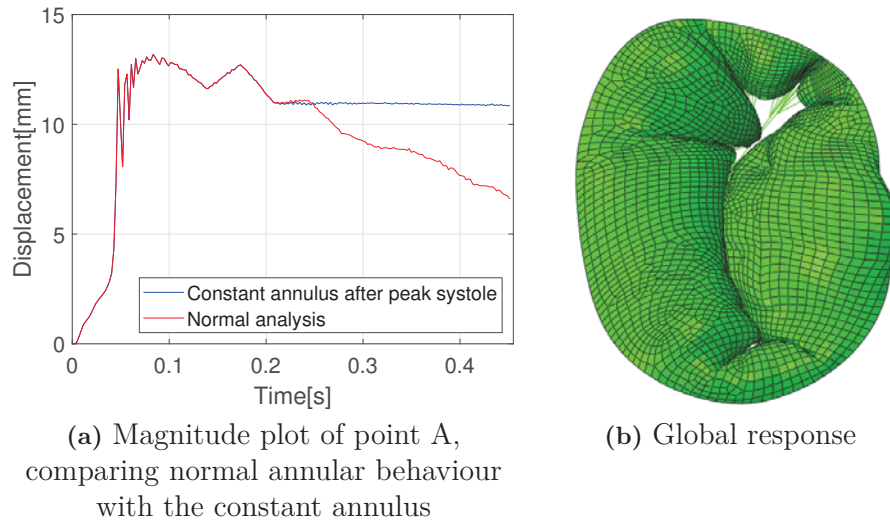


Figure 4.14: Closure of mitral valve after the annulus and papillary muscles are held constant

In figure 4.14a, it is observed that the displacement of point A is constant, as the PM movement and annular movement are held constant. As a result, the late systolic regurgitation observed near the posteromedial commissure at late systole is avoided.

5

Discussion

5.1 Global Response

The global response presented in section 4.2 shows that there is regurgitation at the posteromedial region (A3-P3) at late-systole. Moreover, the posteromedial side of the P2 segment is observed to prolapse at late-systole causing the posterior leaflet to override the anterior leaflet. These results are highly consistent with what we know about the patient's lesions, where regurgitation was detected in the posteromedial region at late systole.

In the anterolateral region (A1-P1), lack of closure in the FE model is observed throughout the whole analysis. The severity of regurgitation in this region is high before and after peak systole for the model. However, comparing the anterolateral regurgitation observed in the patient, the obtained results did not fully coincide with the patient. The patient experienced regurgitation due to prolapse of the P1 segment from mid systole, which is not entirely what the FE model predicts. The echocardiographic modelling might be the reason for the inaccurate observation of regurgitation at this region, and is further discussed in section 5.2.

As can be seen from figure 4.1a, the annular area starts to increase prior to peak systole ($t=0.17s$). The annulus continues to expand until the pressure has reached approximately 118mmHg (0.38s). Furthermore, the annular flattening observed during systole (figure 4.1b) is similar to what is written in literature about Barlow diseased mitral valves (Grewal et al., 2010, Apor et al., 2016). Comparing these findings with the global response (figure 4.2), it is evident that the annular changes must affect the coaptation of the leaflets. The late systolic regurgitation is observed when the annular area is at its highest. Thus, the dilation of the annulus may be a reason for regurgitation during this time interval.

In section 4.9, the movement of the annulus and the papillary muscles are held constant. As a result, the posteromedial region, which earlier experienced lack of closure at late systole, now coapts fully. It is clear from these results, that the annular dilation and papillary muscle movement is crucial for valve closure. It is further discovered that the leaflet displacement is dependent on the annular and papillary muscle dynamics. Where, at high pressures the pressure only makes the leaflets oscillate slightly around the displacement reached at peak systole (figure 4.14). Furthermore, these results explains the importance of an annuloplasty ring during surgical repair of Barlow patients. In section 4.9, the annular size was not reduced as during annuloplasty, but held constant at an already abnormally dilated annulus, leaving the hole at the anterolateral region open, while regurgitation at

the posteromedial region was prevented. Nevertheless, preventing the annulus from dilating further clearly shows advantages, which also exemplifies how crucial an annuloplasty ring is when performing surgery on a Barlow patient.

5.2 Echocardiographic Modelling

The patient-specific mitral valve geometry was modelled using echocardiographic data as described in section 3.2.1. The anterior leaflet and the P2 segment of the posterior leaflet were clearly visible on the echocardiographic images. However, locating the commissures was a more demanding process, where several echocardiographic views were needed. At the posteromedial commissure, the leaflets could be identified from the echocardiographic recording. Hence, the geometry obtained was satisfactory. For the anterolateral commissure the identification of the leaflet structure was cumbersome, leading to considerable uncertainty in the geometry at this region. As a consequence, the interpolated free edge at the anterolateral commissure was inaccurate.

As discussed in section 5.1 regurgitation is observed in the anterolateral region during systole. However, the patient did not experience similar severity of regurgitation near the anterolateral commissure. Thus, the observed regurgitation from the FE analysis is probably a consequence of the inaccurate modelling at the anterolateral region.

5.3 Comparison with 3D Echocardiographic Data

In figure 4.6, the correlation between the echocardiographic measurements and the mitral valve model response are observed to be very good. The bulging towards the left atrium is similar to that of the echocardiographic measurements. However, the FE response for both human and ovine chordae material parameters are shown to coapt further toward the left ventricle at peak systole compared to echocardiography. Furthermore, it is observed that both FE models bulge more than the echocardiographic measurements near the annulus, especially for the ovine material parameters.

Performing a similar comparison near the commissures at peak systole is difficult, as there is observed a lot of tissue on the echocardiographic images at this region. Collocating the echocardiographic measurements and the FE model at the commissures, show that the FE model bulges to little towards the atrium. The excessive tissue at this region is probably a combination of Barlow disease and calcifications near the annulus, making the comparison between the *in vivo* images and the FE model difficult in this region.

5.4 Material Parameters

In order to use the Holzapfel-Gasser-Ogden material model, introduced in section 2.8.1, to model the response of the mitral valve, it is required that the material pa-

parameters implemented in the model show a similar response compared to experimental data presented by May-Newman and Yin (1998). Obtaining a good fit between the experimental data and the material model provided by Abaqus, can make it possible to omit the usage of the subroutine VUMAT, where VUMAT is an Abaqus Explicit subroutine used to model different material models not directly available in Abaqus. The study performed in section 3.1.1, gave a sound fit comparing the experimental data from May-Newman and Yin (1998), with the Holzapfel-Gasser-Ogden strain-energy function.

Human mitral valve tissue has been shown to be stiffer than porcine mitral valve tissue (Prot et al., 2010). Hence, it can be argued that using porcine material properties might not give a correct response when modelling a human mitral valve. However, in the study (Barber et al., 2001b), myxomatous mitral valve leaflets were identified to be twice as extensible and less stiff compared to healthy human leaflets. As a consequence, porcine material parameters are assumed to be a better assumption than using the parameters from a healthy human, due to the difference in stiffness.

The chordae tendineae was modelled with both human and ovine material parameters. Comparing the global response, the coaptation and the location of regurgitation was observed to be near identical. From figure 4.5, the total displacement of point A and B are approximately $1mm$ higher for the ovine chordae parameters. Furthermore, the difference in displacement is mainly observed when the ventricular surface is subjected to peak pressures leading to high chordae strains. As a consequence the human chordae is observed to displace less at high strains compared to the ovine chordae due to the nature of the material. In the study by Barber et al. (2001b), myxomatous chordae tendineae were found to be 50 % less stiff compared to human chordae. Studying the comparison with 3D echocardiographic measurements, the ovine chordae parameters are observed to correlate less to the echocardiography than the model with human chordae parameters. Furthermore, there is observed little difference in coaptation between the models, but the ovine model prolapses more as both the leaflets displace towards the atrium.

In section 4.7, it was shown that the difference in displacements between the stiffer, softer and material parameters from table 3.1 were low. Hence, it appears that annulus and papillary muscle movements have more influence on the global response than the applied materials.

5.5 Boundary Conditions

The boundary conditions applied to the mitral valve model are found to be an essential part of the FE models global response. The annular and papillary muscle configurations are accounted for at every echocardiographic time step, giving them a continuous and close to reality motion. The difference in displacements observed with different material parameters in section 4.7, are moderate, hence the applied boundary conditions seem to govern the global response more than the material parameters used. Furthermore, as discovered in section 4.9, the severe annular dilation contributes significantly to regurgitation, exemplifying the importance of a correct modelled annular movement to predict regurgitation in Barlow patients.

5.6 Chordae Modelling

The marginal chordae tendineae are modelled so that they originate from the papillary muscles and insert into the free edge of the mitral valve leaflets, while the strut chordae insert into the anterior leaflet rough zone. The chordae insertion sites at the free edge are prone to high stresses, and the splitting of the chordae helps redistributing the loads along the elements, preventing the elements from excessive distortion. The chordae modelling is not just important for anatomical correctness but also for the finite element analysis as a whole.

From echocardiographic images it is not possible to get a full representation of the chordae insertion site, nor the amount of chordae. As a consequence, for a patient-specific analysis, the amount of chordae and insertion sites has to be assumed from literature (Kunzelman et al., 1994). Furthermore, it is not possible to detect if the chordae are stretched or not in diastole. A characteristic feature for Barlow patients is the elongated chordae at systole (Carpentier et al., 2010), which might leave the chordae slack at diastole. It is therefore assumed that there is no pre-tension in the chordae for a Barlow patient. Hence, the chordae are modelled as straight lines without any form of pre-tension. The model managed to follow the echocardiographic measurements without any pre-tensions, which was not the case in the study performed by Pham et al. (2017). However, in the study by Pham et al. (2017) the studied valve was a patient with functional mitral regurgitation (FMR), which is not a degenerative disease. It can be argued that some of the chordae should be modelled slack. However, this needs to be studied further.

5.7 Material Orientation

The material orientation applied in the FE model on the mitral valve leaflets is for a healthy porcine specimen. However, as stated in literature, the collagen fibres in Barlow leaflets are observed to be disoriented and disrupted (Hjortnaes et al., 2016). In Anyanwu and Adams (2007), this disruption is found to be due to myxomatous degeneration. Hence, the fibre direction used in this paper may not be entirely accurate. However, to the author's knowledge little is known about the collagen orientation for Barlow mitral leaflets. The gradual rotation of the collagen fibres towards the commissures in the anterior leaflet is not fully accounted for, where instead each partitioned region is given one specific direction as described in section 3.2.7. This modelling technique leads to some abrupt changes where the modelled orientation changes (figure 3.12). This leads to the stress concentrations observed on the anterior leaflet, just above the chordae insertions (figure 4.7).

5.8 Stresses

The von Mises stresses were found to be highest where the abrupt changes in material orientation were present. However, removing the elements with high stresses due to this feature, more reasonable stress values were observed. Regions of high stresses near the chordae insertion points, especially where the strut chordae is inserted,

and the fibrous trigones are observed. This is consistent with previous studies (Prot et al., 2009, Votta et al., 2008). However, comparing stress values with literature, is not so beneficial, as an unusual thickness of $3mm$ is used in this study.

5.9 Mesh Study

From the meshing techniques analyses, it was first of all evident that having no partition in the leaflets reduced the stability of the analyses. No partition leads to a higher occurrence of excessively distorted elements early in the analysis, leading to an aborted analysis. Furthermore, the accuracy of the analyses was shown to be independent of global seeding and meshing technique, as the magnitude of each analysis followed the same path ref. figure 4.13. It was further observed that when the global seeding was reduced to 0.7, deformation wave speed warnings made the analyses unstable. The stable time increment in an explicit analysis is proportional to the length of the smallest element, and inversely proportional to the dilation wave speed through the element. Hence, a too small element size will lead to deformation wave speed warnings.

For the partitioned leaflets, the meshing technique is observed to affect the CPU-time of the analysis. There is a distinct difference in CPU-time and number of increments, where the free technique is almost three times faster than the structured technique. The reason for this observation is probably due to the fact that the free technique has the ability to evenly distribute its elements, resulting in overall equal mesh size. While the structured technique does not have this ability, resulting in some regions with small elements.

Due to the implementation of varying fibre directions, the leaflets had to be partitioned in a specific manner. The partitioning has made it necessary to implement the free meshing technique in order to reduce the analysis time. As discovered in this study, global seeding does not affect the accuracy of the analyses. Hence a seeding giving reasonable CPU-times should be used.

5.10 Thickness Study

The thickness study performed in section 4.6, shows that as the leaflet thickness is increased, the leaflet stresses reduce. However, the reduction in leaflet stress is observed to be higher between thicknesses of $1mm$ and $2mm$, compared with the stress reduction between $4mm$ and $5mm$ thick leaflets. The difference in stress reduction may be because the thicker leaflet elements stretch less at peak systole, while the percentage reduction in thickness is approximately the same for every modelled thickness (table 4.2). Leading the thicker modelled leaflets to have lower overall stresses.

6

Concluding Remarks

6.1 Conclusion

In this thesis, a finite element model of a mitral valve with Barlow disease has been studied. Hyperelastic material models have been used on the mitral valve leaflets and chordae tendineae, and the finite element model has been modelled with annular and papillary muscle motions. Lack of closure were observed in both the anterolateral and posteromedial commissure for the model, which agrees, to some extent with the echocardiographic findings of the patient. The finite element model predicted regurgitation in the posteromedial region well, where late systolic regurgitation and prolapse were observed for both the patient and model. In the anterolateral region the model predicted regurgitation throughout systole, while echocardiography only showed regurgitation at mid-systole. An explanation for this discrepancy may be that the commissure geometry is difficult to define from echocardiography, especially for the anterolateral commissure. Refinement of the method used to localize these regions *in vivo* are necessary to create accurate models. In order to refine the geometrical modelling, an autostereoscopic 3D screen could be used to locate intricate points near the commissures (Dumont et al., 2019). Lastly, severe annular dilation seems to be one major cause of mitral regurgitation. In this study, the most severe lack of closure from mid- to late-systole appeared when the annulus dilated the most. Hence, the boundary conditions were modified in order to check how a constant annulus at peak systole would alter the coaptation of the leaflets, resulting in no regurgitation in the posteromedial region.

Creating accurate patient-specific models which can predict regurgitation correctly and reliably will in the future open up several exciting possibilities: for example, performing surgery *in silico* in order to optimize and create a patient-specific surgical procedure. Furthermore, it may facilitate the development of repair devices as they can be tested and refined numerically.

6.2 Further Work

There are several ways the presented patient-specific finite element model can be improved, in this section suggestions for further studies are discussed.

As briefly discussed in section 6.1, the usage of an Autostereoscopic 3D screen to extract intricate points from the commissural regions, would increase the accuracy of the FE geometry at the commissures. Combining the echocardiographic modelling technique presented in this thesis, with Autostereoscopic modelling, is

worth exploring further. This method may facilitate the creation of a geometry with increased accuracy, capable of predicting regurgitation, especially at the anterolateral commissure.

The material properties and material orientations used in the present work are obtained from human, porcine and ovine specimens. However, as discussed earlier, myxomatous degeneration of the leaflets and chordae tendineae decreases the overall stiffness and disrupts the collagen orientation. Hence, proper material parameters for Barlow mitral valve leaflets and chordae tendineae should be obtained. Furthermore, the mean collagen fibre direction in Barlow mitral valve leaflets should also be studied further.

In the present work, the annulus has shown to be an essential anatomical feature when it comes to regurgitation. Further studies should be performed on the annulus of Barlow patients, and how a reduction in annular size would affect the closure of the mitral valve *in silico*. Here it is important to bear in mind that as the annulus is modified, the annular movement becomes unpredictable. Hence, how to model a good enough prediction of the annular movement after size reduction must also be addressed. If this is accomplished, annuloplasty on FE models should be feasible.

The finite element geometry presented in this thesis is not modelled with blood, but with pressure applied to the ventricular surface of the anterior and posterior leaflets. As a consequence, we do not know how the blood interacts and impacts valve closure of the Barlow mitral valve. Further work should be performed, where a fluid structure interaction (FSI) model is created.

The displacement boundary conditions and loading employed in this thesis are only applied to simulate the mitral valve from the end-diastole to the end-systole. Hence, further studies should be done on modelling of a mitral valve undergoing a full cardiac cycle.

Lastly, this was a pilot study on creating a finite element model of a Barlow mitral valve. However, only one diseased mitral valve was studied. Hence, it is evident that the procedure presented in this thesis should be performed on several Barlow mitral valves to check how consistently the presented method predicts regurgitation.

Bibliography

- Abaqus (2014), *Abaqus Analysis User's Guide*, Dassault Systemes.
- Adams, D. H., Anyanwu, A. C., Rahmanian, P. B., Abascal, V., Salzberg, S. P. and Filsoufi, F. (2006), 'Large annuloplasty rings facilitate mitral valve repair in barlow's disease', *Ann Thorac Surg* **82**(6), 2096–100; discussion 2101.
- Anyanwu, A. C. and Adams, D. H. (2007), 'Etiologic classification of degenerative mitral valve disease: Barlow's disease and fibroelastic deficiency', *Semin Thorac Cardiovasc Surg* **19**(2), 90–6.
- Apor, A., Nagy, A. I., Kovacs, A., Manouras, A., Andrassy, P. and Merkely, B. (2016), 'Three-dimensional dynamic morphology of the mitral valve in different forms of mitral valve prolapse - potential implications for annuloplasty ring selection', *Cardiovasc Ultrasound* **14**(1), 32.
- Barber, J. E., Kasper, F. K., Ratliff, N. B., Cosgrove, D. M., Griffin, B. P. and Vesely, I. (2001a), 'Mechanical properties of myxomatous mitral valves', *J Thorac Cardiovasc Surg* **122**(5), 955–62.
- Barber, J. E., Ratliff, N. B., Cosgrove, D. M., r., Griffin, B. P. and Vesely, I. (2001b), 'Myxomatous mitral valve chordae. i: Mechanical properties', *J Heart Valve Dis* **10**(3), 320–4.
- Ben Zekry, S., Spiegelstein, D., Sternik, L., Lev, I., Kogan, A., Kuperstein, R. and Raanani, E. (2015), 'Simple repair approach for mitral regurgitation in barlow disease', *J Thorac Cardiovasc Surg* **150**(5), 1071–7 e1.
- Borger, M. A. and Mohr, F. W. (2010), 'Repair of bileaflet prolapse in barlow syndrome', *Semin Thorac Cardiovasc Surg* **22**(2), 174–8.
- Brock, R. C. (1952), 'The surgical and pathological anatomy of the mitral valve', *British heart journal* **14**(4), 489–513.
- Carpentier, A., Adams, D. H. and Filsoufi, F. (2010), *Carpentier's reconstructive valve surgery : from valve analysis to valve reconstruction*, Philadelphia: Saunders Elsevier: 33,.
- Carpentier, A. F., Lessana, A., Relland, J. Y. M., Belli, E., Mihaileanu, S., Berrebi, A. J., Palsky, E. and Loulmet, D. F. (1995), 'The "physio-ring": an advanced concept in mitral valve annuloplasty', *The Annals of Thoracic Surgery* **60**(5), 1177–1186.

- Carpentier, A. F., Pellerin, M., Fuzellier, J. F. and Relland, J. Y. (1996), ‘Extensive calcification of the mitral valve annulus: pathology and surgical management’, *J Thorac Cardiovasc Surg* **111**(4), 718–29; discussion 729–30.
- Chandra, S., Salgo, I. S., Sugeng, L., Weinert, L., Tsang, W., Takeuchi, M., Spencer, K. T., O’Connor, A., Cardinale, M., Settlemier, S., Mor-Avi, V. and Lang, R. M. (2011), ‘Characterization of degenerative mitral valve disease using morphologic analysis of real-time three-dimensional echocardiographic images: objective insight into complexity and planning of mitral valve repair’, *Circ Cardiovasc Imaging* **4**(1), 24–32.
- Cochran, R. P., Kunzelman, K. S., Chuong, C. J., Sacks, M. S. and Eberhart, R. C. (1991), ‘Nondestructive analysis of mitral valve collagen fiber orientation’, *ASAIO Trans* **37**(3), 447–8.
- Dal-Bianco, J. P. and Levine, R. A. (2013), ‘Anatomy of the mitral valve apparatus: role of 2d and 3d echocardiography’, *Cardiol Clin* **31**(2), 151–64.
- Dumont, K. A., Kvitting, J. P., Karlsen, J. S., Remme, E. W., Hausken, J., Lundblad, R., Fiane, A. E. and Urheim, S. (2019), ‘Validation of a holographic display for quantification of mitral annular dynamics by three-dimensional echocardiography’, *J Am Soc Echocardiogr* **32**(2), 303–316 e4.
- D’Addario, G., Torracca, L., Oppizzi, M., Alfieri, O., Stefano, P., Maisano, F., La Canna, G. and Zogno, M. (1998), ‘The edge-to-edge technique: a simplified method to correct mitral insufficiency¹’, *European Journal of Cardio-Thoracic Surgery* **13**(3), 240–246.
- Einstein, D. R., Kunzelman, K. S., Reinhall, P. G., Nicosia, M. A. and Cochran, R. P. (2005), ‘The relationship of normal and abnormal microstructural proliferation to the mitral valve closure sound’, *Journal of Biomechanical Engineering* **127**(1), 134–147.
- Estes, E. H., Dalton, F. M., Entman, M. L., Dixon, H. B. and Hackel, D. B. (1966), ‘The anatomy and blood supply of the papillary muscles of the left ventricle’, *American Heart Journal* **71**(3), 356–362.
- Feldman, T., Wasserman, H. S., Herrmann, H. C., Gray, W., Block, P. C., Whitlow, P., St Goar, F., Rodriguez, L., Silvestry, F., Schwartz, A., Sanborn, T. A., Condado, J. A. and Foster, E. (2005), ‘Percutaneous mitral valve repair using the edge-to-edge technique: six-month results of the everest phase i clinical trial’, *J Am Coll Cardiol* **46**(11), 2134–40.
- Fornes, P., Heudes, D., Fuzellier, J. F., Tixier, D., Bruneval, P. and Carpentier, A. (1999), ‘Correlation between clinical and histologic patterns of degenerative mitral valve insufficiency: a histomorphometric study of 130 excised segments’, *Cardiovasc Pathol* **8**(2), 81–92.
- Fucci, C., Faggiano, P., Nardi, M., D’Aloia, A., Coletti, G., De Cicco, G., Latini, L., Vizzardi, E. and Lorusso, R. (2013), ‘Triple-orifice valve repair in severe barlow

- disease with multiple-jet mitral regurgitation: report of mid-term experience', *Int J Cardiol* **167**(6), 2623–9.
- Grewal, J., Suri, R., Mankad, S., Tanaka, A., Mahoney, D. W., Schaff, H. V., Miller, F. A. and Enriquez-Sarano, M. (2010), 'Mitral annular dynamics in myxomatous valve disease: new insights with real-time 3-dimensional echocardiography', *Circulation* **121**(12), 1423–31.
- Gross, L. and Kugel, M. A. (1931), 'Topographic anatomy and histology of the valves in the human heart', *The American journal of pathology* **7**(5), 445–474.7.
- Hjortnaes, J., Keegan, J., Bruneval, P., Schwartz, E., Schoen, F. J., Carpentier, A., Levine, R. A., Hagege, A. and Aikawa, E. (2016), 'Comparative histopathological analysis of mitral valves in barlow disease and fibroelastic deficiency', *Semin Thorac Cardiovasc Surg* **28**(4), 757–767.
- Ho, S. Y. (2002), 'Anatomy of the mitral valve', *Heart* **88**(suppl 4), iv5–iv10.
- Holzapfel, G. A., Ogden, R. W. and Gasser, T. C. (2000), 'A new constitutive framework for arterial wall mechanics and a comparative study of material models', *Journal of Elasticity* **61**(1-3), 1–48.
- Holzapfel, G. A., Ogden, R. W. and Gasser, T. C. (2006), 'Hyperelastic modelling of arterial layers with distributed collagen fibre orientations', *J. R. Soc. Interface* **3**(6), 15–35.
- Iaizzo, P. (2005), (Ed.) *Handbook of Cardiac Anatomy, Physiology, and Devices*, Humana Press: 18-22.
- Iung, B., Baron, G., Tornos, P., Gohlke-Barwolf, C., Butchart, E. G. and Vahanian, A. (2007), 'Valvular heart disease in the community: a european experience', *Curr Probl Cardiol* **32**(11), 609–61.
- Jouan, J., Berrebi, A., Chauvaud, S., Menasche, P., Carpentier, A. and Fabiani, J. N. (2012), 'Mitral valve reconstruction in barlow disease: long-term echographic results and implications for surgical management', *J Thorac Cardiovasc Surg* **143**(4 Suppl), S17–20.
- Katz, W. E., Conrad Smith, A. J., Crock, F. W. and Cavalcante, J. L. (2017), 'Echocardiographic evaluation and guidance for mitraclip procedure', *Cardiovasc Diagn Ther* **7**(6), 616–632.
- Kuntze, T., Borger, M. A., Falk, V., Seeburger, J., Girdauskas, E., Doll, N., Walther, T. and Mohr, F. W. (2008), 'Early and mid-term results of mitral valve repair using premeasured gore-tex loops ('loop technique')', *Eur J Cardiothorac Surg* **33**(4), 566–72.
- Kunzelman, K. S., Cochran, R. P., Verrier, E. D. and Eberhart, R. C. (1994), 'Anatomic basis for mitral valve modelling', *J Heart Valve Dis* **3**(5), 491–6.
- Lam, J. H., Ranganathan, N., Wigle, E. D. and Silver, M. D. (1970), 'Morphology of the human mitral valve. i. chordae tendineae: a new classification', *Circulation* **41**(3), 449–58.

- Laulusa, A., Bauchau, O. A., Choi, J. Y., Tan, V. B. C. and Li, L. (2006), 'Evaluation of some shear deformable shell elements', *International Journal of Solids and Structures* **43**(17), 5033–5054.
- Lawrie, G. M., Earle, E. A. and Earle, N. (2011), 'Intermediate-term results of a nonresectional dynamic repair technique in 662 patients with mitral valve prolapse and mitral regurgitation', *J Thorac Cardiovasc Surg* **141**(2), 368–76.
- Lawrie, G. M., Zoghbi, W., Little, S., Shah, D., Ben-Zekry, Z., Earle, N. and Earle, E. (2016), 'One hundred percent reparability of degenerative mitral regurgitation: Intermediate-term results of a dynamic engineered approach', *Ann Thorac Surg* **101**(2), 576–83; discussion 583–4.
- Levick, J. (2010), *An Introduction to Cardiovascular Physiology*, London: Hodder Arnold: 18-22.
- Liao, J. and Vesely, I. (2003), 'A structural basis for the size-related mechanical properties of mitral valve chordae tendineae', *Journal of Biomechanics* **36**(8), 1125–1133.
- Lim, K. O. and Boughner, D. R. (1975), 'Mechanical properties of human mitral valve chordae tendineae: variation with size and strain rate', *Can J Physiol Pharmacol* **53**(3), 330–9.
- Maisano, F., Schreuder, J. J., Oppizzi, M., Fiorani, B., Fino, C. and Alfieri, O. (2000), 'The double-orifice technique as a standardized approach to treat mitral regurgitation due to severe myxomatous disease: surgical technique', *European Journal of Cardio-Thoracic Surgery* **17**(3), 201–205.
- May-Newman, K. and Yin, F. C. (1998), 'A constitutive law for mitral valve tissue', *J Biomech Eng* **120**(1), 38–47.
- McCarthy, K. P., Ring, L. and Rana, B. S. (2010), 'Anatomy of the mitral valve: understanding the mitral valve complex in mitral regurgitation', *Eur J Echocardiogr* **11**(10), i3–9.
- Millington-Sanders, C., Meir, A., Lawrence, L. and Stolinski, C. (1998), 'Structure of chordae tendineae in the left ventricle of the human heart', *J Anat* **192** (Pt 4), 573–81.
- Muresian, H. (2009), 'The clinical anatomy of the mitral valve', *Clin Anat* **22**(1), 85–98.
- Ormiston, J. A., Shah, P. M., Tei, C. and Wong, M. (1981), 'Size and motion of the mitral valve annulus in man. i. a two-dimensional echocardiographic method and findings in normal subjects', *Circulation* **64**(1), 113–20.
- Padala, M., Sacks, M. S., Liou, S. W., Balachandran, K., He, Z. and Yoganathan, A. P. (2010), 'Mechanics of the mitral valve strut chordae insertion region', *J Biomech Eng* **132**(8), 081004.
- Pham, T., Kong, F., Martin, C., Wang, Q., Primiano, C., McKay, R., Elefteriades,

- J. and Sun, W. (2017), ‘Finite element analysis of patient-specific mitral valve with mitral regurgitation’, *Cardiovasc Eng Technol* **8**(1), 3–16.
- Prot, V., Haaverstad, R. and Skallerud, B. (2009), ‘Finite element analysis of the mitral apparatus: annulus shape effect and chordal force distribution’, *Biomech Model Mechanobiol* **8**(1), 43–55.
- Prot, V. and Skallerud, B. (2017), ‘Contributions of prestrains, hyperelasticity, and muscle fiber activation on mitral valve systolic performance’, *Int J Numer Method Biomed Eng* **33**(4).
- Prot, V., Skallerud, B. and Holzapfel, G. A. (2007), ‘Transversely isotropic membrane shells with application to mitral valve mechanics. constitutive modelling and finite element implementation’, *Int. J. Numer. Meth. Engng.* **71**(8), 987–1008.
- Prot, V. and Skallerud, B. J. C. M. (2009), ‘Nonlinear solid finite element analysis of mitral valves with heterogeneous leaflet layers’, *Comput. Mech.* **43**(3), 353–368.
- Prot, V., Skallerud, B., Sommer, G. and Holzapfel, G. A. (2010), ‘On modelling and analysis of healthy and pathological human mitral valves: two case studies’, *J Mech Behav Biomed Mater* **3**(2), 167–77.
- Quill, J. L., Hill, A. J., Laske, T. G., Alfieri, O. and Iaizzo, P. A. (2009), ‘Mitral leaflet anatomy revisited’, *J Thorac Cardiovasc Surg* **137**(5), 1077–81.
- Ranganathan, N., Lam, J. H., Wigle, E. D. and Silver, M. D. (1970), ‘Morphology of the human mitral valve. ii. the valve leaflets’, *Circulation* **41**(3), 459–67.
- Roberts, N., Morticelli, L., Jin, Z., Ingham, E. and Korossis, S. (2016), ‘Regional biomechanical and histological characterization of the mitral valve apparatus: Implications for mitral repair strategies’, *J Biomech* **49**(12), 2491–501.
- Schubert, S. A., Mehaffey, J. H., Charles, E. J. and Kron, I. L. (2017), ‘Mitral valve repair: The french correction versus the american correction’, *Surg Clin North Am* **97**(4), 867–888.
- Staessen, J. A., Li, Y., Hara, A., Asayama, K., Dolan, E. and O’Brien, E. (2017), ‘Blood pressure measurement anno 2016’, *American Journal of Hypertension* **30**(5), 453–463.
- Tomsic, A., Hiemstra, Y. L., Bissessar, D. D., van Brakel, T. J., Versteegh, M. I. M., Ajmone Marsan, N., Klautz, R. J. M. and Palmén, M. (2018), ‘Mitral valve repair in barlow’s disease with bileaflet prolapse: the effect of annular stabilization on functional mitral valve leaflet prolapse’, *Interact Cardiovasc Thorac Surg* **26**(4), 559–565.
- Van Mieghem, N. M., Piazza, N., Anderson, R. H., Tzikas, A., Nieman, K., De Laet, L. E., McGhie, J. S., Geleijnse, M. L., Feldman, T., Serruys, P. W. and de Jaegere, P. P. (2010), ‘Anatomy of the mitral valvular complex and its implications for transcatheter interventions for mitral regurgitation’, *J Am Coll Cardiol* **56**(8), 617–26.
- von Oppell, U. O. and Mohr, F. W. (2000), ‘Chordal replacement for both minimally

- invasive and conventional mitral valve surgery using premeasured gore-tex loops', *Ann Thorac Surg* **70**(6), 2166–8.
- Votta, E., Caiani, E., Veronesi, F., Soncini, M., Montevocchi, F. M. and Redaelli, A. (2008), 'Mitral valve finite-element modelling from ultrasound data: a pilot study for a new approach to understand mitral function and clinical scenarios', *Philos Trans A Math Phys Eng Sci* **366**(1879), 3411–34.
- Zhang, W., Ayoub, S., Liao, J. and Sacks, M. S. (2016), 'A meso-scale layer-specific structural constitutive model of the mitral heart valve leaflets', *Acta Biomater* **32**, 238–255.
- Zuo, K., Pham, T., Li, K., Martin, C., He, Z. and Sun, W. (2016), 'Characterization of biomechanical properties of aged human and ovine mitral valve chordae tendineae', *J Mech Behav Biomed Mater* **62**, 607–618.

Appendices

A

Manuscript submitted for 10th
National Conference on
Computational Mechanics

FINITE ELEMENT ANALYSIS OF A BARLOW MITRAL VALVE: PATIENT SPECIFIC GEOMETRY AND COMPARISON WITH THREE-DIMENSIONAL ECHOCARDIOGRAPHIC DATA.

Hans Martin Dahl Aguilera¹, Victorien Prot¹, Bjørn Skallerud¹ and Stig Urheim²

¹Department of Structural Engineering, Faculty of Engineering Science
The Norwegian University of Science and Technology, Norway
e-mail: victorien.prot@ntnu.no

² Department of Heart Disease
Haukeland University Hospital, Norway

Key words: Computational Methods, Finite element method, Barlow disease, Degenerative mitral valve disease.

Abstract. In this paper, a patient-specific finite element (FE) model is created for a mitral valve diagnosed with Barlow disease. The FE model is constructed from three-dimensional (3D) echocardiographic data. The mitral valve leaflets and the chordae tendineae are modelled with hyperelastic materials. Patient-specific annular and papillary muscle motions are used as boundary conditions in the analyses. The FE model of this Barlow mitral valve is used to predict the location of mitral regurgitation. The global response of the mitral valve model is compared with echocardiographic measurements, and with the patients lesions observed pre- and intraoperatively. The results showed regurgitation at both commissures, and the FE model aligned well with the echocardiographic measurements at peak systole.

1 Introduction

The mitral valve is a complex structure that separates the left atrium from the left ventricle, ensuring one-way blood flow between the two heart chambers. This valvular structure consists of several components: the anterior and posterior leaflets, the annulus, chordae tendineae and the papillary muscles. The annulus is situated at the intersection between the left atrium and the left ventricle, and functions as an attachment ring for the two leaflets. Moreover, from the ventricular wall, the papillary muscles originate. From the papillary muscles, the chordae tendineae branches out and insert into the posterior

and anterior leaflets. During the cardiac cycle, the components of the mitral valve work in concert in order to achieve proper closure at systole, enabling unidirectional blood flow. Furthermore, Carpentier et al.[1] divided the posterior and anterior leaflets into six different segments described in figure 1.

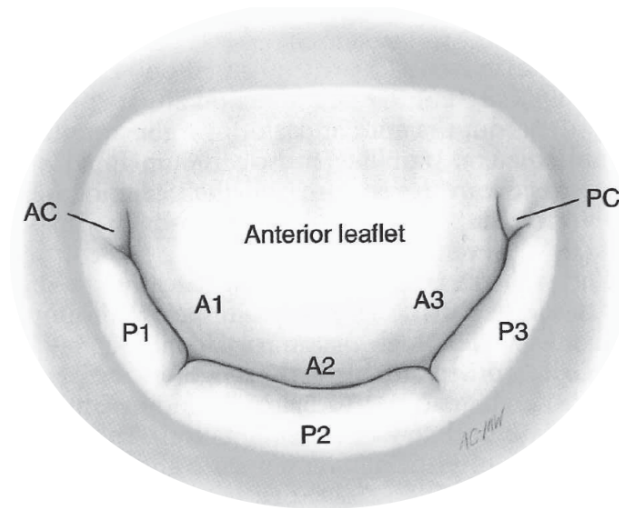


Figure 1: Atrial view of the mitral valve with leaflet segmentation. Anterolateral Commissure (AC), posteromedial Commissure (PC). Taken from [1]

The second most common valvular heart disease in European countries is mitral regurgitation [2]. Mitral regurgitation is predominantly caused by degenerative diseases such as Fibroelastic Deficiency or Barlow disease (BD), where the latter is the topic of this paper. BD affects the entire mitral valve apparatus, where a severely dilated annulus, excessive leaflet tissue, billowing or prolapse of the leaflets, myxomatous degeneration and chordae alterations are characteristic lesions. Another characteristic feature related to BD is that the annular saddle shape flattens, and overstretches at end systole[3]. Furthermore, Barlow disease is mainly observed in patients younger than the age of 60 [4]. The work by Hjortnaes et al.[5] studied the histological changes in the mitral valve due to Barlow's disease. It was observed that the thickening of the mitral valve leaflets was caused by gathering of water absorbent proteins (proteoglycans) in the spongiosa layer, and intimal thickening of the fibrosa and atrialis.

Repairing a Barlow mitral valve is a complex procedure, and often the whole mitral apparatus must be assessed. Reconstructive surgery of the mitral valve may include annuloplasty, different sliding and resection techniques and artificial chordal insertions. Sophisticated imaging techniques have in recent years become available, leading to a greater understanding of the mitral valve dynamics. The motivation for this paper is to develop a patient-specific finite element model of a Barlow mitral valve before surgical

treatment. The development of such a model will hopefully enable us to predict the location of mitral regurgitation. Furthermore, with a realistic model it should be possible to perform surgical procedures *in silico*, optimizing and creating a patient-specific repair procedure. To the author’s knowledge, this is the first time a Barlow mitral valve has been studied using a finite element model.

This paper is organized as follows. First, the patient’s pathology is presented. Then the material models, the FE geometry and boundary conditions are described. Thereafter, the results are presented and discussed. Finally, conclusions from the study are given.

2 Methods

2.1 Patient and echocardiographic measurement

In this section the studied patient, his lesions and the surgical procedures performed are briefly described.

The patient is a 45 year old male who was diagnosed with Barlow disease and operated in 2017 with mitral valve repair. The patient had a severely dilated annulus with excessive leaflet tissue and mitral regurgitation. From echocardiographic findings, multiple jets of mitral regurgitation in mid to late systole were observed. The most severe regurgitation was located in the posteromedial region with billowing (A2-A3-P3) and prolapse of the P3 segment. A less severe regurgitation jet was observed in the anterolateral region due to prolapse of P1. Mitral annular disjunction (MAD) of 10 mm was observed in the P1-P2 region.

The patient received an annuloplasty ring of size 38, triangular resection and sliding of P2 in order to reduce the height of the P2 segment. Furthermore, there was inserted 2x4 neo chordae (Goretex 5-0) from each papillary muscle and to the edge of the A2 and P2 segment. Lastly, there was performed a transposition of secondary P2 chordae to the free edge of the P2 segment.

2.2 Continuum mechanical framework and constitutive models

Kinematics

We consider a deformable body in two different instantaneous configurations Ω_0 and Ω , representing the reference and current configuration, respectively. A particle in the reference configuration Ω_0 is defined by the position vector \mathbf{X} . The position of the same particle in the current configuration Ω is further defined by the the vector \mathbf{x} . The relationship between the two configurations is described by the deformation map relationship $\mathbf{x} = \mathbf{x}(\mathbf{X}, t)$. The deformation gradient \mathbf{F} is defined as

$$\mathbf{F} = \frac{\partial \mathbf{x}}{\partial \mathbf{X}} \quad (1)$$

The volume ratio is defined as $J = \det \mathbf{F}$, where $J = 1$ describes an isochoric transformation. Furthermore, the right and left Cauchy-Green tensors are defined as $\mathbf{C} = \mathbf{F}^T \mathbf{F}$ and

$\mathbf{b} = \mathbf{F}\mathbf{F}^T$ respectively. Furthermore, the distortional part of the right and left Cauchy-Green can be written as $\bar{\mathbf{C}} = J^{-\frac{2}{3}}\mathbf{F}^T\mathbf{F}$ and $\bar{\mathbf{b}} = J^{-\frac{2}{3}}\mathbf{F}\mathbf{F}^T$

For an anisotropic material reinforced by a family of fibres, the fibre direction in the reference configuration is defined by the unit vector \mathbf{a}_0 . The mapping of the fibre direction from the reference configuration to the current configuration is expressed as $\mathbf{a} = \mathbf{F}\mathbf{a}_0$.

Strain-energy function and stress tensors

For hyperelastic materials a strain-energy function Ψ is introduced in order to describe the response of the material. The strain-energy function Ψ for incompressible materials can be expressed in terms of five invariants, I_1, I_2, J, I_4, I_5 as,

$$\Psi = \tilde{\Psi}(I_1, I_2, I_4, I_5) + p(1 - J), \quad (2)$$

where the principal invariants of \mathbf{C} , I_1, I_2, J are related to isotropic elasticity and defined as,

$$I_1 = tr(\mathbf{C}), \quad I_2 = \frac{1}{2}[I_1^2 - tr(\mathbf{C}^2)], \quad J = \sqrt{det(\mathbf{C})}. \quad (3)$$

For an incompressible material the third invariant can be written as $J = 1$. The invariants I_4, I_5 describes the transversely isotropic properties of the material, expressed by the fibre direction in the reference configuration \mathbf{a}_0 and the right Cauchy-Green tensor \mathbf{C} ,

$$I_4 = \mathbf{a}_0 \cdot \mathbf{C}\mathbf{a}_0, \quad I_5 = \mathbf{a}_0 \cdot \mathbf{C}^2\mathbf{a}_0, \quad (4)$$

and p is the Lagrange multiplier. The second Piola-Kirchhoff stress tensor \mathbf{S} can be derived from 2 giving,

$$\mathbf{S} = 2 \sum_{\substack{i=1 \\ i \neq 3}}^5 \frac{\partial \Psi}{\partial \mathbf{I}_i} \frac{\partial \mathbf{I}_i}{\partial \mathbf{C}} + p\mathbf{C}^{-1} \quad (5)$$

where the scalar p can be determined from the plane stress condition. In this work, we apply this constitutive model to mitral leaflets that may be considered as thin sheets, thus assuming that the stress in the out of plane direction (denoted 3-direction) S_{33} is zero leads to:

$$p = -2 \sum_{\substack{i=1 \\ i \neq 3}}^5 \frac{\partial \Psi}{\partial \mathbf{I}_i} \frac{\partial \mathbf{I}_i}{\partial \mathbf{C}_{33}} C_{33} \quad (6)$$

Lastly the second Piola-Kirchhoff stress tensor \mathbf{S} can be transformed to the Cauchy stress tensor $\boldsymbol{\sigma} = \frac{1}{J}\mathbf{F}\mathbf{S}\mathbf{F}^T$ by the push-forward operation of \mathbf{S} [6]. This was used for material parameter fitting presented in section 2.3.

2.3 Material models and parameters

The constitutive model used to analyse the response of the leaflets, is a hyperelastic anisotropic material model, which is available through the material library in Abaqus. The material model was originally developed in order to model the mechanical response of arterial layers with a distributed collagen fibre orientation [7]. The strain-energy function W is defined in terms of the deviatoric strain invariants \bar{I}_1 and \bar{I}_4 . Which are defined as,

$$\bar{I}_1 = tr\bar{\mathbf{C}}, \quad \bar{I}_4 = \mathbf{a}_0 \cdot \bar{\mathbf{C}} \cdot \mathbf{a}_0, \quad (7)$$

Thus,

$$W(\bar{I}_1, \bar{I}_4) = C_{10}(\bar{I}_1 - 3) + \frac{1}{D} \left(\frac{(J^2) - 1}{2} - \ln(J) \right) + \frac{k_1}{2k_2} (exp^{k_2(\bar{E})^2} - 1) \quad (8)$$

with,

$$\bar{E} = \kappa(\bar{I}_1 - 3) + (1 - 3\kappa)(\bar{I}_4 - 1) \quad (9)$$

where C_{10} , D , k_1 , k_2 and κ are temperature-dependent material parameters. C_{10} and k_1 has the dimension MPa, while k_2 is dimensionless. Furthermore, D is a material constant that controls compressibility[8]. The dispersion parameter κ describes the distribution of the fibres. When $\kappa = 0$, there is no dispersion of the fibres, while, $\kappa = \frac{1}{3}$ describes an isotropic material where the fibres are randomly distributed [9].

In order to describe the mechanical response of the mitral valve leaflets, the constitutive model presented by [7] had to be fitted to experimental data. In the paper published by May-Newman and Yin [10], a strain-energy function derived from experimental data with corresponding material parameters is presented. The suggested model in [10] has an exponential form in terms of the invariants I_1 and I_4 .

$$\Psi(I_1, I_4) = c_0 [exp^{c_1(I_1-3)^2 + c_2(\sqrt{I_4}-1)^4} - 1] + p(J - 1) \quad (10)$$

where c_i , $i=0,1,2$, are material parameters, and p is the Lagrange-multiplier.

The *lsqnonlin* function from the Optimization Toolbox of Matlab was used to perform a nonlinear least square fitting. In table 1, the acquired material parameters from the non-linear regression is presented. Furthermore, figure 2 and 3 shows the stress-stretch relationship, comparing the obtained material parameters with the ones presented by May-Newman and Yin[10]. The leaflets were modelled with a density of 1000 kg/m³

Table 1: Material parameters obtained from nonlinear data-fitting of experimental data provided by [10]

	c_{10} (MPa)	k_1 (MPa)	k_2	κ
Anterior leaflet	0.001	0.0240	50.92	0.1728
Posterior leaflet	0.001	0.0207	52.35	0.2669

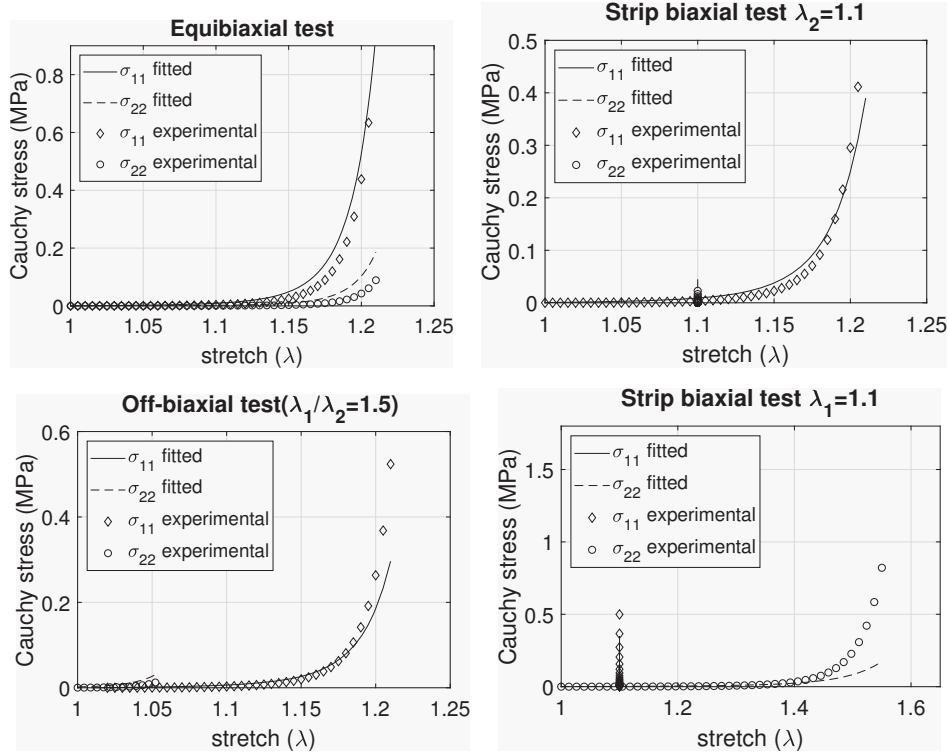


Figure 2: Cauchy-stress vs stretch curves for the anterior leaflet. Experimental data provided by [10] and nonlinear data-fitting of the constitutive model described by [7]

Table 2: Ogden model material parameters for modelling of chordae tendinae. Anterior Marginal(AM), Anterior Strut(AS) and Posterior Marginal(PM). Human and ovine material parameters.

	Human			Ovine		
	AM	AS	PM	AM	AS	PM
$\mu_1(MPa)$	8.91	9.61	9.57	0.37	0.85	0.66
α_1	27.02	30.86	22.78	11.70	28.03	29.67
$\mu_2(MPa)$	12.19	7.99	10.61	1.79	0.21	1.37
α_2	20.91	27.65	21.68	5.00	5.47	18.25
$\mu_3(MPa)$	12.78	7.81	10.65	0.33	0.16	1.46
α_3	20.89	30.00	21.35	34.06	25.06	19.45

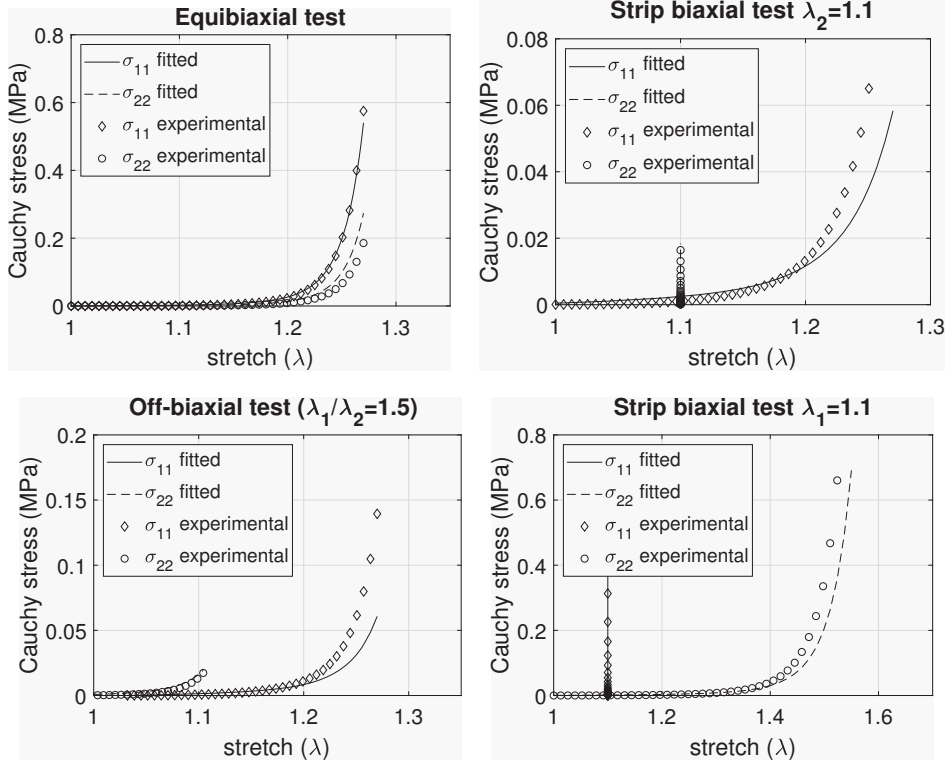


Figure 3: Cauchy-stress vs stretch curves for the posterior leaflet. Experimental data provided by [10] and nonlinear data-fitting of the constitutive model described by [7]

Lastly, the Ogden strain-energy function is used in order to describe the chordae tendineae. When assumed incompressible, the strain-energy function is,

$$\Psi = \sum_{i=1}^N \frac{2\mu_i}{\alpha_i^2} (\lambda_1^{\alpha_i} + \lambda_2^{\alpha_i} + \lambda_3^{\alpha_i} - 3) \quad (11)$$

where μ_i and α_i are material constants and $\lambda_j^{\alpha_i}$ ($j=1,2,3$) are the principal stretches. The material parameters utilized for the chordae is provided by Zuo et al.[11], and describes the response of human chordae tendineae. Material parameters provided by [11] of ovine chordae tendineae was also implemented in another analysis. Human chordae were shown to be significantly stiffer than ovine chordae [11], and myxomatous chordae were found to be 50% less stiff compared to human chordae [12]. Thus, ovine material parameters were studied to compare the global response between the two. In table 2, the material parameters for the marginal chordae and the strut chordae are presented. Lastly, the mechanical response of human and ovine marginal chordae are plotted in figure 4.

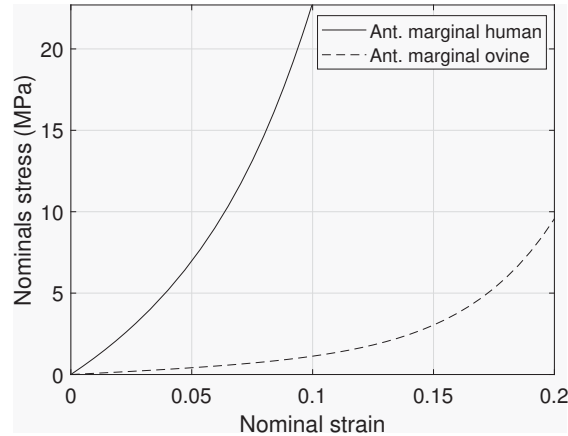


Figure 4: Nominal Stress vs Nominal Strain curves. Human and ovine chordae material parameters implemented in the Ogden material model.

2.4 Geometry

The patient-specific geometry was created from 3D echocardiographic data of a patient diagnosed with Barlow disease. The recordings were imported into a Matlab GUI which enables manual extraction of geometrical points. At the end-diastolic configuration the annulus, leaflet edges and papillary muscle tips were identified (Figure 5).

The annulus was created by extracting points around the annular perimeter and performing a cubic spline interpolation. The anterior and posterior leaflets were constructed by identifying the leaflet edges and the tissue points as shown in figure 5, where the tissue points (white circles in figure 5) are defined as the points between the annulus and the free edge. For the free edge, a cubic interpolation is also performed, creating a continuous line at the margin (figure 6). The extracted points were then imported into the CAD software Rhino, where a non-uniform rational B-spline (NURBS) surface is created by using the tissue points to guide the surface between the annulus and the free edge lines. Furthermore, the papillary muscle tips are identified, and serve as the attachment points for the chordae.

2.5 Chordae modelling

The chordae tendineae originate from the papillary muscles and insert into either the leaflet edge, rough zone or the basal portion of the mitral valve leaflets. However, in this paper the basal chordae are not considered, hence only the marginal and strut chordae are modelled. The marginal chordae insert into the free edge of both the anterior and posterior leaflets, while the strut chordae insert into the anterior leaflet only.

Twelve marginal chordae were modelled to originate from each papillary muscle. Each marginal chordae was then split in a fan-like manner, inserting into the leaflet edge with

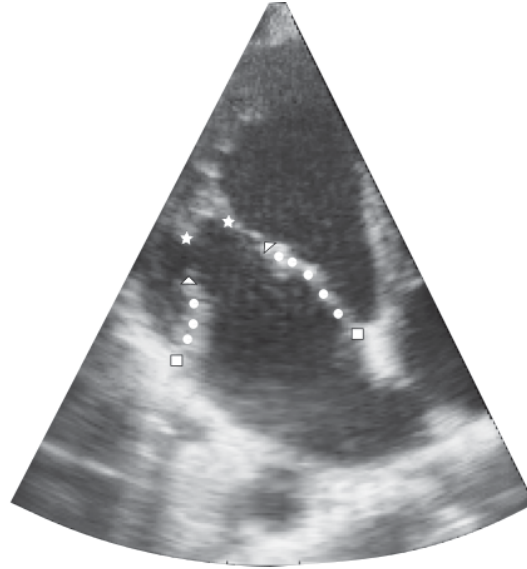


Figure 5: Explanation of the anatomical components on an echocardiographic image, end-diastolic configuration. Papillary Muscle Tips (stars), Posterior leaflet edge (left triangle), Anterior leaflet edge (right triangle), Annulus (squares). White circles represent the tissue points, extracted from the middle of the leaflets.

about five different insertion points as described by [13]. The branching was mainly done in order to simulate a more anatomically correct model, where the branch origin was set between the papillary muscle and the free edge (figure 7a). Moreover, the branching led to a redistribution of stress on the leaflet edge, hence preventing excessive distorted elements in the analysis. Lastly, the strut chordae is inserted into the rough zone of the anterior leaflet, which is situated between the annulus and the free edge. As with the marginal chordae, the strut chordae branches out in a fan-like manner. The branching is distributed to the nearby nodes of the main insertion point (figure 7a).

The cross-sectional areas for human marginal and strut chordae was modelled to be 0.25 mm^2 and 1.27 mm^2 respectively. While, for the ovine chordae the cross-sectional areas were modelled to be 0.26 mm^2 and 0.6 mm^2 . Here, the chordae were assumed to be circular and calculated with the cross-sectional diameter presented in the paper published by [11], which studied human and ovine cadaver hearts.

2.6 Finite element model

The end-diastolic finite element geometry constructed from the echocardiographic data is depicted in figure 7. For the anterior and posterior leaflets, four noded general-purpose shell elements (S4) were used. The chordae tendineae were modelled as two-noded 3D truss elements (T3D2). Furthermore, the overall leaflet thickness was set to be 3mm,

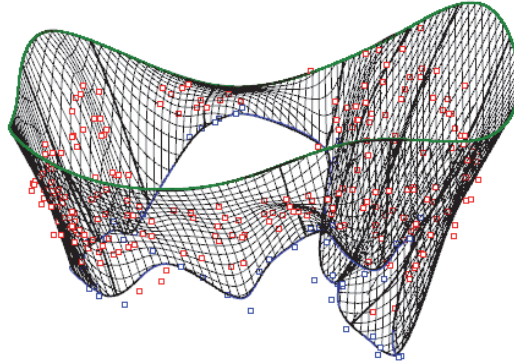


Figure 6: NURBS surface created from imported echocardiographic point cloud. Annulus - green line, Tissue points represented in red and leaflet free edge - blue line.
NURBS surface

which is the average overall thickness of Barlow leaflets found by [5]. As for contact, a general contact algorithm available in Abaqus was applied. The tangential contact behaviour was set to frictionless and the normal contact behaviour was a hard contact condition [9].

The material orientation applied to the mitral valve leaflets is obtained from small angle light scattering (SALS) data presented by [14]. In the paper presented by [14], the mean collagen fibre direction is observed to be perpendicular to the annulus near the commissures, and parallel to the annulus at the middle of the leaflets. Moreover, the fibre direction is observed to gradually rotate from parallel to perpendicular towards the commissures. Implementation of the fibre direction in Abaqus is done by partitioning the leaflet into several regions. Then a material orientation was assigned to each individual partitioned region (figure 7b).

2.7 Boundary conditions and loading

In order to model the boundary conditions, the dynamics of the papillary muscle tips and the annulus was obtained using *in vivo* echocardiographic data. The geometry of the annulus and the positions of the PMs are recorded for all time-frames, between end-diastole and end-systole. As it is difficult to track material points from echocardiographic measurements, the motion of the annulus was prescribed using displacement boundary conditions determined from the acquired images, under the assumption that heterogeneity in annular strain is small. First, the annular geometries of each time step were modelled as periodic degree-3 spline curves parameterised by arc length. Then, the relative parameterisation of the annular curves was optimised to find the point-wise map that minimised the total displacement between two consecutive curves as described by Rego et al. [15]. Between each configuration a linear interpolation is performed, creating a continuously

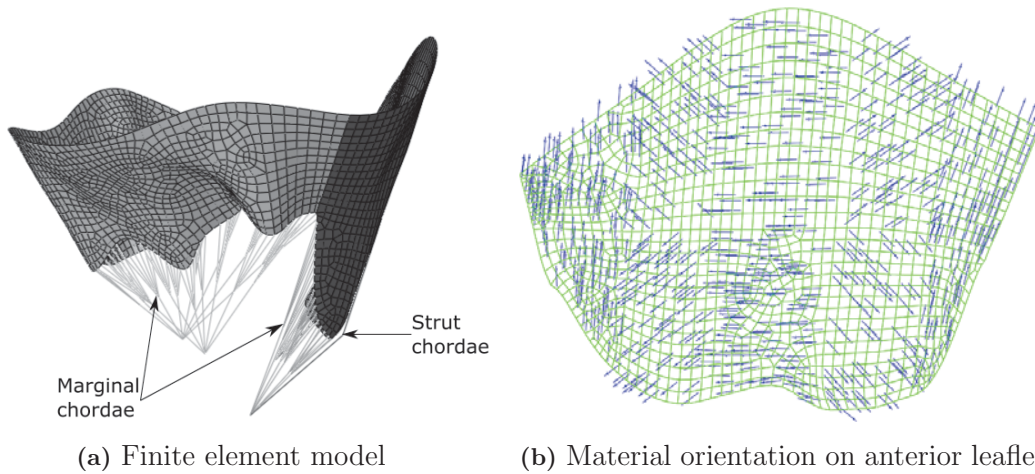


Figure 7: (a) - Finite element model created from echocardiographic data. Posterior leaflet (light gray), anterior leaflet (dark grey). (b) - Anterior leaflet material orientation.

movement between the time-frames. These boundary conditions are then implemented into the Abaqus user subroutine VDISP.

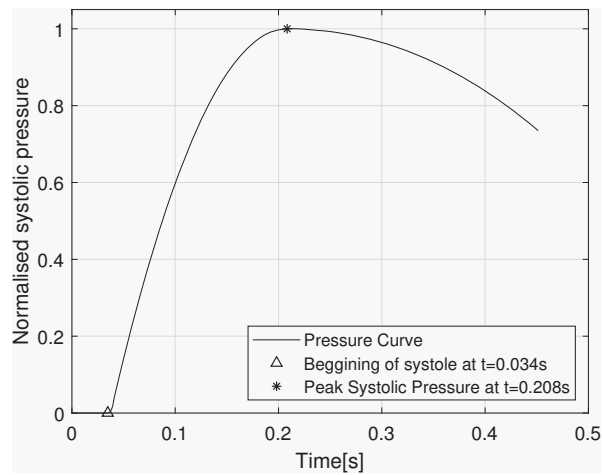


Figure 8: Load Amplitude Curve in the Cardiac Cycle

A uniformly distributed pressure was applied to the leaflets' ventricular surface, with a patient specific peak pressure of 18.13 kPa (136mmHg). Furthermore, the amplitude was modelled in order to follow a pressure curve similar to the one during the cardiac cycle [16]. The pressure curve is presented in figure 8, where the pressure is applied to

the ventricular surface of the leaflets throughout systole.

3 Results

3.1 Measurements of FE geometry

The geometry modelled from echocardiographic data has been compared with measurements obtained in literature of a Barlow mitral valve and a healthy mitral valve. The goal being to verify the geometry with anatomical measurements of Barlow mitral valves. Furthermore, the Barlow mitral valve studied herein shows abnormal features such as excessive tissue and a severely dilated annulus. The finite element model is measured in both the end-diastolic and end-systolic configuration. In table 3 the measurements are presented.

Table 3: Mitral valve measurements of the FE model, compared with measurements from literature both *in vitro* and from 3D echocardiography. [13, 17, 18, 3]

	FE model		From Literature		
	ED	PS	Barlow (S)	Barlow (D)	Healthy (D)
Annular perimeter (mm)	170	160	158 ±19	148±17	82 ±7
IC diameter (mm)	50.83	-	45±9	46.6 ±5	39.5 ±3.4
AP diameter (mm)	45.02	-	44 ±8	37.3 ±6	32.2 ±3.6
Anterior leaflet height (mm)	32.07	-	-	-	20 ±2
Posterior leaflet height (mm)	19.85	-	-	-	12 ±1
AC height (mm)	10.03	-	-	-	7 ±1
PC height (mm)	12.05	-	-	-	7 ±1
3D annular area (mm ²)	2100	1625	-	1500 ±280	-
3D total leaflet area (mm ²)	2645	-	2302 ±455	1850 ±490	-
Anterior leaflet area (mm ²)	1145	-	1162 ±276	-	-
Posterior leaflet area (mm ²)	1500	-	1175 ±306	-	-

IC- Intercommisural, AP-Anteroposterior, AC-Anterolateral Commissure, PC-Posteriomedial commissure, ED-End Diastole, PS-Peak Systole, S-Systole, D-Diastole.

As can be seen in table 3, the FE model measurements coincide with the upper limits of the diastolic Barlow measures extracted from literature [3, 17]. Furthermore, for each time step, a mean annulus plane was calculated. Then, the annulus was projected onto this mean plane and a two-dimensional (2D) area was computed and plotted against time in figure 9a. This plot shows how much the annulus dilates throughout the whole cardiac cycle. Then, the mean squared distance of the annulus to this plane was computed and plotted in figure 9b, showing how much the annulus flattens during one full cardiac cycle. The t-wave on the ECG signal is observed prior to 0.5s, hence the measurements in figure 9 represent systole from 0 to 0.5s. As can be seen in figure 9b, the annulus is distinctly flattened during systole. Note that the end-diastolic configuration is the very last time

step in figure 9.

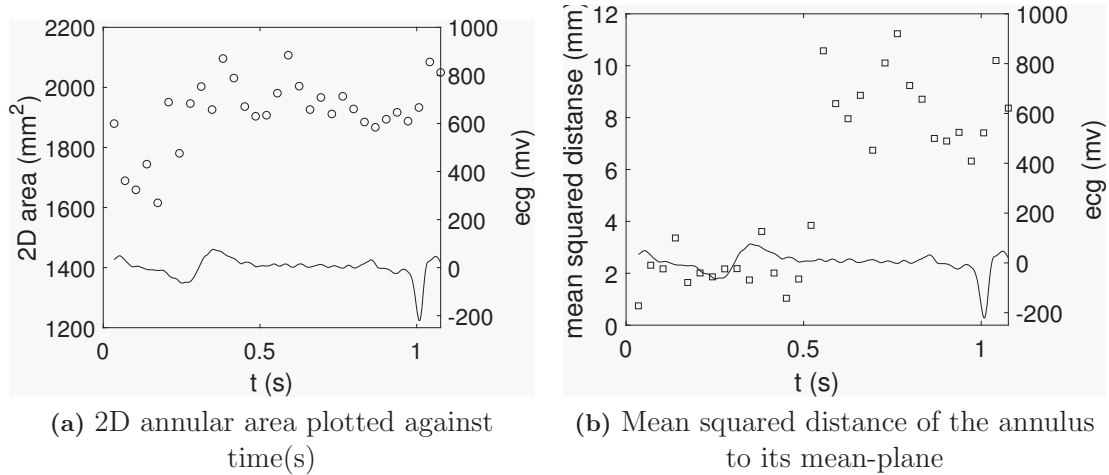


Figure 9: Annular measurements and shape. ECG signal(solid curve), 2D area (circles) and mean squared distance (squares).

3.2 Comparison with three-dimensional echocardiographic data

Figure 10 shows the global response at the A2-P2 region of the leaflet compared to echocardiography at peak systole. As can be seen, there is a very good correspondence between the echocardiographic measurements and the mitral valve models.

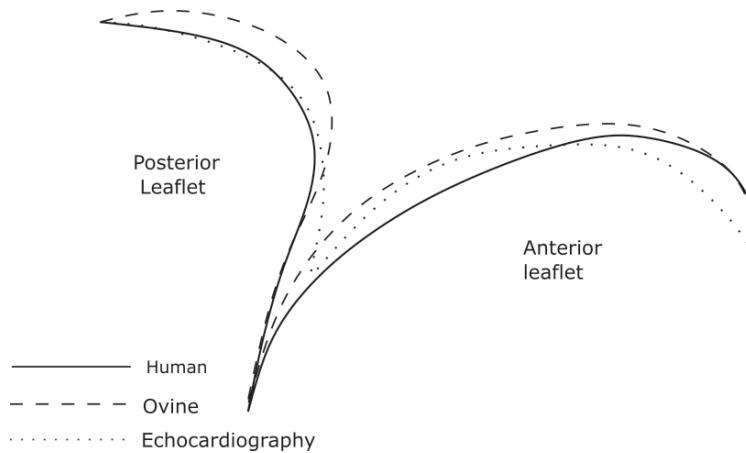


Figure 10: Comparison between finite element models and echocardiography along the A2-P2 leaflets at peak systolic pressure $p=136\text{mmHg}$, using human and ovine chordae material parameters.

3.3 Global Response

In this section, the global response of the finite element analysis is presented. Figure 11 depicts the valve closure from end-diastole to end-systole observed from the left atrium.

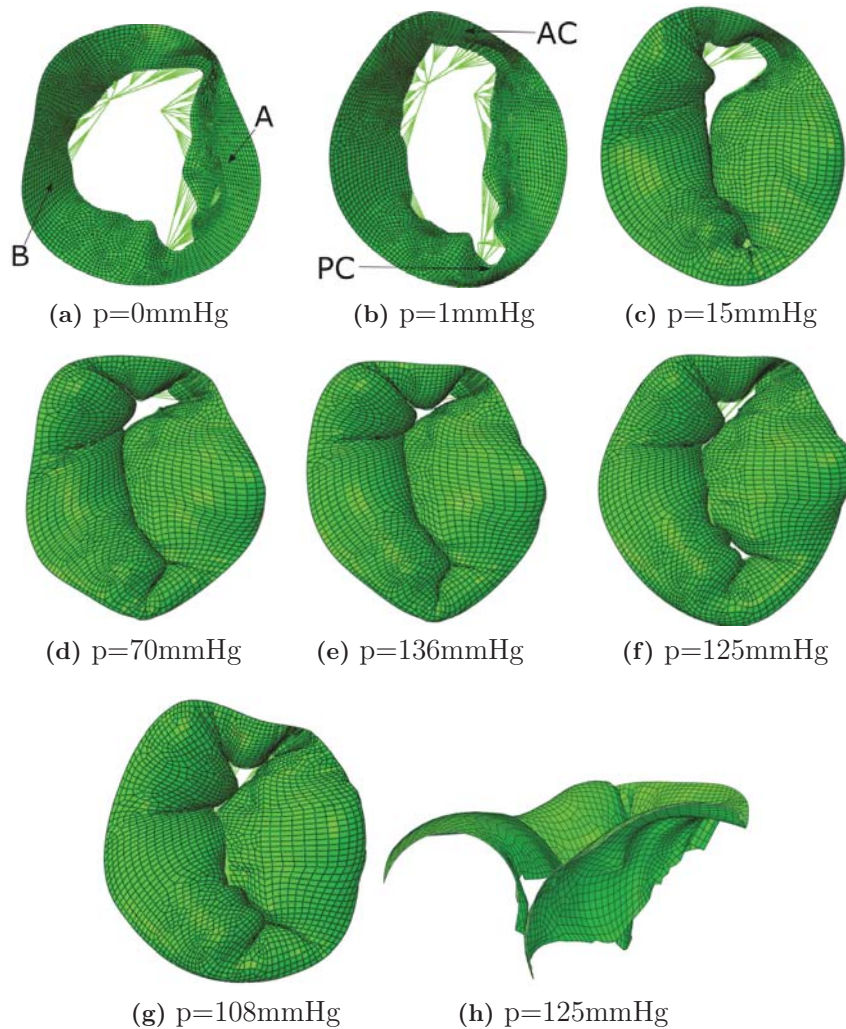


Figure 11: Valve closure of finite element model from end-diastole to end-systole. (a) End-diastolic configuration, $p=0$ mmHg. (b) $p=1$ mmHg. (c) First observation of coapting surfaces, $p=15$ mmHg. (d) $p=70$ mmHg. (e) Peak systolic pressure, $p=136$ mmHg. (f) Late systolic regurgitation, $p=125$ mmHg. (g) End-systolic configuration, $p=108$ mmHg. (h) Cut-view of prolapse at the posteromedial side of the P2 segment

From figure 11 it can firstly be observed regurgitation at the anterolateral region (A1-P1) throughout the whole analysis. Secondly, the annular motion is clearly observed in figure 11. Lastly, in figure 11f, a late systolic regurgitation can be observed near the posteromedial commissure (A3-P3). Figure 11h depicts a cut-view, showing what appears to be prolapse at the posteromedial side of the P2 segment. The prolapse is observed at the same time as the late systolic regurgitation in figure 11f. Note that the prolapse is present until the end of systole.

3.4 Displacements

The norm of the displacement of point A and B (figure 12a) are plotted against time in figure 12. Prior to the pressure being applied, it is observed that point A and B move without any loading. These movements are due to the annular and papillary muscle dynamics. Moreover, figure 12 shows that as the analysis approaches 0.1s ($p=81$ mmHg) the leaflets tend to oscillate very little for the rest of the analysis. Lastly, in figure 12, the displacements of point A and B are plotted to compare the leaflet response when ovine and human chordae material parameters are implemented.

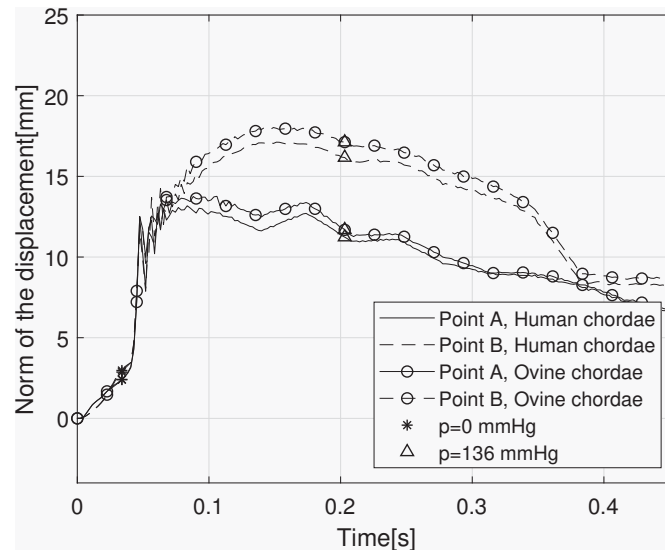


Figure 12: Norm of the displacement of point A and B, obtained with leaflet parameters from table 1, and human and ovine chordae material parameters from table 2

3.5 Material parameter study

In this section the material parameters acquired from the nonlinear data-fitting is compared with stiffer and softer material parameters for the leaflets. This is done in order to observe if there is any difference in global response, when changing these parameters. In

figure 13a, the stress-stretch curves are plotted for an equibiaxial tensile test. Furthermore, in figure 13b the magnitude of point A is plotted, comparing the response from table 1 with the stiffer and softer material parameters.

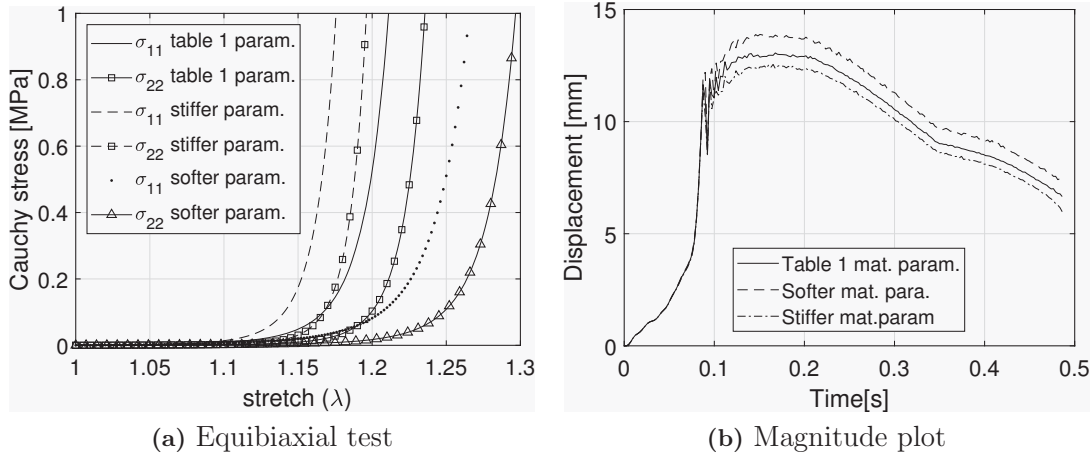


Figure 13: Displacement of point A obtained from analyses using stiffer and softer material parameters compared with material parameters from nonlinear data-fitting.

From figure 13b, the response is as expected. For the stiffer material there are small oscillations during the analysis, and the displacement of point A at peak systole is 0.60mm less for the stiffer material, compared with the material parameters obtained in table 1. Moreover, the softer material clearly has higher oscillations throughout the analysis and displaces 0.75mm higher than the material parameters from table 1 at peak systole. Lastly, it is observed that during the first part of the analysis the response is similar for every analysis. Even for the large difference in stiffness in figure 13a, the difference in leaflet displacement in figure 13b is moderate.

3.6 Stresses

The leaflets von Mises stresses are plotted at peak systole (18.13 kPa) in figure 14. High stress regions are observed near the location where the strut chordae is inserted into the anterior leaflet and near the fibrous trigones. At the marginal chordae insertion points there is also observed high von Mises stresses. However, high stresses are also observed due to the implementation of material orientations, and is further discussed in the section 4.6.

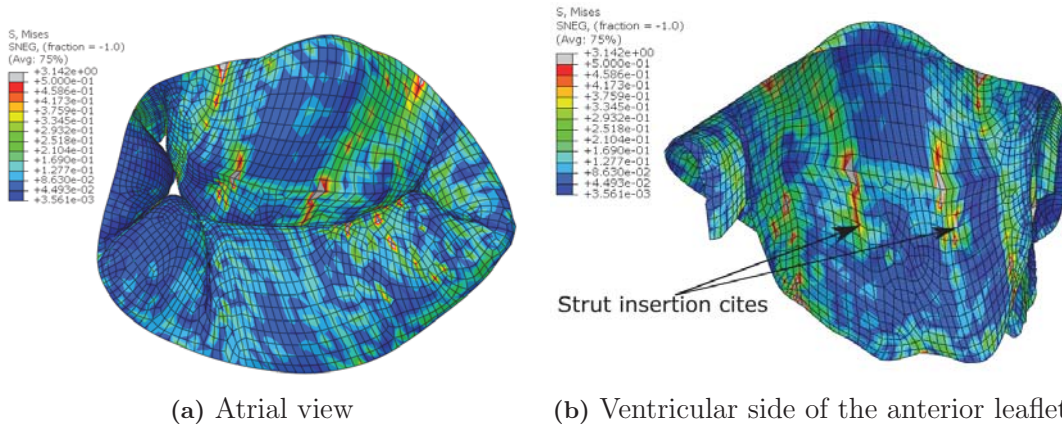


Figure 14: von Mises stress of the mitral valve leaflets (MPa)

The maximum principal stress direction is plotted on the deformed leaflets in figure 15. As can be seen from figure 15a, the maximum principal stress is aligned with the modelled material orientation for the anterior leaflet. The maximum principal stress for the entire posterior leaflet is observed in figure 15b to be perpendicular to the annulus. As a result, in the posterior leaflet, the maximum principal stress only aligns with the assigned material orientation near the commissures.

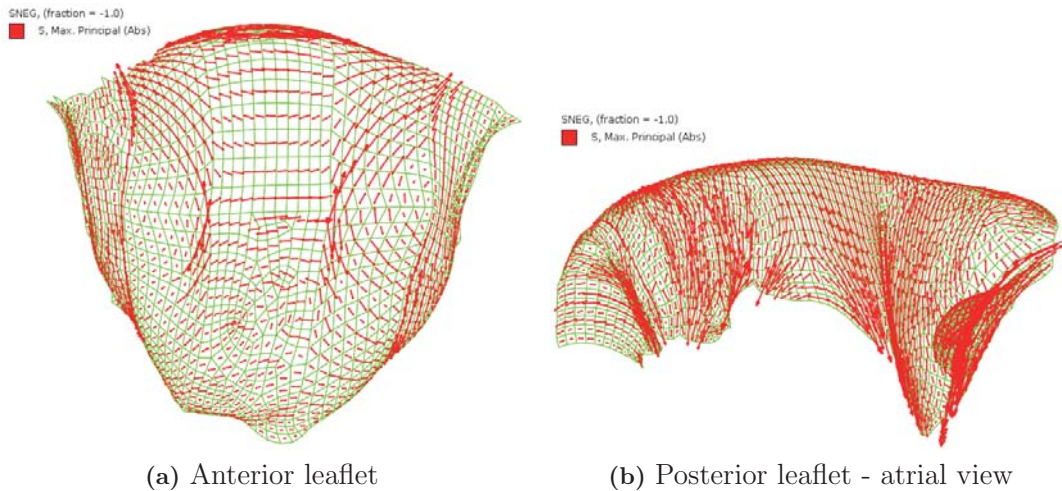


Figure 15: Maximum principal stress plotted on deformed mitral valve leaflets.

4 Discussion

4.1 Global Response

The global response presented in section 3.3 shows that there is regurgitation at the posteromedial region (A3-P3) at late-systole. Moreover, the posteromedial side of the P2 segment is observed to prolapse at late-systole causing the posterior leaflet to override the anterior leaflet. These results are highly consistent with what we know about the patient's lesions, where regurgitation was detected in the posteromedial region at late systole.

In the anterolateral region (A1-P1), lack of closure in the FE model is observed throughout the whole analysis. The severity of regurgitation in this region is high before and after peak systole for the model. However, comparing the anterolateral regurgitation observed in the patient, the obtained results did not fully coincide with the patient. The patient experienced regurgitation due to prolapse of the P1 segment from mid systole, which is not entirely what the FE model predicts. The echocardiographic modelling might be the reason for the inaccurate observation of regurgitation at this region, and is further discussed in section 4.2.

As can be seen from figure 9a, the annular area starts to increase prior to peak systole ($t=0.17s$). The annulus continues to expand until the pressure has reached approximately 118mmHg (0.38s). Furthermore, the annular flattening observed during systole (figure 9b) is similar to what is written in literature about Barlow diseased mitral valves [17],[3]. Comparing these findings with the global response (figure 11), it is evident that the annular changes must affect the coaptation of the leaflets. The late systolic regurgitation is observed when the annular area is at its highest. Thus, the dilation of the annulus may be a reason for regurgitation during this time interval.

4.2 Echocardiographic modelling

The patient-specific mitral valve geometry was modelled using echocardiographic data as described in section 2.4. The anterior leaflet and the P2 segment of the posterior leaflet were clearly visible on the echocardiographic images. However, locating the commissures was a more demanding process, where several echocardiographic views were needed. At the posteromedial commissure, the leaflets could be identified from the echocardiographic recording. Hence, the geometry obtained was satisfactory. For the anterolateral commissure the identification of the leaflet structure was cumbersome, leading to considerable uncertainty in the geometry at this region. As a consequence, the interpolated free edge at the anterolateral commissure was inaccurate.

As discussed in section 4.1 regurgitation is observed in the anterolateral region during systole. However, the patient did not experience similar severity of regurgitation near the anterolateral commissure. Thus, the observed regurgitation from the FE analysis is probably a consequence of the inaccurate modelling at the anterolateral region.

4.3 Comparison with 3D echocardiographic data

In figure 10, the correlation between the echocardiographic measurements and the mitral valve model response are observed to be very good. The bulging towards the left atrium is similar to that of the echocardiographic measurements. However, the FE response for both human and ovine chordae material parameters are shown to coapt further toward the left ventricle at peak systole compared to echocardiography. Furthermore, it is observed that both FE models bulge more than the echocardiographic measurements near the annulus, especially for the ovine material parameters.

Performing a similar comparison near the commissures at peak systole is difficult, as there is observed a lot of tissue on the echocardiographic images at this region. Collocating the echocardiographic measurements and the FE model at the commissures, show that the FE model bulges to little towards the atrium. The excessive tissue at this region is probably an combination of Barlow disease and calcifications near the annulus, making the comparison between the *in vivo* images and the FE model difficult in this region.

4.4 Material parameters

In order to use the Holzapfel-Gasser-Ogden material model, introduced in section 2.3, to model the response of the mitral valve, it is required that the material parameters implemented in the model show a similar response compared to experimental data presented by [10]. Obtaining a good fit between the experimental data and the material model provided by Abaqus, can make it possible to omit the usage of the subroutine VUMAT, where VUMAT is an Abaqus Explicit subroutine used to model different material models not directly available in Abaqus. The study performed in section 2.3, gave a sound fit comparing the experimental data from [10], with the Holzapfel-Gasser-Ogden strain-energy function.

Human mitral valve tissue has been shown to be stiffer than porcine mitral valve tissue [19]. Hence, it can be argued that using porcine material properties might not give a correct response when modelling a human mitral valve. However, in the study [12], myxomatous mitral valve leaflets were identified to be twice as extensible and less stiff compared to healthy human leaflets. As a consequence, porcine material parameters are assumed to be a better assumption than using the parameters from a healthy human, due to the difference in stiffness.

The chordae tendineae was modelled with both human and ovine material parameters. Comparing the global response, the coaptation and the location of regurgitation was observed to be near identical. From figure 12, the total displacement of point A and B are approximately $1mm$ higher for the ovine chordae parameters. Furthermore, the difference in displacement is mainly observed when the ventricular surface is subjected to peak pressures leading to high chordae strains. As a consequence the human chordae is observed to displace less at high strains compared to the ovine chordae due to the nature of the material. In the study by [12], myxomatous chordae tendineae were found to be 50

% less stiff compared to human chordae. Studying the comparison with 3D echocardiographic measurements, the ovine chordae parameters are observed to correlate less to the echocardiography than the model with human chordae parameters. Furthermore, there is observed little difference in coaptation between the models, but the ovine model prolapses more as both the leaflets displace towards the atrium.

In section 3.5, it was shown that the difference in displacements between the stiffer, softer and material parameters from table 1 were low. Hence, it appears that annulus and papillary muscle movements have more influence on the global response than the applied materials.

4.5 Chordae modelling

The marginal chordae tendineae are modelled so that they originate from the papillary muscles and insert into the free edge of the mitral valve leaflets, while the strut chordae insert into the anterior leaflet rough zone. The chordae insertion sites at the free edge are prone to high stresses, and the splitting of the chordae helps redistributing the loads along the elements, preventing the elements from excessive distortion. The chordae modelling is not just important for anatomical correctness but also for the finite element analysis as a whole.

From echocardiographic images it is not possible to get a full representation of the chordae insertion site, nor the amount of chordae. As a consequence, for a patient-specific analysis, the amount of chordae and insertion sites has to be assumed from literature [13]. Furthermore, it is not possible to detect if the chordae are stretched or not in diastole. A characteristic feature for Barlow patients is the elongated chordae at systole [1], which might leave the chordae slack at diastole. It is therefore assumed that there is no pre-tension in the chordae for a Barlow patient. Hence, the chordae are modelled as straight lines without any form of pre-tension. The model managed to follow the echocardiographic measurements without any pre-tensions, which was not the case in the study performed by [20]. However, in the study by [20] the studied valve was a patient with functional mitral regurgitation (FMR), which is not a degenerative disease. It can be argued that some of the chordae should be modelled slack. However, this needs to be studied further.

4.6 Material orientation

The material orientation applied in the FE model on the mitral valve leaflets is for a healthy porcine specimen. However, as stated in literature, the collagen fibres in Barlow leaflets are observed to be disoriented and disrupted [5]. In [21], this disruption is found to be due to myxomatous degeneration. Hence, the fibre direction used in this paper may not be entirely accurate. However, to the author's knowledge little is known about the collagen orientation for Barlow mitral leaflets. The gradual rotation of the collagen fibres towards the commissures in the anterior leaflet is not fully accounted for, where instead each partitioned region is given one specific direction as described in section 2.6. This

modelling technique leads to some abrupt changes where the modelled orientation changes (figure 7b.). This leads to the stress concentrations observed on the anterior leaflet, just above the chordae insertions (figure 14).

4.7 Stresses

The von Mises stresses were found to be highest where the abrupt changes in material orientation were present. However, removing the elements with high stresses due to this feature, more reasonable stress values were observed. Regions of high stresses near the chordae insertion points, especially where the strut chordae is inserted, and the fibrous trigones are observed. This is consistent with previous studies [22, 23]. However, comparing stress values with literature, is not so beneficial, as an unusual thickness of $3mm$ is used in this study.

5 Conclusion

In this paper, a finite element model of a mitral valve with Barlow disease has been employed with annular and papillary muscle motions. Lack of closure were observed in both the anterolateral and posteromedial commissure for the model. This agrees, to some extent with the echocardiographic findings of the patient. The finite element model predicted regurgitation in the posteromedial region well, where late systolic regurgitation and prolapse were observed for both the patient and model. In the anterolateral region the model predicted regurgitation throughout systole, while echocardiography only showed regurgitation at mid-systole. An explanation for this discrepancy might be that the commissure geometry is difficult to define from echocardiography, especially for the anterolateral commissure. Refinement of the method used to localize these regions *in vivo* are necessary to create accurate models. In order to refine the geometrical modelling, an autostereoscopic 3D screen could be used to locate intricate points near the commissures [24]. Lastly, severe annular dilation seems to be one major cause of mitral regurgitation. In this study, the most severe lack of closure from mid- to late-systole appeared when the annulus dilated the most.

Creating accurate patient-specific models which can predict regurgitation correctly and reliably will in the future open up several exciting possibilities: for example, performing surgery *in silico* in order to optimize and create a patient-specific surgical procedure. Furthermore, it may facilitate the development of repair devices as they can be tested and refined numerically.

REFERENCES

- [1] Carpentier, Alain and Adams, David H. and Filsoufi, Farzan *Carpentier's reconstructive valve surgery : from valve analysis to valve reconstruction*. Saunders Elsevier, Vol. I., (2010).
- [2] Iung, B., Baron, G., Tornos, P., Gohlke-Barwolf, C., Butchart, E. G. and Vahanian, A. Valvular heart disease in the community: a European experience. *Curr. Probl. Cardiol.* (2007) **32**:609–61.
- [3] Apor, A., Nagy, A. I., Kovacs, A., Manouras, A., Andrassy, P. and Merkely, B. Three-dimensional dynamic morphology of the mitral valve in different forms of mitral valve prolapse - potential implications for annuloplasty ring selection. *Cardiovasc. Ultrasound* (2016) **14**:32.
- [4] Jouan, J., Berrebi, A., Chauvaud, S., Menasche, P., Carpentier, A. and Fabiani, J. N. Mitral valve reconstruction in Barlow disease: long-term echographic results and implications for surgical management *J. Thorac. Cardiovasc. Surg.* (2012) **143**:517–20.
- [5] Hjortnaes, J., Keegan, J., Bruneval, P., Schwartz, E., Schoen, F. J., Carpentier, A., Levine, R. A., Hagege, A. and Aikawa, E. Comparative Histopathological Analysis of Mitral Valves in Barlow Disease and Fibroelastic Deficiency *Semin. Thorac. Cardiovasc. Surg.* (2016) **37**:757–767.
- [6] Prot, V., Skallerud, B. and Holzapfel, G. A. Transversely isotropic membrane shells with application to mitral valve mechanics. Constitutive modelling and finite element implementation. *Int. J. Numer. Meth. Engng.* (2007) **3**:987–1008.
- [7] Holzapfel, G. A., Ogden, R. W. and Gasser, T. C. Hyperelastic modelling of arterial layers with distributed collagen fibre orientations *J. R. Soc. Interface* (2006) **3**:15–35.
- [8] Prot, V. and Skallerud, B. Nonlinear solid finite element analysis of mitral valves with heterogeneous leaflet layers. *Comput. Mech.* (2008) **43**:353–368.
- [9] Abaqus *Abaqus Analysis User's Guide*. Dassault Systemes, Vol. (2014).
- [10] May-Newman, K. and Yin, F. C. A constitutive law for mitral valve tissue. *J Biomech Eng* (1998) **120**:38–47.
- [11] Zuo, K., Pham, T., Li, K., Martin, C., He, Z. and Sun, W. Characterization of biomechanical properties of aged human and ovine mitral valve chordae tendineae. *J. Mech. Behav. Biomed. Mater.* (2016) **62**:607–18.

- [12] Barber, J. E., Ratliff, N. B., Cosgrove, D. M., 3rd, Griffin, B. P. and Vesely, I. Myxomatous mitral valve chordae. I: Mechanical properties. *J. Heart. Valve. Dis.* (2001) **122**:955–62.
- [13] Kunzelman, K. S., Cochran, R. P., Verrier, E. D. and Eberhart, R. C. Anatomic basis for mitral valve modelling. *J. Heart Valve Dis.* (1994) **3**:449–58.
- [14] Cochran, R. P., Kunzelman, K. S., Chuong, C. J., Sacks, M. S. and Eberhart, R. C. Nondestructive analysis of mitral valve collagen fiber orientation *ASAIO Trans.* (1991) **37**:447–8.
- [15] Rego, B. V., A. H. Khalighi, A. Drach, E. K. Lai, A. M. Pouch, R. C. Gorman, J. H. Gorman, and M. S. Sacks. A noninvasive method for the determination of in vivo mitral valve leaflet strains. *Int. j. numer. method. biomed. eng.* (2018) **34**:e3142.
- [16] J. Levick *An Introduction to Cardiovascular Physiology*. Hodder Arnold, Vol. 5., (2010).
- [17] Grewal, J., Suri, R., Mankad, S., Tanaka, A., Mahoney, D. W., Schaff, H. V., Miller, F. A. and Enriquez-Sarano, M. Mitral annular dynamics in myxomatous valve disease: new insights with real-time 3-dimensional echocardiography. *Circulation* (2010) **121**:1423–31.
- [18] Chandra, S., Salgo, I. S., Sugeng, L., Weinert, L., Tsang, W., Takeuchi, M., Spencer, K. T., O’Connor, A., Cardinale, M., Settlemier, S., Mor-Avi, V. and Lang, R. M. Characterization of degenerative mitral valve disease using morphologic analysis of real-time three-dimensional echocardiographic images: objective insight into complexity and planning of mitral valve repair. *Circ. Cardiovasc. Imaging* (2011) **4**:24–32.
- [19] Prot, V., Skallerud, B., Sommer, G. and Holzapfel, G. A. On modelling and analysis of healthy and pathological human mitral valves: two case studies. *J. Mech. Behav. Biomed. Mater.* (2010) **3**:167–77.
- [20] Pham, T., Kong, F., Martin, C., Wang, Q., Primiano, C., McKay, R., Elefteriades, J. and Sun, W. Finite Element Analysis of Patient-Specific Mitral Valve with Mitral Regurgitation. *Cardiovasc. Eng. Technol.* (2017) **8**:3–16.
- [21] Anyanwu, A. C. and Adams, D. H. Etiologic classification of degenerative mitral valve disease: Barlow’s disease and fibroelastic deficiency. *Semin. Thorac. Cardiovasc. Surg.* (2007) **19**:90–6.
- [22] Prot, V., Haaverstad, R. and Skallerud, B. Finite element analysis of the mitral apparatus: annulus shape effect and chordal force distribution. *Biomech. Model. Mechanobiol.* (2008) **8**:43–55.

- [23] Votta, E., Caiani, E., Veronesi, F., Soncini, M., Montevecchi, F. M. and Redaelli, A. Mitral valve finite-element modelling from ultrasound data: a pilot study for a new approach to understand mitral function and clinical scenarios. *Philos. Trans. A Math. Phys. Eng. Sci.* (2008) **366**:3411–34.
- [24] Dumont, K. A., Kvitting, J. P., Karlsen, J. S., Remme, E. W., Hausken, J., Lundblad, R., Fiane, A. E. and Urheim, S. Validation of a Holographic Display for Quantification of Mitral Annular Dynamics by Three-Dimensional Echocardiography. *J. Am. Soc. Echocardiogr.* (2019) **32**:303–316 e4.